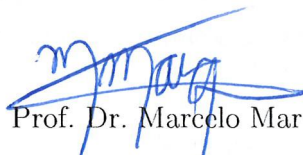


Dissertation presented to the Instituto Tecnológico de Aeronáutica, in partial fulfillment of the requirements for the degree of Master of Science in the Graduate Program of Physics, Field of Atomic and Molecular Physics.

Bruno Lucatto

**AB INITIO STUDY OF 2D
HETEROSTRUCTURES AND DEFECTS IN 3D
SEMICONDUCTORS FOR PHYSICAL
IMPLEMENTATION OF QUBITS**

Dissertation approved in its final version by signatories below:


Prof. Dr. Marcelo Marques
Advisor

Prof. Dr. Pedro Teixeira Lacava
Dean for Graduate Education and Research

Campo Montenegro
São José dos Campos, SP - Brazil
2018

Cataloging-in Publication Data
Documentation and Information Division

Lucatto, Bruno

Ab initio study of 2D heterostructures and defects in 3D semiconductors for physical implementation of qubits / Bruno Lucatto.

São José dos Campos, 2018.

111f.

Dissertation of Master of Science – Course of Physics. Area of Atomic and Molecular Physics – Instituto Tecnológico de Aeronáutica, 2018. Advisor: Prof. Dr. Marcelo Marques.

1. Heteroestruturas de van der Waals. 2. Estruturas bidimensionais. 3. Semicondutores. 4. Cálculos ab initio. 5. Física. I. Instituto Tecnológico de Aeronáutica. II. Title.

BIBLIOGRAPHIC REFERENCE

LUCATTO, Bruno. **Ab initio study of 2D heterostructures and defects in 3D semiconductors for physical implementation of qubits**. 2018. 111f. Dissertation of Master of Science – Instituto Tecnológico de Aeronáutica, São José dos Campos.

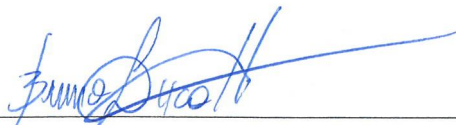
CESSION OF RIGHTS

AUTHOR'S NAME: Bruno Lucatto

PUBLICATION TITLE: Ab initio study of 2D heterostructures and defects in 3D semiconductors for physical implementation of qubits.

PUBLICATION KIND/YEAR: Dissertation / 2018

It is granted to Instituto Tecnológico de Aeronáutica permission to reproduce copies of this dissertation and to only loan or to sell copies for academic and scientific purposes. The author reserves other publication rights and no part of this dissertation can be reproduced without the authorization of the author.



Bruno Lucatto

Av. Marechal do Ar Eduardo Gomes, 50
12.228-900 – São José dos Campos–SP

AB INITIO STUDY OF 2D HETEROSTRUCTURES AND DEFECTS IN 3D SEMICONDUCTORS FOR PHYSICAL IMPLEMENTATION OF QUBITS

Bruno Lucatto

Thesis Committee Composition:

Prof. Dr. Jayr de Amorim Filho	Chairperson	-	ITA
Prof. Dr. Marcelo Marques	Advisor	-	ITA
Prof. Dr. Luiz Fernando de Araújo Ferrão	Member	-	ITA
Prof. Dr. Guilherme Matos Sipahi	External Member	-	USP
Prof. Dr. José Edimar Barbosa Oliveira	Internal Substitute	-	ITA
Prof. Dr. Luiz Tadeu Fernandes Eleno	External Substitute	-	USP

To the reader

Acknowledgments

First and foremost, I would like to thank my parents, Célia and Gerson, for their constant support through all my life, and for dedicating so much love for me. I appreciate everything they have always done.

To my advisor, professor Marques, who has always been very enthusiastic about this work and has dedicated much of his time in long conversations about it and in uncountable meetings. To professors Lara, Ronaldo, and Lucy, whose contributions to this work were so many.

To Matteus Caprecci and Flávio Marchi, who were always very supportive whenever it was needed. To Daniel S. Koda and Ivan Guilhon, for the always highly instructive discussions. I also would like to thank him and all my other friends for the awesome moments and awesome fun we always had!

Finally, I would like to thank Jackeline, for making my life happier each day, and for supporting me in achieving my goals.

Back in the 1940s, researchers were just discovering how to use vacuum tubes as simple switches. These switches could then form logic gates, which could be linked together to form the first logic circuits. That's where we're at now with quantum processors.

We have verified that all the components work.

The next step is to engineer the smallest, yet most interesting circuit possible.

— JUNGSANG KIM

Abstract

A major challenge in creating a quantum computer is to find a quantum system that could be used to implement the qubits. In this scenario, solid state systems, such as deep center defects in semiconductors or quantum dots, are prominent qubit candidates, and *ab initio* calculations are one of the most important tools to theoretically study their properties. However, these calculations are usually highly involved, due to the large supercells needed, and the computational cost can be even larger when one goes beyond the Kohn-Sham scheme to correct the band gap problem and achieve good accuracy in the prediction of excited state phenomena.

In this work, we use first principle calculations in the search of materials and systems that would be suitable for the physical implementation of quantum bits and other quantum information devices. This is addressed on two fronts: First, we develop a method that sharply reduces the computational cost of simulating deep center defects with DFT including quasiparticle corrections, and then we benchmark it with the largely used quantum register based on the negatively-charged NV center in diamond, obtaining a great agreement with experimental data. Second, we demonstrate the possibility of using a gated van der Waals heterostructure to implement spatial quantum superpositions of electron states and, moreover, to implement a qubit. We study the case of the ZrSe₂/SnSe₂ heterostructure, simulating it under the influence of the gate field, providing theoretical quantitative results of its operation as a qubit, and proposing a possible methodology to manipulate and to measure the information in this qubit.

List of Figures

FIGURE 2.1 – Flowchart of the algorithm used in the self-consistent solution of the Kohn-Sham equations.	24
FIGURE 2.2 – Calculated and experimental band gaps for several semiconductors. The calculations were performed with both LDA and LDA-1/2 potentials. The diagonal line (in black) corresponds to a perfect calculation, where the theoretical result is equal to the experimental data. Reproduced from (FERREIRA <i>et al.</i> , 2011).	31
FIGURE 3.1 – Single qubit representation in the Bloch Sphere. The qubit state is represented by the orange line in the picture. The state at the top of the sphere represents $ 0\rangle$ and the state at the bottom of the sphere represents $ 1\rangle$	36
FIGURE 3.2 – Scaling of the general number field sieve (GNFS) on classical computers and Shor’s algorithm using BCDP modular exponentiation on a quantum computer, with various clock rates. The steep curves are for GNFS on a set of classical computers. The left curve is extrapolated performance based on a previous world record, factoring a 530-bit number in one month, established using 104 PCs and workstations made in 2003. The right curve is speculative performance using 1,000 times as much computing power. This could be 100,000 PCs in 2003, or, based on Moore’s law, 100 PCs in 2018. Reproduced from (HAMDI <i>et al.</i> , 2014)	38
FIGURE 3.3 – Simple quantum circuit used to test the operation of the Hadamard and X gates, and its corresponding Quantum Assembly code. The barriers (vertical gray dashed lines) is added to ensure that the compiler will not perform simplifications, such as $HH = I$; while the idle gates were inserted to ensure the measurements are done at the same time, and hence obtaining a similar level of decoherence in each qubit.	39

- FIGURE 3.4 – Results of 1024 runs of the quantum circuit in Fig. 3.3 on the quantum processor. We note a small percentage of spurious results due to noise and decoherence. 40
- FIGURE 3.5 – NV center in diamond. The vacancy is represented in gray, the nearest-neighbor and next-nearest-neighbor carbon atoms to the vacancy in black and the substitutional nitrogen atom in cyan. 41
- FIGURE 3.6 – Schematics of the three NV center MOs responsible for the center’s observable properties in the vicinity of the vacancy and their energy ordering. The vacancy is represented in white, the nearest-neighbor carbon atoms to the vacancy in black and the substitutional nitrogen atom in brown. Red and blue components represent positive and negative contributions to the MOs, respectively. The band gap induced energy levels are shown at the right, without considering spin-orbit and spin-spin interactions. Reproduced from (DOHERTY *et al.*, 2011). 42
- FIGURE 3.7 – (a) Band diagram for the NV^- calculated using density functional theory. Reproduced from (GALI *et al.*, 2008). (b) Configuration coordinate diagram. Reproduced from (GORDON *et al.*, 2013). (c) Many-body diagram for the NV^- transitions. The primary transition between triplet ground and excited states is predominantly spin conserving. Decay via the intermediate singlets gives rise to spin polarization by preferentially switching spin from $m_s = \pm 1$ to $m_s = 0$ 43
- FIGURE 3.8 – (a) An example of a quantum circuit, which implements an algorithm whose function is to decouple the qubit state from a dephasing bath state, and (b) its experimental implementation using an NV^- center. In this example, ^{14}N nuclear spin is used as an ancilla (‘a’), and the electron spin of the NV center (‘q’) is subjected to noise (lightning bolt) due to the spin bath (‘b’) of the ^{13}C of the bulk diamond and possibly subjected to the action of unitary gates U. The entangling gates, represented in (a) by the circle with a plus sign inside and a vertical extension, are controlled-NOT gates. The shaded region is a coherent feedback gate implemented by a controlled Pauli-Z gate (‘Z’). Hadamard gates (‘H’) prepare and read out a superposition state of the qubit, $|\phi\rangle_q = (|0\rangle + |1\rangle)/\sqrt{2}$. Figure adapted from (HIROSE; CAPPELLARO, 2016). 46

- FIGURE 3.9 – (a) 5-level model graph detailing the allowed transitions as well as their rate. (b) Simulation of the time-resolved emission for an ensemble whose centers were previously initialized and manipulated to a specific initial state. (c) Temporal evolution of the probability of being in each one of the states to a center who was previously initialized and manipulated to a superposition state with 40% probability of being in the dark state ($|g_1\rangle$) and 60% probability of being in the bright state ($|g_0\rangle$). 47
- FIGURE 3.10 –(a) Simulation of the time-resolved emission for an ensemble whose centers were previously initialized and manipulated to the dark state and to the bright state. (b) Experimental result measured using confocal microscopy. Reproduced from (DOHERTY *et al.*, 2013). . . . 51
- FIGURE 4.1 – (a) Schematic representation of a Kohn-Sham band structure with the Valence Band Maximum and Conduction Band Minimum with half-occupation, as considered on the DFT-1/2 method; and (b) Extension of the DFT-1/2 scheme for defect levels within the band gap. 54
- FIGURE 4.2 – (a) 215-atom supercell used to simulate the defect avoiding spurious interactions among images. (b) NV⁻ center and its surrounding atoms, representing the vacancy as a gray shadow. In both images, Brown, bluish-gray and red circles represent, respectively, the host carbon atoms, the nitrogen atom, and the three carbon atoms neighboring the vacancy. The images have been produced with help of the VESTA software. (MOMMA; IZUMI, 2011) 56
- FIGURE 4.3 – CUT determination for the DFT-1/2 corrections. The corrections have been performed sequentially for each geometry, in the following order: C_{Bulk} , N, C_{Defect} . (a) Band gap of pure diamond as a function of the CUT for the 0.25 electron removal from the C_{Bulk} atoms' $2p$ orbital; (b) Transition energy on the ground state's geometry as a function of the CUT of the nitrogen atom, with C_{Bulk} corrected; (c) Transition energy on the ground state's geometry as a function of the CUT of the C_{Defect} atoms, with C_{Bulk} and N corrected; (d) Transition energy on the excited state's geometry as a function of the CUT of the nitrogen atom, with C_{Bulk} corrected; (e) Transition energy on the excited state's geometry as a function of the CUT of the C_{Defect} atoms, with C_{Bulk} and N corrected. 58

- FIGURE 4.4 – Supercell band structures, around the gap region and along some special high symmetry directions in the cubic BZ, for the structural geometries of the NV- center in the (a) ground state and (b) excited state. The blue and red lines represent, respectively, the spin-up and spin-down energy levels. The occupied states related to the defect are indicated by \uparrow and \downarrow arrows. Both results have been obtained with bulk and local corrections. The direct band gap is a consequence of the supercell band folding. 61
- FIGURE 4.5 – (a) Orthogonal cell used to perform the structural relaxation of the w-GaN. (b) 432 atoms supercell used to simulate the defect, avoiding spurious interactions among images. In both images, gray and red spheres represent, respectively, the bulk Gallium and Nitrogen atoms, while the blue, black and orange spheres represent, respectively, the Chromium atom, the three Gallium atoms neighboring the vacancy and the three Nitrogen atoms neighboring the Chromium atom. The images have been produced with help of the VESTA software.(MOMMA; IZUMI, 2011) 64
- FIGURE 4.6 – Schematic band diagram for the $\text{Cr}_{\text{Ga}}\text{V}_{\text{N}}^+$ center, obtained via first-principles calculations after applying the correction to the bulk atoms. 65
- FIGURE 5.1 – Coordinates for the mathematical formulation of the dihydrogen cation system. 70
- FIGURE 5.2 – (a) Total energy as a function of the electric field and the λ coefficient, for a fixed value of $R = R_{min}$. The values of λ which maximize and minimize the total energy for each field strength F are given by the red and blue dashed lines in the contour plot (b). 72
- FIGURE 5.3 – The surface plot represents the values that the wavefunction along the z axis for a range of values of the electric field. One of the hydrogen nucleus is at $z = 0$, while the other is at $z = R_{min} = 1.3\text{\AA}$. 73
- FIGURE 5.4 – (a) Probability of finding the electron around ions 1 (blue) and 2 (red) calculated using the LCAO model. (b) Comparison between the normalized probabilities calculated with the LCAO model (solid lines) and the DFT simulation (dashed lines) 74

- FIGURE 5.5 – Band structures of $\text{ZrSe}_2/\text{SnSe}_2$ heterostructure for different values of the vertical electric field. The inset in (a) shows the positive field orientation is considered from the ZrSe_2 layer to the SnSe_2 layer. The color of a dot in a Bloch band represents the relative contribution of each monolayer to the eigenvalue. The VBM is chosen as energy zero. 76
- FIGURE 5.6 – Qualitative representation of the squared moduli of the wavefunctions for states $|0\rangle$ and $|1\rangle$ for positive (a), vanishing (b), and negative (c) electric fields. 77
- FIGURE 5.7 – Conduction-band energy level diagram versus gate-field strength F together with the localized electron states for an uncoupled system $|A\rangle$ and $|B\rangle$ (dashed lines) with eigenenergies E_A and E_B , respectively. The hybridization of the states for the coupled system results in new eigenstates $|0\rangle$ and $|1\rangle$, with eigenenergies E_0 and E_1 , respectively, and anticrossing energy Δ_{AC} (solid lines). For strong fields the qubit eigenstates are well approximated by $|A\rangle$ and $|B\rangle$, but for fields values around F_{AC} the eigenstates are strongly delocalized. For the null field, $E_B - E_A = \Delta E_C$, *i.e.*, the conduction band discontinuity. 78
- FIGURE 5.8 – Difference between the eigenenergies $E_1 - E_0$ as a function of the vertical electric field. 79
- FIGURE 5.9 – Weights $|\alpha_\psi|^2$ (red) and $|\beta_\psi|^2$ (blue), for $|\psi\rangle$ equals $|0\rangle$ (solid lines) and $|1\rangle$ (dashed lines), as a function of the applied vertical electric field. The inset represents the area of the Bloch sphere in which $|0\rangle$ and $|1\rangle$ are comprised for the considered electric fields ($|F| < 0.3\text{V}/\text{\AA}$) (light gray), and for small fields ($|F| < 0.1\text{V}/\text{\AA}$) (dark gray) considering a generic azimuthal angle ϕ . The horizontal axis indicates the direction of the vector $\hat{v} = \cos\phi\hat{x} + \sin\phi\hat{y}$ in the xy-plane. 80
- FIGURE 5.10 – Weights $|\alpha_h|^2$ (red, solid line) and $|\beta_h|^2$ (blue, solid line), as a function of the applied vertical electric field. The dashed lines indicate the weights for the maximum valence band state at Γ and the dotted lines indicate the weights for the maximum valence band state at the reciprocal space position of the VBM for $F = -0.3\text{V}/\text{\AA}$ 82
- FIGURE A.1 – Coordinates for the mathematical formulation of the dihydrogen cation system. 95

List of Tables

TABLE 4.1 –	Orbital character of the defect levels and fractions of an electron to be removed from and added to each potential (denoted by ξ and ζ , respectively).	59
TABLE 4.2 –	Vertical absorption (E_{Ab}), vertical emission (E_{Em}), zero-phonon line (E_{ZPL}), Stokes shift (E_S) and anti-Stokes shift (E_{aS}) energies calculated by different methods, compared to the experimental data (all values in eV).	60
TABLE 4.3 –	Transition energy between the levels of interest for different corrections. The bulk corrected potentials were applied to different combinations of atoms, in order to study the effect of considering the neighbor atoms as part of the bulk or not.	65
TABLE 4.4 –	Orbital character of the defect levels and fractions of an electron to be removed from and added to each potential (denoted by ξ and ζ , respectively). Only the defect and its first neighbors were considered in this table.	66
TABLE 5.1 –	Difference in energy between the conduction and valence bands of several pairs of materials, <i>i.e.</i> , the band discontinuities ΔE_C and ΔE_V (in eV). In green are the systems that present a misalignment lower than 0.3 eV, in yellow the ones that are between 0.3 eV and 0.6 eV and in red the ones that are greater than 0.6 eV. All the values are given in eV.	83
TABLE 5.2 –	Difference in energy between the conduction band minimum of the materials in the columns with the valence band maximum of the materials in the rows. In green are the systems that present a misalignment lower than 0.3 eV, in yellow the ones that are between 0.3 eV and 0.6 eV and in red the ones that are greater than 0.6 eV. All the values are given in eV.	84

Contents

1	INTRODUCTION	17
1.1	Motivation	17
1.2	Objective	18
1.3	Overview	19
2	THEORETICAL METHODOLOGY	21
2.1	Formulation	21
2.1.1	Quantum Theory of a Crystalline Solid	21
2.1.2	Hohenberg-Kohn Theorems	22
2.1.3	Kohn-Sham Equations	23
2.1.4	Projector Augmented-Wave	25
2.1.5	Periodic Boundary Conditions and the Supercell Method	26
2.2	Hybrid Functionals	27
2.3	Approximate quasi-particle corrections: DFT-1/2	28
2.4	van der Waals correction	31
2.5	Obtaining differences in total energy through eigenvalues	32
2.6	Vienna Ab-Initio Simulation Package	33
3	QUBITS AND THE CASE OF THE NV^- CENTER IN DIAMOND	35
3.1	Quantum bits and quantum gates	35
3.2	Quantum algorithms and Quantum speedup	37
3.3	IBM Quantum Experience	38
3.4	The NV^- Center in Diamond	40
3.5	Using the Qubit	44

4	THE DFT-1/2 LOCAL CORRECTION TO DEFECT LEVELS . . .	52
4.1	The Local Correction	52
4.2	Benchmarking with the NV ⁻ Center in Diamond	56
4.2.1	Computational details	56
4.2.2	Procedure	57
4.2.3	Results and Discussion	61
4.3	Chromium-Vacancy in w-GaN	63
4.3.1	Characteristics of the Host	63
4.3.2	Computational details	63
4.3.3	Simulating the Defect	64
5	QUBIT BASED ON VAN DER WAALS HETEROSTRUCTURES . . .	68
5.1	Quantum superposition and two-dimensional systems	68
5.2	A Toy Model for the Dihydrogen Cation Under an Axial Electric Field	69
5.2.1	Formulation	69
5.2.2	Results and Discussion	72
5.3	The van der Waals Qubit	74
5.3.1	Computational details	74
5.3.2	Effect of vertical electric field on band structure	75
5.3.3	Usage as qubit:	80
5.3.4	Conduction by holes	81
5.3.5	Similar systems	82
6	CONCLUSION	85
	BIBLIOGRAPHY	87
	APPENDIX A – FORMULATION OF THE DIHYDROGEN CATION TOY MODEL	95
	APPENDIX B – PUBLICATIONS IN PERIODICALS	99

APPENDIX C – PRESENTATIONS AT CONFERENCES	100
ANNEX A – PUBLISHED PAPERS	101
GLOSSARY	112

1 Introduction

1.1 Motivation

Shortly after their creation, during the last decades of the 20th century, computers changed society. More than an end in themselves, they are important tools that have been accelerating the development of new technologies and even their own evolution. Despite all the progress, there are still problems that are very difficult to solve, no matter how fast computers become. For some of these problems, quantum computation arises as a possible solution in the near future.

A quantum computer is a computation system that makes direct use of quantum phenomena, such as entanglement and superposition, to perform operations on data. Prior to their complete development, there are already proposals of efficient algorithms for some problems, such as the factorization of large prime numbers (SHOR, 1997), or the simulation of quantum systems, as predicted by Feynman (FEYNMAN, 1982) and already realized by (WANG *et al.*, 2014) for a simple case, the helium hydride cation, HeH^+ .

The fundamental building blocks of a quantum computer are called qubits, in analogy to the bits present in classical computers. A qubit is a quantum system consisting of two energy levels, usually labeled $|0\rangle$ and $|1\rangle$. From the axioms of Quantum Mechanics, we have that any normalized linear combination with complex coefficients of these states is also valid states of the system, and from the Born rule (BORN, 1954), the square of the magnitude of the coefficient is the probability of a measurement has its respective basis vector as the outcome.

In order to implement an universal quantum computer (DEUTSCH, 1985), various technological barriers must be overcome. Among these challenges is the physical realization of qubits, since most systems suffer from loss of coherence. In principle, an isolated atom would provide an intuitive quantum bit, whose properties are well-understand. Unfortunately, it is very difficult to use isolated atoms in a quantum device, since it requires additional apparatus such as magneto-optical traps to fix them in space.

This scenario motivates the use of point defects in semiconductors or insulators, since

their electronic properties are similar to the properties of isolated atoms or molecules, with the intrinsic advantage of being held into place by the surrounding crystal, as it is the case for all solid state qubits. Moreover, the dynamics of such systems presents the same fundamental concepts of lasers. Therefore, the study relates to other technological applications of current interest, such as terabit optical data channels (WANG *et al.*, 2017).

Crystal growth and controlled incorporation of defects in semiconductors (doping) have been largely used to engineer materials that can be used as electronic devices. By judicious choice of the dopant and its respective concentrations, a very broad gamma of devices can be realized. These devices, however, don't make direct use of the quantum properties of the defects, such as superposition and entanglement. Nonetheless, the technologies that are already known by the semiconductor industry offers various tools for the solid state quantum systems that are currently being developed.

One prominent candidate for solid state qubit is the negatively-charged nitrogen-vacancy defect (NV^- center) in bulk diamond (DOHERTY *et al.*, 2013) since it is an individually addressable quantum system that may be initialized, manipulated, and measured with high fidelity even at room temperature (WEBER *et al.*, 2010). It is also the platform on which the aforementioned quantum simulation of HeH^+ was realized (WANG *et al.*, 2014). However, it is of great interest to find other analog systems hosted in different materials that would enable for better integration with microelectronic, photonic and micromechanical integration. Identifying defects with similar properties in other materials would enhance device design and possibly result in superior performance.

On the other hand, as with the bits in classical computing, it is highly desirable to have several different methods to store and process information, since each of them has its positive and negative aspects, and may be more or less interesting depending on the application intended. Examples in classical computing are the magnetic domains in hard disks, transistors in RAM modules, reflective and opaque regions in a CD-R, or even white and black regions in a barcode. There are already several proposals for qubits as well, such as the polarization of light (O'BRIEN *et al.*, 2003), energy levels of ultracold atoms in an optical lattice (SCHNEIDER; SAENZ, 2012), and electron spin orientations (LAUCHT *et al.*, 2016). In order to contribute to this matter, we propose a novel qubit concept based on van der Waals heterostructures, which directly dialogues with the fast-paced growing technology of 2D materials.

1.2 Objective

The objective of the present study is to use first principle calculations in the search of materials and systems that would be suitable for the physical implementation of quantum

bits and other quantum information devices. This is addressed on two fronts:

First, qubits based on deep center defects in solids are studied, and a new theoretical method for the calculation of the optical transition energies between the defect levels of interest for their operation as a qubit is proposed. The proposal is based on a methodology developed at the *Grupo de Materiais Semicondutores e Nanotecnologia* (GMSN) for precise band-gap calculations called LDA-1/2, and it has the required accuracy and low computational cost required for a systematic search for new combinations of host materials and complex defects. The method is benchmarked with the NV^- center in diamond, which has already been extensively studied both theoretically and experimentally. Finally, the method is applied on other possible host material, GaN, since it is more technologically mature than diamond and is, therefore, more suitable for the implementation of quantum computers in the present date.

Second, consonant with the research conducted at the GMSN on 2D materials and their heterostructures, a novel concept of a qubit is proposed. The qubit is based on the spatial quantum superposition that can be obtained for some combinations of 2D materials in gated van der Waals heterostructures. For this reason, we refer to it as the vdW qubit. One of these possible combinations, namely the $ZrSe_2/SnSe_2$, is simulated theoretically, as well as its manipulation using an electric field applied at the gate, and the results are promising. Finally, we provide a table with combinations between ten 2D crystals that allows the identification of cases where the natural bands' discontinuities are small and, therefore, have a possible application as a vdW qubit.

In both cases, toy models that were developed to aid in the understanding of the physical phenomena involved are presented and discussed.

1.3 Overview

In chapter 2, Density Functional Theory is briefly explained. The Hohenberg-Kohn theorems and the Kohn-Sham equations are presented, and a motivation for the supercell method is given. Then, we demonstrate that it is possible to obtain the energies of electronic transitions between two localized levels within the band gap directly from the Kohn-Sham eigenvalues in supercell calculations. In the latter part, we introduce the DFT-1/2 method for gap correction and present general aspects of its formulation.

In chapter 3, we introduce some concepts on quantum computing, and an illustrative experiment on a real quantum processor is performed, using the IBM Quantum Experience platform. Then, the structure and properties of the NV center in diamond are addressed. Some experimental methods to initialize, manipulate and measure a single NV^- center are described. In the latter part, we introduce a simplified model that helps to clarify how

the spin dynamics determines the luminosity. This model also presents good qualitative results for the luminescence in function of time for various initial conditions. A comparison of these results with experimental data is given.

In Chapter 4, we propose an extension to the method DFT-1/2 to correct the defect energy levels within the band gap and thus allowing the accurate calculation of the electronic transition energies with low computational cost. We also show that together with a standard DFT calculation of the anti-Stokes shift, we are able to determine other two energies of experimental interest: The Stokes shift and the Zero Phonon Line. The method is then benchmarked with the NV^- center in diamond, whose energies have already been determined, both theoretically and experimentally. The application of the method to the NV^- center is explained in detail, in order to exemplify its use and to highlight some important aspects. Finally, we present the results of the application of this methodology in a complex defect in wurtzite Gallium Nitride.

Finally, in chapter 6, we demonstrate the possibility of using a gated vdW heterostructure to implement spatial quantum superpositions of electron and hole states. A charge qubit based on the $ZrSe_2/SnSe_2$ vdW heterostructure is proposed. The quantum state is prepared by application of a vertical electric field. It may be manipulated by short pulses in this field, and measurement is possible via electrical currents. The qubit state is robust and compatible with current 2D technology. The results show the potential use of vdW heterostructures as a platform for qubit devices. In order to highlight important aspects, before the actual proposal of the qubit, a toy model that presents analogous behavior is developed and analyzed.

2 Theoretical Methodology

This chapter introduces topics on Density Functional Theory that directly relate to this work. The possibility of determining the differences in total energy resulting from an electronic excitation through the Kohn-Sham eigenvalues under certain conditions is demonstrated. The electronic gap correction method DFT-1/2 is presented.

2.1 Formulation

The text in this section (2.1) was adapted from the paper *A Bird's-Eye View of Density-Functional Theory*, by Klaus Capelle. (CAPELLE, 2006) This section intends to briefly introduce the DFT concepts that will be directly employed in this study. More advanced readers may refer to (ENGEL; DREIZLER, 2011)

2.1.1 Quantum Theory of a Crystalline Solid

DFT is one of the most popular and successful quantum mechanical approaches to matter. Therefore, to better understand its concepts, it is useful to understand how it is derived from the quantum theory, recalling some important concepts.

In the quantum formalism, the state of a system may be described as a wavefunction Ψ . The time-independent Schroedinger equation may be written as

$$H\Psi = E\Psi, \quad (2.1)$$

where H is the Hamiltonian operator and E is the energy eigenvalue. For a crystalline solid, the Hamiltonian can be separated into five terms,

$$H = \hat{T}_{nucleus} + \hat{T}_{electron} + \hat{U}_{electron-electron} + \hat{V}_{nucleus-electron} + \hat{W}_{nucleus-nucleus} \quad (2.2)$$

where \hat{T} stands for the kinetic energy operator and \hat{U} , \hat{V} and \hat{W} stands for the coulombic interaction operators.

Since we are concerned with a very large number of particles, it is not possible to exactly solve the Schroedinger equation. Therefore, we must consider some approximations. The first one is known as the Born-Oppenheimer approximation, and it consists in considering that the nuclei are static. It is based on the fact that the nuclei are much more massive than the electrons, and thus change very slowly in the time scale of the electronic movement. This introduces a great simplification, since the nuclei kinetic energy and the nucleus-nucleus interaction become constants, corresponding to a global shift in energy, and hence they can be removed from the calculation. Moreover, we may describe the nucleus-electron interaction as a single-body potential, and hence write the Hamiltonian of the system on the Hartree atomic units as

$$H = \hat{T} + \hat{V} + \hat{U} \quad (2.3)$$

$$= \sum_{i=1}^N \hat{T}_i + \sum_{i=1}^N \hat{V}_i + \sum_{i=1}^N \sum_{j>i}^N \hat{U}_{ij} \quad (2.4)$$

$$= \sum_{i=1}^N -\frac{\nabla_i^2}{2} + \sum_{i=1}^N \sum_{k=1}^M -\frac{Z_k}{|\mathbf{r}_i - \mathbf{R}_k|} + \sum_{i=1}^N \sum_{j>i}^N \frac{1}{|\mathbf{r}_i - \mathbf{r}_j|}, \quad (2.5)$$

where M is the total number of nuclei, N is the total number of electrons, \mathbf{r}_i is the position of the i -th electron, Z_k and \mathbf{R}_k are the atomic number and the position of the k -th nucleus, respectively.

Even though the Born-Oppenheimer approximation simplification is significant, it still unfeasible to solve the N-body problem. In this scenario, an ingenious approach is to consider the problem in terms of the number density of electrons, defined as

$$n(\mathbf{r}) = N \int |\Psi(\mathbf{r}, \mathbf{r}_2, \dots, \mathbf{r}_N)|^2 d^3r_2 \dots d^3r_N, \quad (2.6)$$

which have only 3 spatial degrees of freedom, instead of $3N$.

2.1.2 Hohenberg-Kohn Theorems

Hohenberg and Kohn demonstrated that the ground state density $n(\mathbf{r})$ completely specifies the ground state wave function $\Psi(\mathbf{r}_1, \mathbf{r}_2, \dots, \mathbf{r}_N)$, despite the fact that the later have N times more degrees of freedom than the former. (HOHENBERG; KOHN, 1964) This is possible because besides reproducing the density n , Ψ must minimize the energy, due to the variational principle. More precisely, the Hohenberg-Kohn (HK) theorems, which relate to any system consisting of electrons moving under the influence of an external potential, may be stated as:

Theorem 2.1 The external potential (and hence the total energy), is a unique func-

tional of the electron density.

Theorem 2.2 The functional that delivers the ground state energy of the system gives the lowest energy if and only if the input density is the true ground state density.

An important corollary to the first HK theorem is that all properties of a system are determined from only the ground state electron density. Since the ground state density defines the Hamiltonian, it also defines all its eigenfunctions.

2.1.3 Kohn-Sham Equations

One of the most successful methods to calculate the electronic structure of many particles systems via DFT is to solve the so-called Kohn-Sham (KS) equations. (KOHN; SHAM, 1965) Motivated by the enormous complexity of solving a system of interacting electrons, it is desirable to define a fictitious system of non-interacting particles whose density is the same as the density of the problem to be solved. We will denote the ground state wave function of this fictitious system as $\Phi(\mathbf{r}_1, \mathbf{r}_2, \dots, \mathbf{r}_N)$.

Considering that the non-interacting Hamiltonian consists only of one single-particle potential $v_{ks}(\mathbf{r})$ and the kinetic energy operator, and that the potential energy depends only on the density and not on the particular wave function of the system, the KS wave function of density $n(\mathbf{r})$ can be defined as the wave function that yields $n(\mathbf{r})$ and has least kinetic energy. Consequently, it is possible to write the KS wave function as a single Slater determinant of the so-called Kohn-Sham orbitals $\phi_i(\mathbf{r})$, $i = 1, 2, \dots, N$, and thus write the density as

$$n(\mathbf{r}) = \sum_i |\phi_i(\mathbf{r})|^2, \quad (2.7)$$

Since exact and simple expressions for both the single particle kinetic energy and the Hartree energy are known, these terms are explicitly written in the energy functional

$$E[n] = T[n] + U[n] + V_{ext}[n] \quad (2.8)$$

$$= T_0[n] + U_H[n] + V_{ext}[n] + E_{xc}[n] \quad (2.9)$$

$$= \langle \Phi[n] | \hat{T} | \Phi[n] \rangle + \frac{1}{2} \int d^3r d^3r' \frac{n(\mathbf{r})n(\mathbf{r}')}{|\mathbf{r} - \mathbf{r}'|} + \int d^3r v_{ext}(\mathbf{r})n(\mathbf{r}) + E_{xc}[n] \quad (2.10)$$

$$= -\frac{1}{2} \sum_{i=1}^N \int \phi_i^*[n](\mathbf{r}) \nabla^2 \phi_i[n](\mathbf{r}) + \frac{1}{2} \int d^3r d^3r' \frac{n(\mathbf{r})n(\mathbf{r}')}{|\mathbf{r} - \mathbf{r}'|} + \int d^3r v_{ext}(\mathbf{r})n(\mathbf{r}) + E_{xc}[n] \quad (2.11)$$

where $E_{xc}[n]$ is the exchange-correlation energy defined as $E_{xc} = T - T_0 + U - U_H$, whose functional form is not known and therefore must be approximated. Among several possibilities, in this work we consider the purely theoretical functional PBE (PERDEW

et al., 1996a), which is one of the most popular and reliable approximations for E_{xc} . It belongs to a class of approximations called GGA, or *Generalized Gradient Approximation*, which has the general form:

$$E_{xc}^{GGA} = \int d^3r f(n(\mathbf{r}), \nabla n(\mathbf{r})) \quad (2.12)$$

Minimizing the energy functional subjected to the restriction of a fixed number of electrons, one obtains the set of uncoupled equations

$$\left\{ -\frac{1}{2}\nabla^2 + \int d^3r' \frac{n(\mathbf{r}')}{|\mathbf{r} - \mathbf{r}'|} + v_{ext}(\mathbf{r}) + v_{xc}(\mathbf{r}) \right\} \phi_i(\mathbf{r}) = \varepsilon_i \phi_i(\mathbf{r}) \quad (2.13)$$

and identifies the KS potential as

$$v_{ks}(\mathbf{r}) = \int d^3r' \frac{n(\mathbf{r}')}{|\mathbf{r} - \mathbf{r}'|} + v_{ext}(\mathbf{r}) + v_{xc}(\mathbf{r}) \quad (2.14)$$

where v_{xc} is defined as the functional derivative of the exchange-correlation energy with respect to the density, and the integral term is called the Hartree potential (denoted v_H).

Since the v_H and v_{xc} depend on n , which depends on the ϕ_i , which in turn depend on v_{ks} , the problem of solving the KS equations is nonlinear and is usually solved through a self-consistency cycle, which consists in starting with an initial guess for n , calculate v_{ks} , solve the system of KS equations for the ϕ_i , calculate the new density and iterate until convergence is reached. At this point, the KS orbitals yield the density which yields themselves; hence the name ‘‘self-consistency’’. The Fig. 2.1 schematically represents the

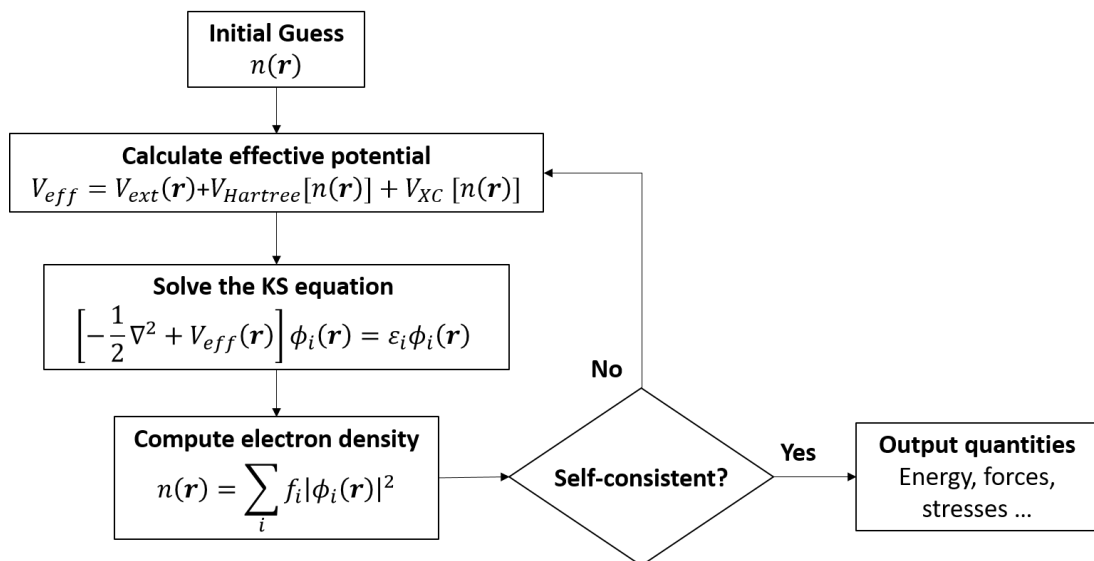


FIGURE 2.1 – Flowchart of the algorithm used in the self-consistent solution of the Kohn-Sham equations.

major aspects of the procedure.

2.1.4 Projector Augmented-Wave

Although several approximations are made, DFT solutions still are rather costly from a computational point of view. Even when the procedures explained so far are employed, there are still two major concerns in the description of solids:

- The singularity of the Coulomb potential renders too large the number of plane waves necessary to describe it adequately, especially when compared to non-singular potentials.
- Heavier elements in the periodic table require more electrons to be simulated, rendering simulations more costly and complex.

Several methods try to solve these problems, such as the pseudopotentials (HELLMANN, 1935; VANDERBILT, 1990), the Linearized Augmented-Plane-Wave (LAPW) (ANDERSEN, 1975), and the Projector Augmented-Wave (PAW) (BLÖCHL, 1994; KRESSE; JOUBERT, 1999). In this work, we use the PAW method, which tries to combine in a single approach the accuracy of the “all-electron” methods (such as the LAPW) with the efficiency of the pseudopotential methods.

In the PAW method, the problem of the plane waves describing the wavefunction is firstly solved by determining “augmentation spheres” of given radii around the atoms. Inside these spheres, *i.e.*, in the core region, the wavefunction oscillates rapidly in space due to the Coulomb potential. Outside these spheres, *i.e.*, in the interstitial region, the wavefunction is smoother and can easily be described using plane waves.

The method describes how to build a transformation of the physical quantities between the all-electron Kohn-Sham orbitals space and a pseudo-space of plane waves. Such a transformation can be written as (ANDERSEN, 1975)

$$|\Psi\rangle = \hat{\mathcal{T}}|\tilde{\Psi}\rangle, \quad (2.15)$$

where $|\Psi\rangle$ represents the real wavefunction and $|\tilde{\Psi}\rangle$ represents the pseudo-wavefunction. Since these two functions must coincide in the region outside the spheres, the transformation must be of the form

$$\hat{\mathcal{T}} = \hat{\mathbb{1}} + \sum_a \hat{\mathcal{T}}^a, \quad (2.16)$$

where $\hat{\mathbb{1}}$ is the identity operator and $\hat{\mathcal{T}}^a$ only acts in their respective augmentation spheres,

labeled by the index a . It is possible to show that these operators can be calculated as

$$\hat{\mathcal{T}}^a = \sum_i (|\phi_i^a\rangle - |\tilde{\phi}_i^a\rangle) \langle \tilde{p}_i^a|, \quad (2.17)$$

where i is a index for both angular and magnetic quantum numbers, $|\phi_i^a\rangle$ are the radial solutions of the Kohn-Sham equations for the atoms, $|\tilde{\phi}_i^a\rangle$ are the corresponding pseudo-orbitals, and $|\tilde{p}_i^a\rangle$ are smooth projector functions satisfying the following orthogonality and completeness relations inside the augmentation spheres:

$$\begin{aligned} \langle \tilde{p}_i^a | \tilde{\phi}_j^a \rangle &= \delta_{ij} \\ \sum_i |\tilde{\phi}_j^a\rangle \langle \tilde{p}_i^a| &= \hat{1}. \end{aligned} \quad (2.18)$$

The true wavefunction can be written as

$$|\Psi\rangle = |\tilde{\Psi}\rangle + \sum_a \sum_i |\phi_i^a\rangle \langle \tilde{p}_i^a | \tilde{\Psi}\rangle - \sum_a \sum_i |\tilde{\phi}_i^a\rangle \langle \tilde{p}_i^a | \tilde{\Psi}\rangle = |\tilde{\Psi}\rangle + |\Psi^1\rangle - |\tilde{\Psi}^1\rangle. \quad (2.19)$$

The PAW method, therefore, divides the wavefunction in three terms: (i) a pseudo-wavefunction $|\tilde{\Psi}\rangle$, related to a pseudopotential and identical to $|\Psi\rangle$ outside the augmentation spheres; (ii) a component $|\Psi^1\rangle$ that corrects the behavior of the wavefunction close to the nuclei; and (iii) a component $|\tilde{\Psi}^1\rangle$ that cancel the pseudo-function on the atomic site.

By means of the transformation $\hat{\mathcal{T}}$, it is possible to obtain, in a formal manner, the expectation value of physical quantities such as the electronic density in a pseudopotential calculation.

2.1.5 Periodic Boundary Conditions and the Supercell Method

One way to apply DFT calculations to solids is to assume that the crystal is infinite. Due to the translational symmetry, it is possible to limit the calculation to a single unit cell, applying periodic boundary conditions. The KS orbitals then can be written in the form

$$\phi_{\mathbf{k}}(\mathbf{r}) = e^{i\mathbf{k}\cdot\mathbf{r}} u_{\mathbf{k}}(\mathbf{r}), \quad (2.20)$$

where the vector \mathbf{k} is called the crystal momentum and u is a function with the same periodicity of the crystal lattice, *i.e.* $u_{\mathbf{k}}(\mathbf{r} + \mathbf{R}) = u_{\mathbf{k}}(\mathbf{r})$, for all lattice vectors \mathbf{R} . This result is known as the Bloch theorem (BLOCH, 1929).

A practical consequence of this approach in the calculation of crystalline defects is that if a defect is placed in a unit cell, it is infinitely replicated throughout the crystal.

This corresponds to a large concentration of defects and consequently introduces spurious interactions between them. In order to minimize such effects, one of the most used techniques is to place the defect in a very large unit cell, commonly called a *supercell*, and hence separating the defect of its images by several atomic layers. One signature of a properly isolated defect is the reduction of the defect levels dispersion within the electronic band structure, indicating a localized orbital.

Since the number of atoms grows with the cube of the unit cell size for three-dimensional systems, this method can become very computational costly.

2.2 Hybrid Functionals

Since DFT deals well with correlation but not with the exchange functional, attempts to perform a mixed approach together with the Hartree-Fock (HF) method (HARTREE, 1928; FOCK; LENINGRAD, 1930), which has an exact exchange, were proposed.

For this purpose, the use of hybrid functionals was proposed (BECKE, 1993), in which the hybrid exchange-correlation energy E_{xc}^{hyb} is composed by a mixture of the DFT and HF energies, following a linear relationship such as

$$E_{xc}^{hyb} = E_x^{HF} + (1 - a)(E_x^{DFT} - E_x^{HF}) + E_c^{DFT}, \quad (2.21)$$

where a is the mixing parameter, originally proposed as $a = 1/2$ (BECKE, 1993). In the case of $a = 1/4$, derived with perturbation theory, and using the GGA functional PBE for the DFT exchange and correlation energies, the hybrid functional PBE0 is obtained (PERDEW *et al.*, 1996b; ADAMO; BARONE, 1999). Although the energy is improved in these systems, the convergence starts to be a problem in solids due to the long-range integral from HF calculations. In order to circumvent this problem, the exact exchange term was divided into two parts: a short-range and a long-range one (HEYD *et al.*, 2003). In this case, the exchange-correlation energy is written as

$$E_{xc}^{HSE06} = \frac{1}{4}E_x^{HF,sr}(\mu) + \frac{1}{4}E_x^{GGA,sr}(\mu) + E_x^{HF,lr} + E_c^{GGA}, \quad (2.22)$$

having μ as an adjustable “screening” parameter, and with “sr” and “lr” standing for short range and long range, respectively. The exchange-correlation is better represented when the non-locality is included in the exchange energy. This also describes partially quasi-particle effects due to electronic excitations and, thus, band structures calculated with hybrid functionals usually present considerably better predictions for the band gap of semiconductors and insulators.

This is a reason for the success of hybrid functionals, especially when its complexity

is reduced by means of an artifice such as the one employed in HSE06. However, HSE06 calculations require more computational time than standard DFT and can be up to two order of magnitude slower than PBE calculations.

2.3 Approximate quasi-particle corrections: DFT-1/2

It is a well-known fact in the solid state physics literature that the Kohn-Sham band gap of semiconductors and insulators are underestimated when compared to experiments (SHAM; SCHLÜTER, 1985; PERDEW; LEVY, 1983; PERDEW *et al.*, 2017). It has been shown that this effect also impairs reliable calculations of defect levels above the valence band. (RINKE *et al.*, 2009)

The methods that go beyond DFT to correct Kohn-Sham eigenvalues, such as hybrid functionals (HEYD *et al.*, 2003; HEYD *et al.*, 2006) and the GW approach, (HYBERTSEN; LOUIE, 1985) usually sharply raise the computational cost (PELA *et al.*, 2015), which is critical in large supercell calculations. One good alternative is the DFT-1/2 method (FERREIRA *et al.*, 2008; FERREIRA *et al.*, 2011), which produces results comparable to the best correction methods, but with a very reduced computational cost - essentially the same as the standard DFT. The DFT-1/2 method generalizes the Slater's transition state technique for solids, introducing approximate quasi-particle corrections which lead to accurate calculations of semiconductor band gaps.

The method assumes the Janak's theorem (Eq. 2.38) and considers the quasi-linear dependence of the eigenvalue with its own occupancy (LEITE; FERREIRA, 1971; GÖRANSSON *et al.*, 2005). By direct integration from $f_i = 0$ (unoccupied orbital) to $f_i = 1$ (occupied orbital), we obtain

$$\int_{E_i(0)}^{E_i(1)} dE = \int_0^1 \varepsilon_i(f_i) df_i, \quad (2.23)$$

where $E_i(1)$ and $E_i(0)$ are the energies of the system with $f_i = 1$ and $f_i = 0$, respectively. Assuming the linearity of ε_i with respect to f_i , we may write $\varepsilon_i(f_i) = \alpha_i f_i + \beta_i$, where α and β are constants with respect to f_i . Hence

$$E_i(1) - E_i(0) = \int_0^1 (\alpha_i f_i + \beta_i) df_i = \left(\frac{\alpha_i f_i^2}{2} + \beta_i f_i \right) \Big|_0^1 = \alpha_i \frac{1}{2} + \beta_i = \varepsilon_i(1/2). \quad (2.24)$$

Since $I_i = E_i(0) - E_i(1)$ is the ionization energy of the i -th level, and defining the self-energy as $S_i = \frac{1}{2} \frac{\partial \varepsilon_i}{\partial f_i} = \alpha_i/2$, Eq. 2.24 may be written as

$$I_i = -\varepsilon_i(1) + S_i. \quad (2.25)$$

This result shows that the ionization energy of the i -th electron requires not only the

opposite of its eigenvalue, but also its self-energy.

In the case of a semiconductor, we are usually interested in the band gap energy, G , which is defined here as the difference between the system with one excited electron and the system in the ground state. If we denote the total energy as $E = E(f_{VBM}, f_{CBM})$, where f_{VBM} and f_{CBM} are the occupations of the valence band maximum and the conduction band minimum, respectively, we may write

$$\begin{aligned}
G &= E(0, 1) - E(1, 0) \\
&= [E(0, 1) - E(0, 0)] - [E(1, 0) - E(0, 0)] \\
&= -I_{CBM} + I_{VBM} \\
&= -[-\varepsilon_{CBM}(1) + S_{CBM}] + [-\varepsilon_{VBM}(1) + S_{VBM}] \\
&= \varepsilon_{CBM}(1) - \varepsilon_{VBM}(1) + S_{VBM} - S_{CBM} \\
&= g + S_{VBM} - S_{CBM},
\end{aligned} \tag{2.26}$$

where g is the gap between Kohn-Sham eigenvalues. Eq. 2.27 shows that the gap, as defined here, is not simply the difference between eigenvalues. Moreover, it shows that the self-energy must be considered in the calculation. If we apply Eq. 2.24 in Eq. 2.26, we find that

$$G = \varepsilon_{CBM}(1/2) - \varepsilon_{VBM}(1/2), \tag{2.28}$$

that is, we may calculate the band gap as the difference between two Kohn-Sham eigenvalues, as long as they were calculated in a half occupation scenario. However, until this moment, we did not show how we can implement the half occupation scenario in a semiconductor crystal. From Eqs. 2.7 and 2.13 with the occupation variables f_i , we can rewrite the self-energy S_i as (FERREIRA *et al.*, 2008; FERREIRA *et al.*, 2011)

$$\begin{aligned}
2S_i &= \int d^3r d^3r' \frac{n_i(\mathbf{r})n_i(\mathbf{r}')}{|\mathbf{r} - \mathbf{r}'|} + \int d^3r d^3r' n_i(\mathbf{r})n_i(\mathbf{r}') \frac{\delta^2 E}{\delta n_i(\mathbf{r})\delta n_i(\mathbf{r}')} \\
&+ \int d^3r d^3r' \frac{n_i(\mathbf{r})}{|\mathbf{r} - \mathbf{r}'|} \sum_j f_j \frac{\partial n_j(\mathbf{r}')}{\partial f_i} + \int d^3r d^3r' n_i(\mathbf{r}) \frac{\delta^2 E}{\delta n_i(\mathbf{r})\delta n_i(\mathbf{r}')} \sum_j f_j \frac{\partial n_j(\mathbf{r}')}{\partial f_i}
\end{aligned} \tag{2.29}$$

were, compactly, we denote $n_i(\mathbf{r}) = \phi_i^*(\mathbf{r})\phi_i(\mathbf{r})$. The first term of the equation was the motivation to attribute the name self-energy to the variable S_i . The self-energy can be written in terms of a potential V_S of self-energy, defined as

$$S_i = \int d^3r n_i(\mathbf{r})V_S(\mathbf{r}) \tag{2.30}$$

that is, we may write $V_S(\mathbf{r})$ as

$$2V_S(\mathbf{r}) = \int d^3r' \frac{n_i(\mathbf{r}')}{|\mathbf{r} - \mathbf{r}'|} + \int d^3r' n_i(\mathbf{r}') \frac{\delta^2 E}{\delta n_i(\mathbf{r}) \delta n_i(\mathbf{r}')} + \int d^3r' \frac{1}{|\mathbf{r} - \mathbf{r}'|} \sum_j f_j \frac{\partial n_j(\mathbf{r}')}{\partial f_i} + \int d^3r' \frac{\delta^2 E}{\delta n_i(\mathbf{r}) \delta n_i(\mathbf{r}')} \sum_j f_j \frac{\partial n_j(\mathbf{r}')}{\partial f_i} \quad (2.31)$$

It is possible to show that $\varepsilon_i(1) - S_i$, as appears in Eq. 2.25 can be obtained by solving the Kohn-Sham equations (Eq. 2.13) with V_S summed to the effective Hamiltonian (FERREIRA *et al.*, 2008). It is necessary, therefore, calculate V_S . For atoms, V_S is the difference between the potentials of the neutral atom and the half-ionized atom (FERREIRA *et al.*, 2008; FERREIRA *et al.*, 2011), that is:

$$[V(\mathbf{r})]_{f_i=1} - V(\mathbf{r})_{f_i=1/2} = V_S(\mathbf{r}) \quad (2.32)$$

In the case of an atom, this quantity can be easily calculated within DFT, In this work, this calculation was done with the well-known code ATOM (PSEUDOPOTENTIALS, 2014). Due to spherical symmetry, the correction potential depends only on $r = |\mathbf{r}|$. For a crystal, we consider that the correction V_S of one electron at the conduction band minimum and a hole at the valence band maximum can be obtained through the atomic V_S corrections for each ion in the crystal lattice. Therefore, we add the atomic V_S to the LDA potential (in the LDA-1/2 method), or in the GGA potential (in the GGA-1/2 method).

Directly summing V_S in the ions of the crystal would lead to a convergence problem: since the V_S potential has a resulting charge of $e/2$, the periodic summation to all the atoms in the solid would lead to a harmonic series, which diverges. To avoid this problem, we multiply V_S by a trimming function $\Theta(r)$, which limits the reach of the potential to a radius defined by a parameter called CUT . There are a few requisites that Θ must obey, and the function proposed in (FERREIRA *et al.*, 2008) is

$$\Theta(r) = \begin{cases} \left[1 - \left(\frac{r}{CUT}\right)^8\right]^3 & \text{if } r \leq CUT \\ 0 & \text{if } r > CUT \end{cases} \quad (2.33)$$

which has already been extensively tested and proved to yield correct results.

The CUT parameter introduced by the trimming function, which measures the reach of the DFT-1/2 correction applied to each atom of the crystal lattice. Nonetheless, it was shown that it can be determined variationally, by extremizing the band gap (FERREIRA *et al.*, 2008). Therefore, the DFT-1/2 method does not have any adjustable or semi-empirical parameter.

The results of the LDA-1/2 method are compared with the experimental data and with the results for standard LDA in Fig. 2.2 for several semiconductors. We note that the DFT-1/2 method is much more accurate than standard DFT, and the agreement of the results with experimental data is outstanding.

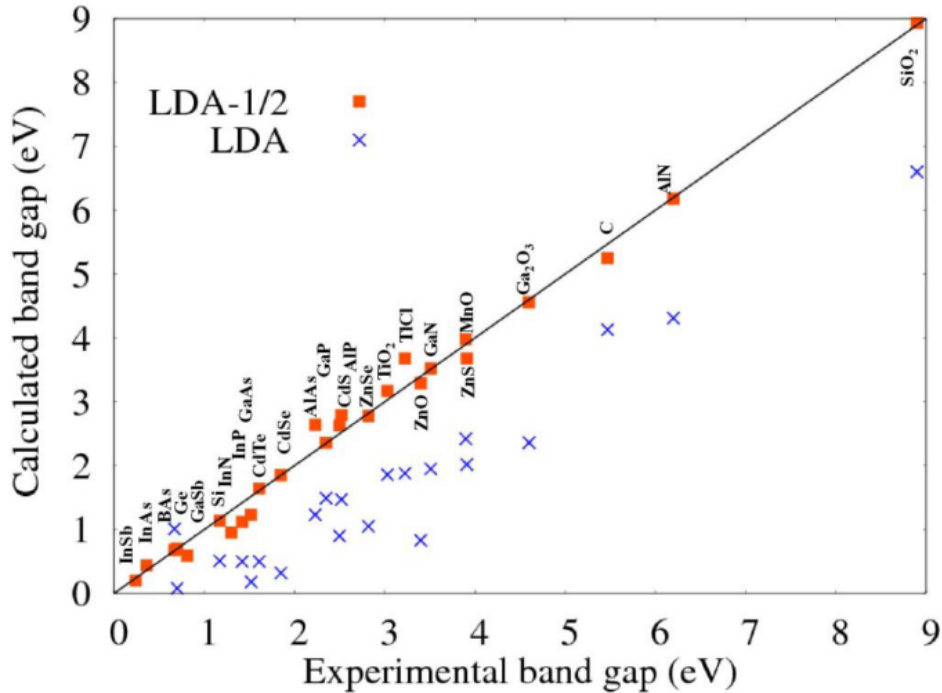


FIGURE 2.2 – Calculated and experimental band gaps for several semiconductors. The calculations were performed with both LDA and LDA-1/2 potentials. The diagonal line (in black) corresponds to a perfect calculation, where the theoretical result is equal to the experimental data. Reproduced from (FERREIRA *et al.*, 2011).

2.4 van der Waals correction

van der Waals (vdW) interactions are essential to describe 2D materials. Although LDA and GGA are reasonably successful when calculating solid systems, London dispersions are not well taken into account due to the short range of the correlation in these methods (ENGEL; DREIZLER, 2011). Considering that in the presented methods these systems are solved by a local density, correlation effects are not enough to describe their electronic behavior. For instance, two atoms separated by a long distance may be almost non-interacting from a correlation point of view, due to small wavefunction overlap. However, virtual excitations, such as ones in vdW interaction, give rise to forces which are not well described by these methods.

One possible approach for this problem is to adjust the correlation energy, dividing it

in two,

$$E_c[n] = E_c^0[n] + E_c^{nl}[n], \quad (2.34)$$

where both terms on the right hand side are non-local correlation energies. $E_c^0[n]$ is a term similar to the LDA one, while $E_c^{nl}[n]$ is responsible by the vdW interaction. It has the general form

$$E_c^{nl}[n] = \frac{1}{2} \int \int d^3r d^3r' n(\mathbf{r}) f(\mathbf{r} - \mathbf{r}') n(\mathbf{r}'), \quad (2.35)$$

with f a function of $\mathbf{r} - \mathbf{r}'$ (DION *et al.*, 2004).

In 2D systems or adsorption of molecules on surfaces, vdW interactions are necessary to predict adequate distances between the systems and binding energies. The non-locality obtained by adjusting the correlation energy, therefore, deals adequately with the vdW interaction and alters stability effects.

2.5 Obtaining differences in total energy through eigenvalues

Kohn-Sham eigenvalues do not represent the energy of the electrons which occupy these levels. However, in particular cases, it is possible to use them to compute differences in the total energy of the system. Consider a situation in which we want to obtain the energy of an electronic transition between the localized states ψ_α and ψ_β through the use of a supercell DFT calculation. Defining the total energy E in terms of partial occupations

$$E = T + U[n] + E_{xc}[n], \quad (2.36)$$

$$n(\mathbf{r}) = \sum_i f_i |\phi_i(\mathbf{r})|^2, \quad (2.37)$$

where n is the electron number density, ψ_i is the i -th Kohn-Sham orbital and f_i its occupancy, T is the kinetic energy, U is the classical Coulomb energy, and E_{xc} is the exchange-correlation functional. In order to preserve the simplicity of the argument, we are considering that we have a single sampling point on the reciprocal space, which is, in fact, a reasonable assumption, due to the band folding on large supercells. Nonetheless, the demonstration can be extended to an integral over the first Brillouin zone.

Considering all but ψ_α and ψ_β levels' occupations are fixed, we have $E = E(f_\alpha, f_\beta)$. The Janak's theorem states that

$$\frac{\partial E}{\partial f_i} = \varepsilon_i, \quad (2.38)$$

where ε_i is the i -th Kohn-Sham eigenvalue. In a large supercell, the excitation of a localized electron is a small perturbation on the Kohn-Sham operators. Thus, the position

of the eigenvalues remain unchanged and we can immediately integrate to obtain

$$\int_0^1 \frac{\partial E}{\partial f_\alpha}(f_\alpha, f_\beta) df_\alpha = \varepsilon_\alpha \int_0^1 df_\alpha \Rightarrow E(1, f_\beta) - E(0, f_\beta) = \varepsilon_\alpha, \forall f_\beta \quad (2.39)$$

and

$$\int_0^1 \frac{\partial E}{\partial f_\beta}(f_\alpha, f_\beta) df_\beta = \varepsilon_\beta \int_0^1 df_\beta \Rightarrow E(f_\alpha, 1) - E(f_\alpha, 0) = \varepsilon_\beta, \forall f_\alpha. \quad (2.40)$$

By taking $f_\beta=0$ on equation 2.39 and $f_\alpha=0$ on equation 2.40, and then performing their subtraction, we conclude that

$$\Delta E_{trans} = E(0, 1) - E(1, 0) = \varepsilon_\beta - \varepsilon_\alpha, \quad (2.41)$$

i.e., in this case, the transition energy can be computed as the difference between the Kohn-Sham eigenvalues.

It is important to note that this result is valid only if the level is flat, since if we have more than one k point Eq. 2.41 becomes

$$\Delta E_{trans} = \frac{1}{\Omega_{1BZ}} \int_{1BZ} d^3k (\varepsilon_\beta(\mathbf{k}) - \varepsilon_\alpha(\mathbf{k})), \quad (2.42)$$

where Ω_{1BZ} is the volume of the first Brillouin zone. If ε_α and ε_β are constant with respect to \mathbf{k} , *i.e.*, the level is flat, it is possible to remove the eigenvalues from the integration to obtain

$$\Delta E_{trans} = \frac{\varepsilon_\beta - \varepsilon_\alpha}{\Omega_{1BZ}} \int_{1BZ} d^3k = \varepsilon_\beta - \varepsilon_\alpha. \quad (2.43)$$

Finally, one could be concerned that the number of states to excite scales linearly with the number k points, so the approximation that the change in their occupancy does not change the Kohn-Sham operators would be harnessed. However, the approximation is still valid, since the number of states that remain constant also scales linearly with the number of k points, making the ratio between them constant.

2.6 Vienna Ab-Initio Simulation Package

First-principles simulations in this work are made using the software Vienna Ab-Initio Simulation Package (VASP) (KRESSE; FURTHMÜLLER, 1996a; KRESSE; FURTHMÜLLER, 1996b), within the PAW method (BLÖCHL, 1994; KRESSE; JOUBERT, 1999) to generate the wavefunctions and pseudopotentials.

The software performs integrations in the First Brillouin Zone (1BZ) by means of

sampling,

$$\frac{1}{\Omega_{1BZ}} \int_{1BZ} d^3k f(\mathbf{k}) \approx \sum_{\mathbf{k}} w_{\mathbf{k}} f(\mathbf{k}), \quad (2.44)$$

where Ω_{1BZ} is the volume of the first Brillouin zone and $w_{\mathbf{k}}$ are weights such that

$$\sum_{\mathbf{k}} w_{\mathbf{k}} = 1. \quad (2.45)$$

The plane wave basis set truncation is given by a parameter named ENCUT, which corresponds to the kinetic energy in eV of the plane wave. All plane-waves with kinetic energy smaller than ENCUT are included in the basis set.

The functionals employed throughout the work, as well as the chosen convergence parameters, are described for each calculation in its respective ‘‘Computational Details’’ section.

3 Qubits and the Case of the NV^- Center in Diamond

In this chapter, some motivational topics on quantum computing will be presented, and a brief description of its foundations are going to be explored within an example, which is then experimentally tested in an actual quantum processor. The use of NV^- centers in diamond as solid state qubits is explored, and a description of its properties is given. Finally, a simple model of its operation is proposed, in order to illustrate how the quantum properties are accessed and manipulated.

3.1 Quantum bits and quantum gates

One of the most exciting engineering problems of current days is to develop a quantum computer. A quantum computer is a computation system that makes direct use of quantum phenomena, such as entanglement and superposition, to perform operations on data. Their fundamental building blocks are called qubits, in analogy to the bits present in digital computers. One motivation to create a quantum computer is that it would enable us to solve very complex and time-demanding problems in a fast way. This difference is not because quantum computers are going to be faster in processing data (clock speed), on the contrary, thus most probably will not. It is due to the different kind of operations they can do with the data stored in qubits (STRUCK; BURKARD, 2016).

A qubit is a quantum system consisting of two energy levels, labeled $|0\rangle$ and $|1\rangle$. Together, they compose what is commonly called the *computational basis vectors*. From the axioms of Quantum Mechanics, we have that any normalized linear combination with complex coefficients of these states is also valid states of the system, and from the Born rule (BORN, 1954), the square of the magnitude of the coefficient is the probability of a measurement have its respective basis vector as an outcome. These mixed states are called superpositions.

Since the coefficients can be complex numbers, visualizing a qubit requires a unitary sphere on the state space, called the “Bloch Sphere”, depicted on Fig. 3.1. Each point on

the surface of the Bloch Sphere corresponds to the state of a qubit, being $|0\rangle$ on the top of the sphere and $|1\rangle$ at the bottom. When the qubit is in a superposition of the states $|0\rangle$ and $|1\rangle$, its representation will be in some point between these two extrema.

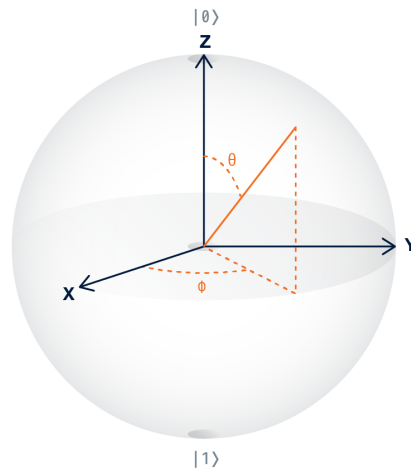


FIGURE 3.1 – Single qubit representation in the Bloch Sphere. The qubit state is represented by the orange line in the picture. The state at the top of the sphere represents $|0\rangle$ and the state at the bottom of the sphere represents $|1\rangle$.

The components of a quantum circuit are the quantum gates, which are basic quantum circuits that operate on a small number of qubits. They are analogous to the classical logic gates of conventional digital circuits. An example of a single qubit gate is the X gate, which is known as “bit flip” or “ X rotation”, since it can be viewed as a π radians rotation around the x axis on the Bloch Sphere. If the original state is $|0\rangle$, it becomes $|1\rangle$, and vice-versa. Analogously to this gate, there are also the Y and Z gates, which correspond to a π radians rotation around the y and z directions, respectively.

Another common single qubit gate is the H gate, known as the Hadamard gate. This gate maps state $|0\rangle$ to state $|+\rangle \equiv (|0\rangle + |1\rangle)/\sqrt{2}$ and state $|1\rangle$ to state $|-\rangle \equiv (|0\rangle - |1\rangle)/\sqrt{2}$, and hence is useful to create superpositions. The states $|+\rangle$ and $|-\rangle$ also form a basis, which is commonly called the “superposition basis”.

Another class of important gates is formed by the two-qubit gates. The most remarkable example is the $CNOT$ gate (Controlled-NOT gate), which flips the target qubit in the computational basis if the control qubit is $|1\rangle$; otherwise, it does nothing. It can be shown that the single qubit gates and the $CNOT$ gate form a universal set of gates, which means that any other gate, acting on any number of qubits, can be build by using only these elements. This is analogous as the NAND gate in classical computing, which is a universal gate, meaning that any other gate can be represented as a combination of NAND gates.

Finally, it is important to mention the *ancilla* qubits, which are quantum registers whose quantum states are known *a priori*. Since quantum computers are reversible computation machines, one cannot deterministically put qubits in a specific prescribed state unless one is given access to qubits whose original state is known in advance. For this reason, algorithms normally use *ancillae* qubits, whose values are independent on the input.

3.2 Quantum algorithms and Quantum speedup

Quantum circuits, which are based on quantum gates, are designed to implement quantum algorithms, some of which have no classical counterpart. By making direct use of superposition and entanglement properties, some algorithms are able to solve problems in a much more efficient way than in classical computing and hence being of particular interest.

Some of the most famous algorithms are:

- **Grover's algorithm**, for unstructured search;
- **Quantum Fourier Transform**, analogous to the Discrete Fourier Transform;
- **Quantum Phase Estimation**, which can be used to determine the eigenvalues of a given matrix;
- **HHL algorithm**, for solving linear systems of equations;
- **Shor's algorithm**, for factoring numbers.

All the listed algorithms present a significant improvement in its complexity over the known classical solutions. For example, the HHL algorithm is able to solve sparse linear system of equations in time $O(\kappa^2 s^2 \log(N), /\varepsilon^3)$ while the classical solution takes $O(\kappa s N \log(1/\varepsilon))$, where N is the number of variables, κ is the conditioning factor, s is the sparseness and ε is the error.

The most important aspect of quantum speedup is that it makes it possible to solve problems that would be impractical otherwise. One outstanding example is Shor's algorithm, which would make it possible to break cryptography. For example, considering that a quantum computer would operate at 1Mhz and that current cryptography uses numbers of about 1000 bits of length, the quantum computer would break the cryptography in about one day, while the best known classical algorithm would take approximately one hundred years (HAMDI *et al.*, 2014).

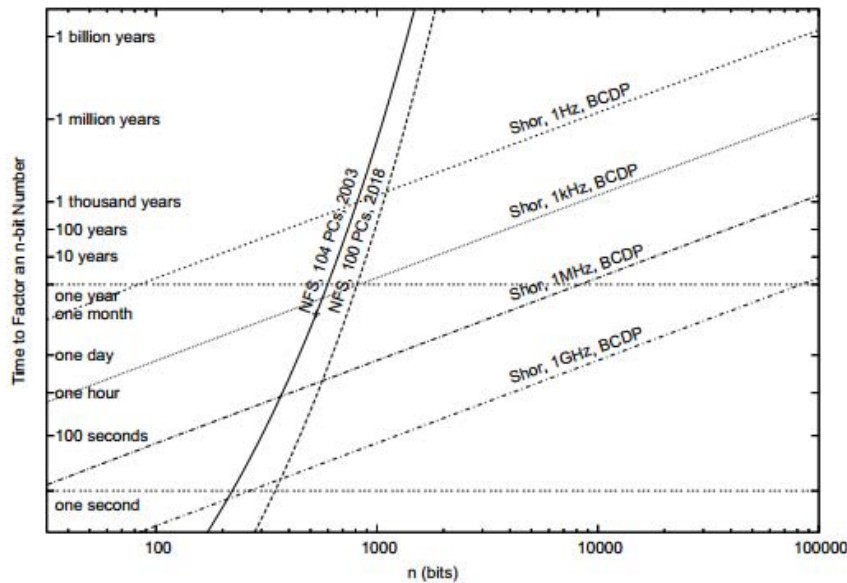


FIGURE 3.2 – Scaling of the general number field sieve (GNFS) on classical computers and Shor’s algorithm using BCDP modular exponentiation on a quantum computer, with various clock rates. The steep curves are for GNFS on a set of classical computers. The left curve is extrapolated performance based on a previous world record, factoring a 530-bit number in one month, established using 104 PCs and workstations made in 2003. The right curve is speculative performance using 1,000 times as much computing power. This could be 100,000 PCs in 2003, or, based on Moore’s law, 100 PCs in 2018. Reproduced from (HAMDI *et al.*, 2014)

3.3 IBM Quantum Experience

Despite the fact that quantum computers are still only available in laboratories and inaccessible for most people, there is one exception: one can program an actual quantum processor and run one’s own quantum software through a program called IBM Quantum Experience. This program’s goal is to allow the users to learn about quantum computing and to compose their own experiments, running them in simulation, and executing them on the world’s first fully-controllable quantum processor through the IBM Cloud.

The IBM Quantum Experience consists of:

- a set of tutorials that leads the reader from the basics of simple single-qubit experiments to more complicated multi-qubit experiments, and then toward more advanced ideas in the area of quantum algorithms and quantum error correction;
- the Quantum Composer, which is a graphical user interface where the user can create his own quantum circuits (which they call quantum scores, in analogy to music scores);
- a simulator that can test the quantum scores;

- access to an actual quantum processor running in an IBM Quantum Computing lab, where the quantum scores will be executed; and
- a quantum community where the quantum scores, ideas, and experiences can be shared and discussed.

As a practical example, we perform an experiment with the circuit depicted in Figure 3.3. In the first line, we are measuring the qubit $q[0]$, which should always result in 0. In the second line, we are measuring qubit $q[1]$ after applying an X gate, and hence it should always result in 1. In the third line, we are measuring the action of the Hadamard gate on $|0\rangle$, and hence the result is expected to be 50% 0 and 50% 1. In the fourth line, we are measuring the action of the Hadamard gate on $|1\rangle$, and hence the result is expected to be 50% 0 and 50% 1. Finally, on the fifth line, we are measuring the result of two consecutive Hadamard gates on $|0\rangle$, and hence the result is expected to be always 0. Since all these measurements are independent of each other, the expected final result is 25% 00010, 25% 00110, 25% 01110 and 25% 01010, as can be confirmed by running a simulation of this circuit.

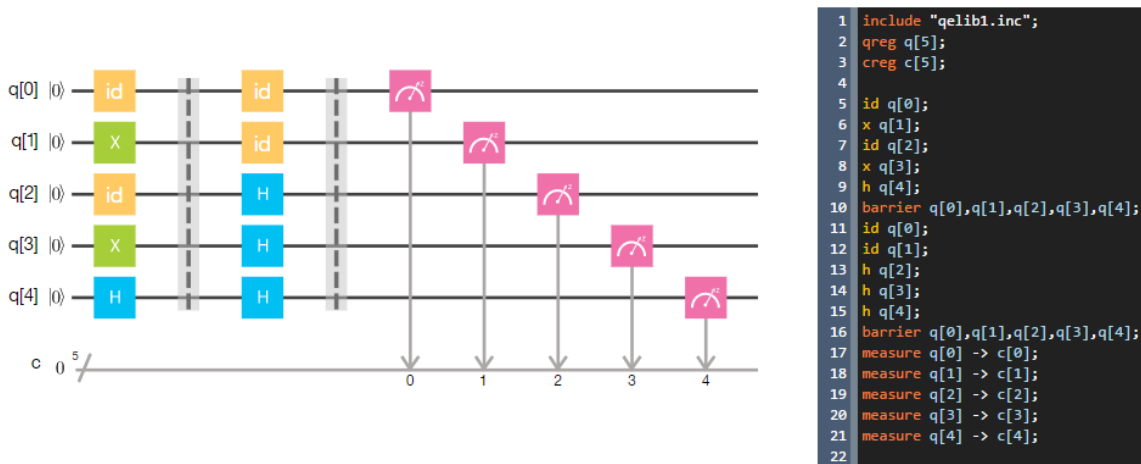


FIGURE 3.3 – Simple quantum circuit used to test the operation of the Hadamard and X gates, and its corresponding Quantum Assembly code. The barriers (vertical gray dashed lines) is added to ensure that the compiler will not perform simplifications, such as $HH = I$; while the idle gates were inserted to ensure the measurements are done at the same time, and hence obtaining a similar level of decoherence in each qubit.

After the simulation, we executed the code on the quantum processor. The results are presented in Fig. 3.4. This experiment is interesting because it highlights the effect of the superposition after the Hadamard gate. Based only on the result of the third and fourth lines, one could naively hypothesize that the Hadamard gates were randomly placing their corresponding qubit on $|0\rangle$ or $|1\rangle$. However, from the fifth line, we see that the result for two consecutive Hadamard gates is always zero, and this rules out the previous hypothesis since under it the result was supposed to be 50% 0 and 50% 1.

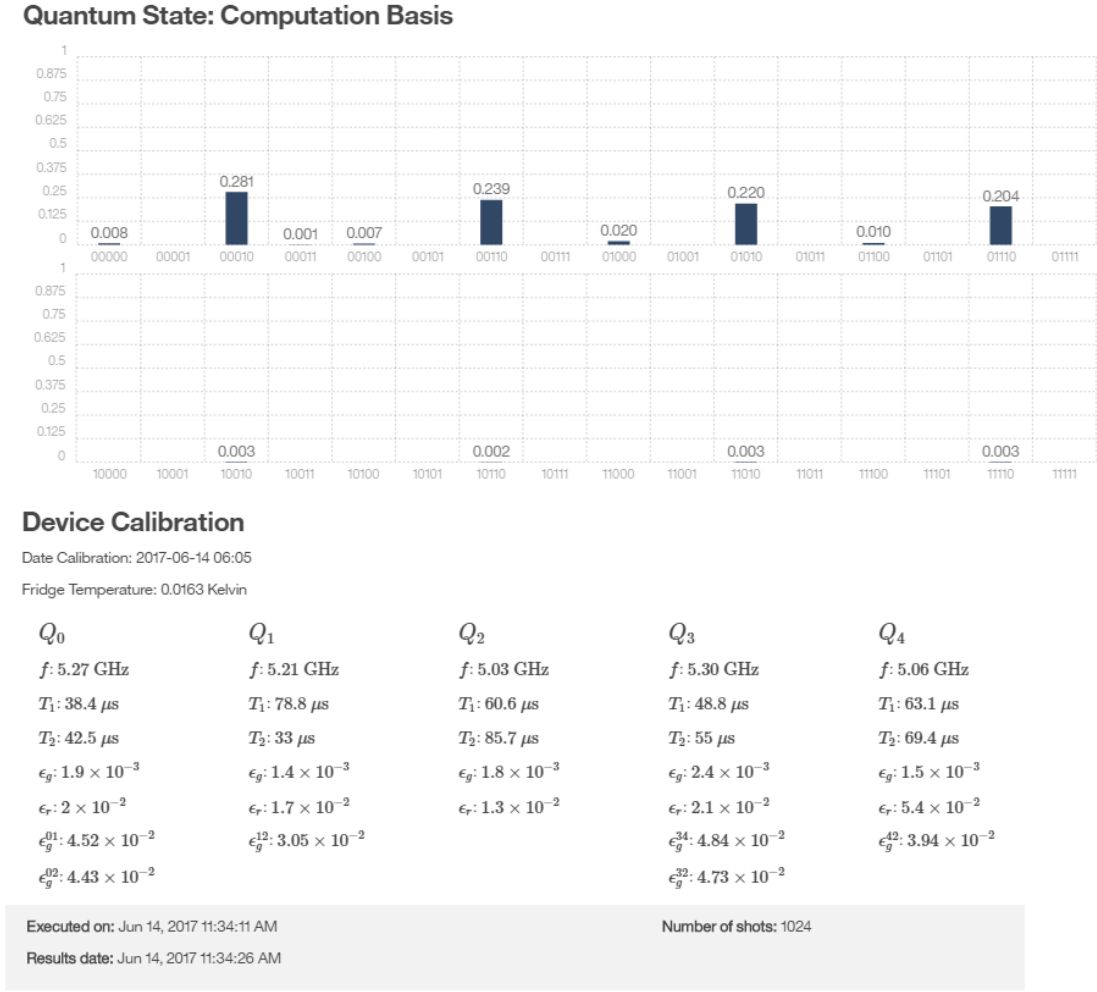


FIGURE 3.4 – Results of 1024 runs of the quantum circuit in Fig. 3.3 on the quantum processor. We note a small percentage of spurious results due to noise and decoherence.

3.4 The NV⁻ Center in Diamond

A major challenge in creating a quantum computer is to find a quantum system that could be used to implement the qubits, which are the building block of quantum computers, in analogy to bits. Most systems interact strongly with their surroundings, causing decoherence and consequently loss of information. In this scenario, deep centers have a prominent position. They are point defects in a semiconductor or insulating crystal that bind electrons to a localized region of space. Consequently, most characteristics of their electronic states resemble the ones of single atoms or molecules. Additionally, deep centers have a fundamental advantage, since they are fixed in space by the surrounding crystal, in contrast to other proposals that require additional systems to accomplish this, as the magneto-optical traps for ultracold atoms.

A deep center in diamond, known as negatively charged nitrogen-vacancy center (NV⁻

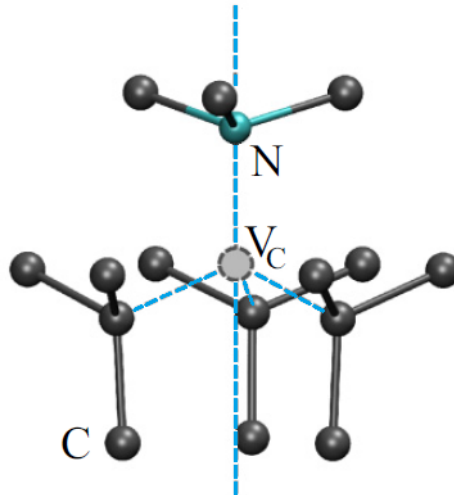


FIGURE 3.5 – NV center in diamond. The vacancy is represented in gray, the nearest-neighbor and next-nearest-neighbor carbon atoms to the vacancy in black and the substitutional nitrogen atom in cyan.

center), has been strongly considered for such applications, since it has many desirable characteristics: its spin can be optically polarized, manipulated with microwaves, optically measured in an on-demand fashion at the single defect level, and also have a huge coherence time, achieving the order of milliseconds (KOEHL *et al.*, 2015).

Point defects are usually stable in different charge configurations, depending on the position of the Fermi level. The NV center has two different charge configurations, NV⁰ and NV⁻, and only the last one has the desired properties (DOHERTY *et al.*, 2013). Fortunately, doping by nitrogen itself can easily place the Fermi level inside the range where the negatively charged defect is stable (WEBER *et al.*, 2010).

The NV center structure consists of a substitutional nitrogen atom adjacent to a carbon vacancy (Fig. 3.5). The defect belongs to the C_{3v} symmetry group, of which the ammonia molecule is also a member. An instructive and useful model is to think of the point defect as an effective molecule. This approach, known as “molecular model for defects” consists in making symmetry adapted linear combinations of the atomic orbitals (SALCs) of the dangling bonds around the vacancy to construct molecular orbitals (MOs) (Fig. 3.6). This approach has the implicit assumption of the electrons bound to the defect being localized in space and not “spilling over” from the vacancy into the rest of the crystal (COULSON; KEARSLEY, 1957; LENEFF; RAND, 1996). The states are commonly labeled using the Mulliken symbols, which in our case are:

- a₁, a₂ where “a” indicates that it is a non-degenerate state without changes of the sign under the C₃ rotations and the subscripts 1 and 2 stand for symmetry and antisymmetry under the σ_v reflections respectively;

- e_x, e_y where “e” indicates that the state is twofold degenerate. These functions do not transform under the C_3 rotations. e_x stands for the wave function that is symmetric under reflection in one vertical plane (xz plane) and e_y for the one that is antisymmetric under reflection in this same plane.

These same labels are used with capital letters when describing states of a multielectronic system.

Since each dangling bond from the three surrounding carbon atoms contributes with one electron, and the overlapping nitrogen orbital has other two electrons, we conclude that the neutral NV center would have five electrons and, consequently, the NV⁻ would have six.

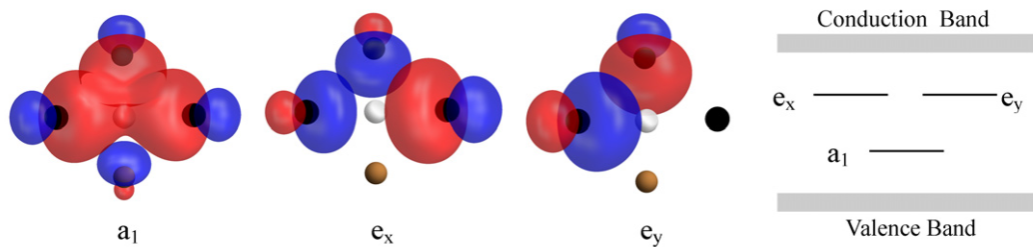


FIGURE 3.6 – Schematics of the three NV center MOs responsible for the center’s observable properties in the vicinity of the vacancy and their energy ordering. The vacancy is represented in white, the nearest-neighbor carbon atoms to the vacancy in black and the substitutional nitrogen atom in brown. Red and blue components represent positive and negative contributions to the MOs, respectively. The band gap induced energy levels are shown at the right, without considering spin-orbit and spin-spin interactions. Reproduced from (DOHERTY *et al.*, 2011).

The state of the art in the theoretical determination of the properties of crystals are the computational methods known as *ab initio* (or first-principles) calculations, in particular, the ones based on Density Functional Theory (DFT). By means of those methods, it is possible to calculate with reasonable precision ($O(0.1 \text{ eV})$) the electronic band structure of systems with translational symmetry, and with some considerations (detailed in the section *Search for other deep centers*), it is possible to determine the energy levels of the point defects. Fig 3.7(a) is the result obtained by Gali *et. al.* (GALI *et al.*, 2008).

We note that the defect has states within the band gap that are spin dependent, a consequence of the fact that this defect breaks the inversion symmetry of the crystal, as explained by Krupin in (KRUPIN, 2004). The electronic occupation for the ground state of the NV⁻ center is shown in Fig. 3.7(a). It can be obtained by filling the lowest energy states with the corresponding spin state (spin up on the left side, spin down on the right side). This leaves us with four spin-up and two spin-down electrons, hence the spins in the ground state do not cancel out and we have a total spin of $S = 1$, *i.e.* the ground

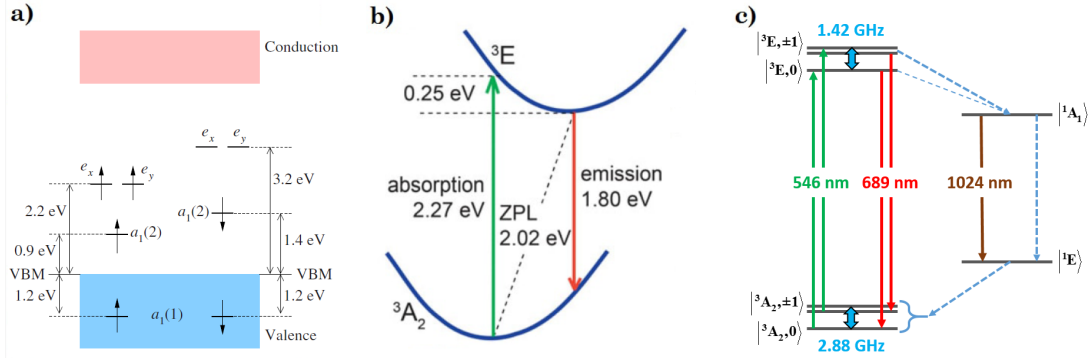


FIGURE 3.7 – (a) Band diagram for the NV⁻ calculated using density functional theory. Reproduced from (GALI *et al.*, 2008). (b) Configuration coordinate diagram. Reproduced from (GORDON *et al.*, 2013). (c) Many-body diagram for the NV⁻ transitions. The primary transition between triplet ground and excited states is predominantly spin conserving. Decay via the intermediate singlets gives rise to spin polarization by preferentially switching spin from $m_s = \pm 1$ to $m_s = 0$.

state is a triplet. This fact is of central importance in the application of the NV⁻ center as a qubit since it is the spin that is used to store the quantum information.

When we apply electromagnetic radiation at 2.27 eV (546 nm, green light) as depicted in Fig 3.7(b), we have resonant excitation to the first excited state. This can be understood in light of Fig 3.7(a) as promoting the spin down electron in the state $a_1(2)$ to one of the excited states e_x or e_y . As we will see soon, this is too simplistic of a way to think about it, since the many-body states are superpositions of the states with well-defined occupancy, but this is a good enough picture in most situations. Note that this is the first possible optical excitation of the system since changes in spin are forbidden at the first order. Another important fact concerning this transition is that we are able to excite the system without exciting any electrons from the valence band, due to the “deepness” of the energy levels within the band gap. If the levels were shallower, it would be possible to excite electrons into the defect levels, what would compromise its operation as a qubit, and the reason for this will become clear in the *Using the qubit* section.

The excited state is also a triplet, but transforms as the E symmetry representation, in contrast with the ground state, which transforms as A_2 . This change in the symmetry of the wave function impacts the geometry of the defect due to the coulombic interaction. The structure then relaxes to the new equilibrium geometry, and since the movement of the ions is orders of magnitude slower than the electronic transition, it is a good approximation to consider that the absorption and emission correspond to vertical transitions (Fig 3.7(b)). The photon emission then occurs in the equilibrium geometry of the excited state, and the difference in energy between the excited state and the ground state in this configuration is 1.80 eV (688 nm, red light). This change in the frequency of absorption/emission is called the Stokes shift. The difference in energy between the excited and

ground states in their respective relaxed geometries is called the Zero Phonon Line (ZPL) and is also indicated in Fig 3.7(b). This large difference in the wavelength enables us to easily separate the photons of the pumping laser from the photons emitted by the center by using a dichroic mirror (which reflects one wavelength and transmits the other), as in confocal microscopy.

It is important to mention here that the DFT approach is complementary to the defect molecular model. These two theoretical methods have their complementary strengths and weaknesses, and only their combined application can give us a good picture of the observed phenomena (DOHERTY *et al.*, 2013).

Thinking of the NV⁻ as a multielectronic system, we can draw the diagram in Fig. 3.7(c), where the states are labeled according to their symmetry and with a left superscript that indicates with a 3 if it is a triplet ($S = 1$) and with a 0 if it is a singlet ($S = 0$). It is well accepted today that we have two triplet states and two intermediate singlet states (DOHERTY *et al.*, 2013). It is possible to relate the many-body states (denoted by capital letters) with the occupancy of the single electron states in Fig. 3.7(a) (denoted by lower case letters) and, in general, the many-body states are superpositions of different occupancies given by Slater determinants (or combination of them, when including spin-orbit interactions). A detailed treatment is given by Leneff and Rand in (LENEFF; RAND, 1996) and by Doherty *et al.* in (DOHERTY *et al.*, 2011).

The optical excitations conserve the spin state, but there is a probability of the states $|^3E, \pm 1\rangle$ decaying non-radiatively to the singlet state $|^1A_1\rangle$, a phenomenon called inter-system crossing (ISC). This happens at an appreciable rate because the energy curve in function of the position of the atoms for the $|^3E, \pm 1\rangle$ state intersects the curve for the $|^1A_1\rangle$ state. Therefore, for some instant during the vibrational relaxation that the ions undergo after the excitement, it is possible for the spin to flip with little or no energy required in the transition (CHOI *et al.*, 2012). It is important to note that this mechanism could also lead to a transition from $|^3E, 0\rangle$ to $|^1A_1\rangle$, but the rate of the ISC is much larger for the $|^3E, \pm 1\rangle$ states, therefore this transition can be neglected. The diagram in Fig. 3.7(c) also shows the non-radiative and infrared competing decay paths between the two singlet states, and the fine splitting in the triplet states, whose difference in energy corresponds to microwave frequencies.

3.5 Using the Qubit

The key feature behind the implementation of qubit using the NV⁻ center is that the spin couples to optical transitions, and we can exploit spin-selective interactions to initialize, manipulate and measure the spin state using optical techniques. In this section,

we will briefly explain how the optical cycle of the NV⁻ center can be exploited in this sense, and introduce a simple model for its dynamics that can reproduce many observed aspects. An example of a real application of the system as a qubit is given in Fig. 3.8 and readers with interest in more details about it should refer to (HIROSE; CAPPELLARO, 2016).

Initialization

The initialization can be achieved by a very straight-forward method: We have an appreciable probability of the system decaying from the $m_s = \pm 1$ to the $m_s = 0$ states through the one-way route of the singlet states, as described above. If we cycle the system for a large enough amount of time ($O(\mu s)$), we should approach 100% of probability of being in the $m_s = 0$ states, at least in principle. The small probabilities of the second-order effects (singlet state decaying to the $m_s = 1$ states, spin flipping in optical transitions, change in the charge state, etc) impose a practical limit to this value.

Manipulation

In order to manipulate the states of the system, the most common procedure is to apply a microwave field resonant with the fine splitting of the ground state. Similarly to the Nuclear Magnetic Resonance (NMR) experiments, the state of the system will precess, giving rise to Rabi Oscillations between the states $m_s = \pm 1$ and $m_s = 0$. By controlling the duration of a pulse of this microwave, we can set the spin state in any desired superposition of these states, and in this way, we are able to write the data in the qubit.

Measurement

As mentioned above, the emitted and absorbed light have different frequencies, thus it is easy to separate the light that is coming out of the NV⁻ center. To measure the qubit, we explore the fact that the $m_s = \pm 1$ states will eventually decay to the long-lived singlet states and therefore fluoresces less than the $m_s = 0$ state on average. The strategy is to illuminate the center with the pumping light and count the intensity of light that comes out of it as a function of time. The incidence of the laser also reinitializes the system, hence we have a window of time ($O(100ns)$) when we can measure the difference in the response of the different initial states. Due to this mechanism, the $m_s = \pm 1$ and $m_s = 0$ states are also called the “dark” and “bright” states, respectively.

It is important to note that this method of measurement requires averaging, which can

be done by two means: first, if we have an ensemble of NV⁻ centers; second, if we make several runs at a single center and record the data. This is not ideal for the quantum computing applications, and there are some proposals in order to increase the spin-photon coupling aiming a single-shot readout. A more ambitious goal is to achieve single-shot measurement by detecting a single photon (BARRETT; KOK, 2004).

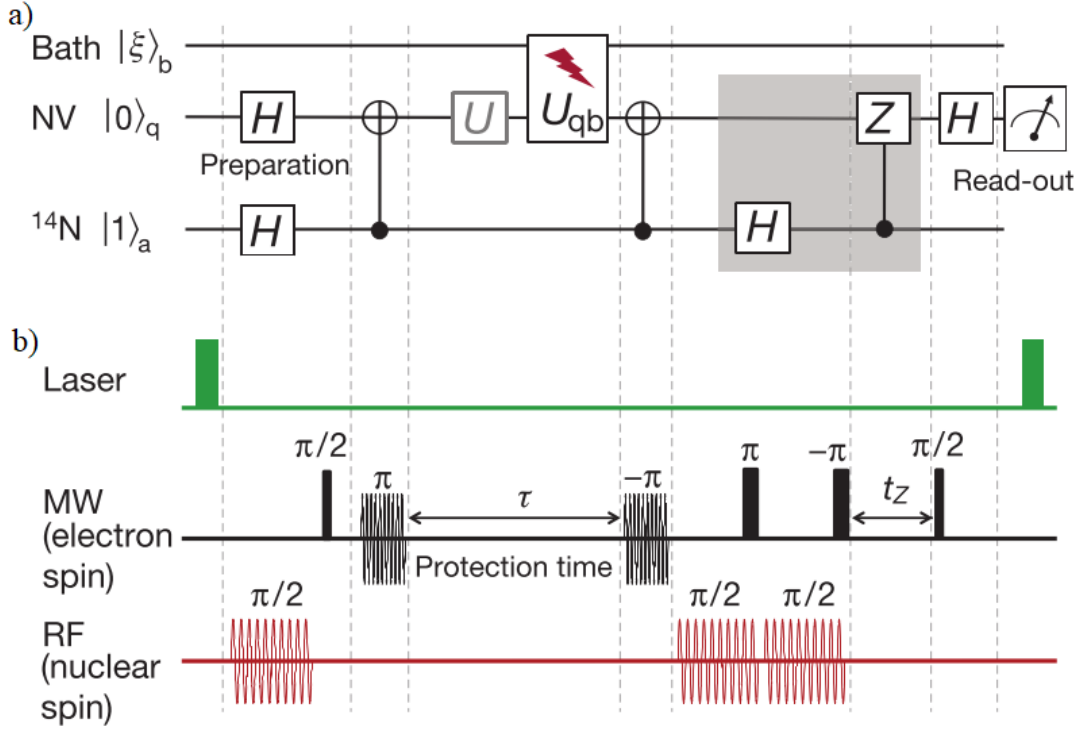


FIGURE 3.8 – (a) An example of a quantum circuit, which implements an algorithm whose function is to decouple the qubit state from a dephasing bath state, and (b) its experimental implementation using an NV⁻ center. In this example, ^{14}N nuclear spin is used as an ancilla (‘a’), and the electron spin of the NV center (‘q’) is subjected to noise (lightning bolt) due to the spin bath (‘b’) of the ^{13}C of the bulk diamond and possibly subjected to the action of unitary gates U . The entangling gates, represented in (a) by the circle with a plus sign inside and a vertical extension, are controlled-NOT gates. The shaded region is a coherent feedback gate implemented by a controlled Pauli-Z gate (‘Z’). Hadamard gates (‘H’) prepare and read out a superposition state of the qubit, $|\phi\rangle_q = (|0\rangle + |1\rangle)/\sqrt{2}$. Figure adapted from (HIROSE; CAPPELLARO, 2016).

Model for the spin dynamics

In order to clarify and illustrate the concepts listed above, a toy model will be developed here.

One of the most simple systems that could be used to study optically excited electronic transitions is the so-called two-level atom. The approximations are that the optical radiation field is nearly monochromatic and that it coincides with one of the transition

frequencies in the atom under consideration. Conceptually, the two-level atom is the same kind of system of a spin-one-half particle in a magnetic field, and hence the spin vector formalism of Bloch, developed for magnetic resonance, is immediately applicable to optical resonance problems (BLOCH, 1946).

In order to facilitate the application of the analogy between these two systems, the pseudospin vector is defined. Its components are related to the atom's dipole moment and inversion, and their time evolutions are determined by a set of equations called the optical Bloch equations, which can be derived by applying the time-dependent Schrödinger's equation (HAGELSTEIN *et al.*, 2004; ALLEN; EBERLY, 2012).

Solving the optical Bloch equations can easily become a difficult task. However, when the properties of interest are only related to incoherent effects, the system can be analyzed very straightforwardly using probabilistic rate equations (ALLEN; EBERLY, 2012), which are a set of differential equations over time of the probabilities that the system occupies each of the different states. Fortunately, many important phenomena are well described under these considerations. For example, Einstein's derivation of Planck's radiation law and his prediction of the phenomenon of stimulated emission was based on rate equations (EINSTEIN, 1917). Lamb has demonstrated that for a laser well above threshold a rate equation approach leads to results in close agreement with those of a much more sophisticated theory (LAMB, 1964). In a more recent work, Casperson compared rate equations in high-gain lasers with more rigorous semiclassical models, and also developed higher-order rate-equation approximations, which can yield much better accuracy with little added complexity (CASPERSON, 1997).

As shown in (ALLEN; EBERLY, 2012), the rate equations are a quasi-steady-state limit of the optical Bloch equations, when the dipole moment homogeneous decay time is the

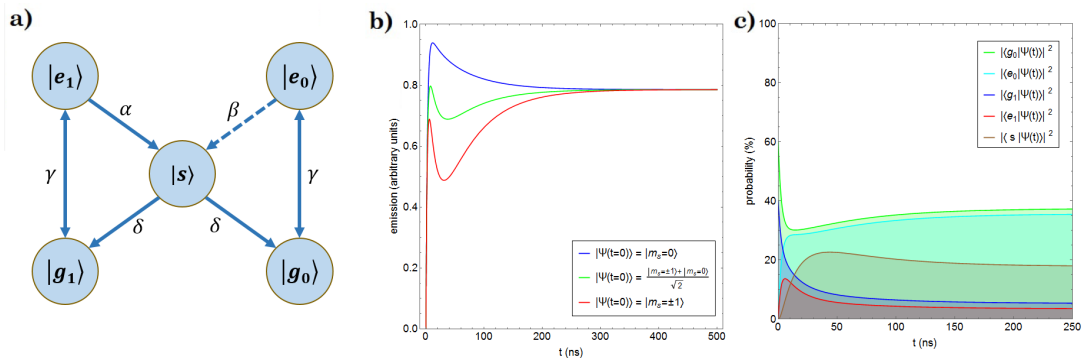


FIGURE 3.9 – (a) 5-level model graph detailing the allowed transitions as well as their rate. (b) Simulation of the time-resolved emission for an ensemble whose centers were previously initialized and manipulated to a specific initial state. (c) Temporal evolution of the probability of being in each one of the states to a center who was previously initialized and manipulated to a superposition state with 40% probability of being in the dark state ($|g_1\rangle$) and 60% probability of being in the bright state ($|g_0\rangle$).

shortest of all the incoherent relaxation rates. Following (ALLEN; EBERLY, 2012), for an ensemble of the two-level system on resonance, the rate equations become

$$\begin{aligned}\dot{N}_2 &= -R(N_2 - N_1) - \frac{N_2}{T_1} \\ \dot{N}_1 &= +R(N_2 - N_1) + \frac{N_2}{T_1}\end{aligned}\quad (3.1)$$

where R expresses the rate of stimulated emission and absorption due to the applied field, N_1 and N_2 are the level population densities and T_1 is the spontaneous decay time. The equations have a very straightforward qualitative interpretation. The first one says that the upper-level population changes for three reasons, at three different rates: at the rate $-RN_2$ because of induced emission, at the rate $+RN_1$ because of absorption of radiation by lower level atoms, and at the rate $-N_2/T_1$ by the natural decay independent of the inducing field. For the second equation, the term $+N_2/T_1$ represents atoms being added to the first-level population because of decay from the first level.

Thus, by the same logic, we can model this system as a series of simultaneous first-order processes. This leads us to a system of coupled first-order differential equations, and if we divide by the total number of centers in the ensemble, we can give a probabilistic interpretation to it. We can, therefore, model it as a Markov chain, since the transition depends only on the present state of the NV⁻ center, and not in the previous transitions.

Based on Fig 3.7(c), we can draw the graph presented in Fig. 3.9(a), where the two singlet states were condensed into one state, labeled $|s\rangle$, and the $|^3A_2, 0\rangle$, $|^3A_2, \pm 1\rangle$, $|^3E, 0\rangle$, $|^3E, \pm 1\rangle$ were labeled $|g_0\rangle$, $|g_1\rangle$, $|e_0\rangle$, $|e_1\rangle$, for convenience in the notation, and we also condensed the degenerate $m_s = \pm 1$ states. Here, s stands for singlet, g for ground state and e for excited state. Note that we included the transmission rate for the $|^3E, 0\rangle$ to $|^1A_1\rangle$, represented by a dashed line to emphasize that it is small.

Some simplifying assumptions about the rates were made: First, we assume that the transition rates from the excited states to the ground state are equal, what is not generally true, especially in this case where they have different resonant frequencies and the intensity of light in each of them is probably very different. Second, we assumed that the transition rates from the excited states to the ground states are equal to the transition rates from the ground states to the excited states, and in general this is not the case since the emission have two different contributions, one from the spontaneous and the other from the stimulated process. Third, we neglected the imperfection of the spin selection rules in the optical excitation and relied only on the more pronounced effect of the $|^3E, 0\rangle$ state decaying to $|^1A_1\rangle$ to model the effects of the undesirable spin flips. Fourth, we assumed that the rates of decaying from the singlet state are equal for both spin states. This might seem like a bad approximation, but in fact, it is not and is in agreement with

the findings of Robledo *et.al.* (ROBLEDO *et al.*, 2011).

Many authors explain the dynamics of the NV⁻ center by admitting that the transition from $|s\rangle$ to $|g_1\rangle$ is small, but as we will see, only the fact that the probability of decaying to $|^1A_1\rangle$ is smaller for $|^3E, 0\rangle$ than for $|^3E, \pm 1\rangle$ is enough to polarize the spin to $m_s = 0$.

The system of differential equations that describes our system is:

$$\begin{aligned}
 \dot{N}_{|g_0\rangle} &= -\gamma N_{|g_0\rangle} + \gamma N_{|e_0\rangle} + \delta N_{|s\rangle} \\
 \dot{N}_{|g_1\rangle} &= -\gamma N_{|g_1\rangle} + \gamma N_{|e_1\rangle} + \delta N_{|s\rangle} \\
 \dot{N}_{|e_0\rangle} &= \gamma N_{|g_0\rangle} - (\gamma + \beta) N_{|e_0\rangle} \\
 \dot{N}_{|e_1\rangle} &= \gamma N_{|g_1\rangle} - (\gamma + \alpha) N_{|e_1\rangle} \\
 \dot{N}_{|s\rangle} &= \alpha N_{|e_1\rangle} + \beta N_{|e_0\rangle} - 2\delta N_{|s\rangle}
 \end{aligned} \tag{3.2}$$

where $N_{|x\rangle}$ stands for the number of centers in state $|x\rangle$. If we divide all the equations of our system by the total number of centers N , we will have the same equations with the replacements:

$$\begin{aligned}
 \frac{\dot{N}_{|x\rangle}}{N} &= \dot{P}_{|x\rangle} \\
 \frac{\dot{N}_{|x\rangle}}{N} &= \dot{P}_{|x\rangle}
 \end{aligned} \tag{3.3}$$

where $P_{|x\rangle}$ stands for the probability of a center be in state $|x\rangle$.

In order to construct matrices and vectors to describe our system, we will ordinate the basis of our state space as

$$\{|g_1\rangle, |e_1\rangle, |g_0\rangle, |e_0\rangle, |s\rangle\}. \tag{3.4}$$

Our transition rate matrix Q is

$$Q = \begin{pmatrix} -\gamma & \gamma & 0 & 0 & \delta \\ \gamma & -(\gamma + \alpha) & 0 & 0 & 0 \\ 0 & 0 & -\gamma & \gamma & \delta \\ 0 & 0 & \gamma & -(\gamma + \beta) & 0 \\ 0 & \alpha & 0 & \beta & -2\delta \end{pmatrix}, \tag{3.5}$$

and the vector of probabilities is given by

$$P(t) = \begin{pmatrix} |\langle g_1 | \Psi(t) \rangle|^2 \\ |\langle e_1 | \Psi(t) \rangle|^2 \\ |\langle g_0 | \Psi(t) \rangle|^2 \\ |\langle e_0 | \Psi(t) \rangle|^2 \\ |\langle s | \Psi(t) \rangle|^2 \end{pmatrix} \quad (3.6)$$

where $|\Psi(t)\rangle$ is the state of our system at time t . The evolution of the vector of probabilities is simply given by the differential equation:

$$P'(t) = QP(t) \quad (3.7)$$

We can set the derivative of the probabilities to zero and find a steady state given by

$$P_{ss} = \frac{1}{\frac{2}{\gamma} + \frac{2}{\alpha} + \frac{2}{\beta} + \frac{1}{\delta}} \left(\frac{\gamma + \alpha}{\gamma\alpha}, \frac{1}{\alpha}, \frac{\gamma + \beta}{\gamma\beta}, \frac{1}{\beta}, \frac{1}{\delta} \right), \quad (3.8)$$

which is independent of the initial conditions.

Since the measured luminosity is due to the system decaying from one of the states $|e\rangle$ to its respective state $|g\rangle$, we can say that for a large ensemble the emission is proportional to the population of the $|e\rangle$ states. Equivalently, for a single center the average of its emission over many runs is proportional to the probability of being in the states $|e\rangle$. Therefore:

$$I(t) \propto |\langle e_1 | \Psi(t) \rangle|^2 + |\langle e_0 | \Psi(t) \rangle|^2 = P_2(t) + P_4(t). \quad (3.9)$$

The “large ensemble” and “average over many runs” interpretations are dual, and it is easy to relate one to another. In the following discussions we will focus on the former, since we believe it is more intuitive.

This system of coupled first order linear equations have a fifth-order characteristic equation, and our attempts to solve it analytically were unsuccessful. Therefore, we aimed to plug in numerical rates and observe how the system behaves. Some authors have already employed similar models and fitted to the experimental data (ROBLEDO *et al.*, 2011; MANSON *et al.*, 2006), so we can get an insight into how to choose reasonable parameters based on their works. We found that the set of parameters

$$\begin{aligned} \gamma &= 0.2 \text{ ns}^{-1} \\ \alpha &= 0.1 \text{ ns}^{-1} \\ \beta &= 0.01 \text{ ns}^{-1} \\ \delta &= 0.02 \text{ ns}^{-1} \end{aligned} \quad (3.10)$$

reproduces most of the interesting aspects in the dynamics of this system. We can now use our model to predict the behavior of the system under different initial conditions. Fig. 3.9(b) shows the emission for three different initial spin states according to eq. (3.9). From this result, we note that we have the behavior described on the *Measuring* subsection: for a window of time in the order of 100 ns, the luminosity is a crescent function of the probability of the initial state being in the $|g_0\rangle$ state.

Solving the system for a slightly more asymmetric initial condition, we can visualize the time evolution of the number of centers in each state in a less particularized way. Fig. 3.9(c) can be interpreted as the proportion of centers in each state in function of time, starting from 40% in the dark state and 60% in the bright state. The time scale for the optical transitions is lower than the others, and soon the curves for the respective $|e\rangle$ and $|g\rangle$ pairs start to track each other. The effect that follows is that the centers start to accumulate in the long-lived $|s\rangle$ state and the system undergoes to the steady state, which is independent of the initial conditions.

The comparison of our result for the emission rate with the experimental measurements in Fig. 3.10 confirms that the most important qualitative characteristics of the system were preserved, despite all the simplifications.

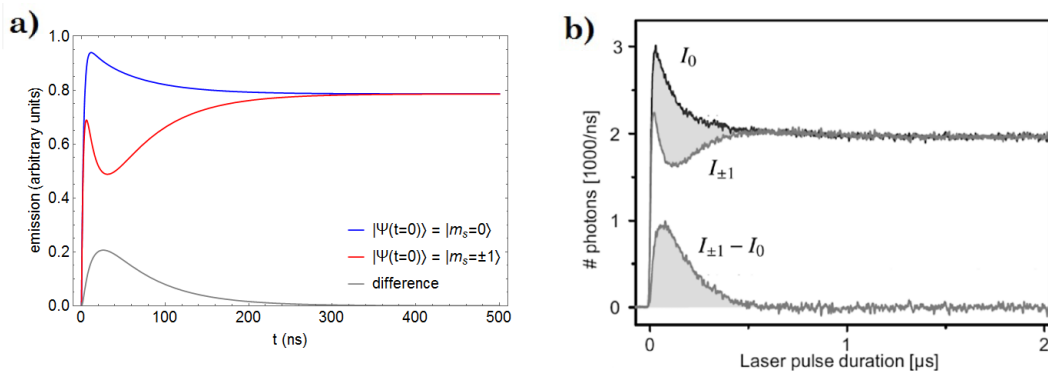


FIGURE 3.10 – (a) Simulation of the time-resolved emission for an ensemble whose centers were previously initialized and manipulated to the dark state and to the bright state. (b) Experimental result measured using confocal microscopy. Reproduced from (DOHERTY *et al.*, 2013).

4 The DFT-1/2 Local Correction to Defect Levels

In this chapter, an extension of the method DFT-1/2 for correcting the defect levels within the band gap is proposed. The method is then exemplified and benchmarked by its application on the NV^- center in diamond, whose transition energies have already been determined, both theoretically and experimentally. Results for the application to wurtzite gallium nitride (w-GaN) are presented. Finally, some limits of validity of this new approach, more specifically in what concerns substitutional transition-metals, is discussed.

4.1 The Local Correction

The most important tools to support the search for suitable deep centers for quantum computing applications are the *ab initio* computational techniques based on DFT since they allow us to determine macroscopic properties based only on the system's atomic composition and approximate geometry. Many attempts have been made to find such defects to find such kind of defects in several semiconductors, as in some silicon-carbide polytypes, (KOEHL *et al.*, 2015; WEBER *et al.*, 2010) wurtzite aluminum nitride (TU *et al.*, 2013) and zinc-blende gallium nitride. (WANG *et al.*, 2012)

Two major concerns can make first-principle calculations of defects a difficult task. First, the usually employed periodic boundary conditions to study solids require a large supercell to minimize the interaction between the defect and its images. Second, the Kohn-Sham band gap is underestimated when compared to experiments, (SHAM; SCHLÜTER, 1985; PERDEW; LEVY, 1983) which also impairs reliable calculations of defect levels above the valence band. (RINKE *et al.*, 2009) The methods which correct Kohn-Sham eigenvalues, such as hybrid functionals (HEYD *et al.*, 2003; HEYD *et al.*, 2006) and the *GW* approach, (HYBERTSEN; LOUIE, 1985) usually raise the computational cost. (PELA *et al.*, 2015) The DFT-1/2 method is a good alternative due to its nice accuracy and low computational cost.

There are several methods to correct the band-gap predictions of DFT. The most

commonly used are the GW (HYBERTSEN; LOUIE, 1985) and HSE. (HEYD *et al.*, 2003; HEYD *et al.*, 2006) The problem is that those methods, especially GW, sharply raise the computational cost. This imposes a practical limit in the cell size, establishing a trade-off between the time required to perform the calculation and the proximity of two defects. In this work, we extend the GGA-1/2 method, which is a generalization of the LDA-1/2 for GGA pseudopotentials. The method has been chosen by its low-cost characteristics, high accuracy in its predictions and for being entirely theoretical, not semi-empirical.

LDA-1/2 and GGA-1/2 have already been successfully used to study point defects (MATUSALEM *et al.*, 2013; MATUSALEM *et al.*, 2014) by applying a formalism developed by Rinke *et al.* (RINKE *et al.*, 2009) In these cases, the interest was to study the defect formation and transition energies, both quantities related to the electronic ground state in several charge states, such that what was changing was the number of electrons bound to the defect as a function of the Fermi level position. In the present case, the charge of the defect is always the same and our interest is to study the energies associated with the optical excitation of an electron between intra-defect energy levels.

The DFT-1/2 method generalizes the Slater's transition state technique for solids, introducing approximate quasi-particle corrections which lead to accurate band gap calculations. The details of the method are given in Refs. (FERREIRA *et al.*, 2008; FERREIRA *et al.*, 2011). The approach relies on the Janak's theorem (JANAK, 1978) and on the approximately linear dependence of the Kohn-Sham eigenvalues with its own occupation. It is possible to use these two facts to show that, in the case of atoms and molecules, the value of the highest occupied eigenvalue with half-ionization is the system ionization energy with a remarkable agreement with experimental data.(SLATER; JOHNSON, 1972)

In semiconductors and insulators, the quasi-particle band gap is defined as the energy difference between the ionization energy and the electronic affinity. Thus, this scheme allows us to compute the band gap as the difference between the Kohn-Sham eigenvalues, by introducing a half-hole on the VBM and a half-electron on the CBM.

Since Bloch states are delocalized, they do not accurately describe neither the hole on the valence band nor the electron on the conduction band. (FERREIRA *et al.*, 2011) Therefore, instead of changing the occupations of the levels, this contribution in energy is added to the potential of the atoms itself. It is assumed that this potential has the same format of the atomic self-energy potential V_S , which can be simply computed as the difference between the neutral atomic potential and the half-ionized atomic potential. (FERREIRA *et al.*, 2008) Considering that the localized hole state will be close to the VBM and the localized electron state will be close to the CBM, we must find which atomic orbitals contribute to each of these levels and in what proportion (the orbital *character* of the levels). This is quantified by the projection of these Kohn-Sham orbitals onto the atomic orbitals. A schematic representation of this scenario is given in Fig. 4.1(a).

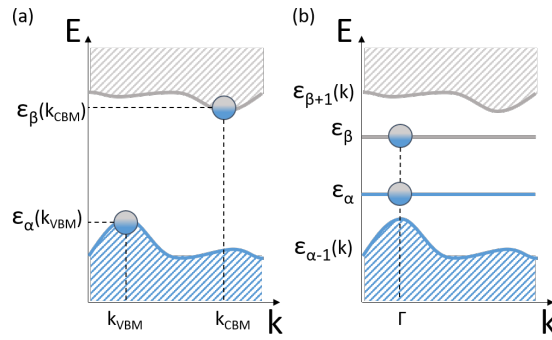


FIGURE 4.1 – (a) Schematic representation of a Kohn-Sham band structure with the Valence Band Maximum and Conduction Band Minimum with half-occupation, as considered on the DFT-1/2 method; and (b) Extension of the DFT-1/2 scheme for defect levels within the band gap.

In what follows, we describe an extension of the method for defect levels, which resembles in many aspects the scheme for the bulk (Fig. 4.1(b)). Due to the increased complexity of the orbital character of the levels, a more precise notation is necessary. Indeed, this is also a formalization of some ideas that already have been introduced in recent publications. (FREITAS *et al.*, 2016b; FREITAS *et al.*, 2016a; ATAIDE *et al.*, 2017)

We must add the potential that corresponds to the removal of half-electron from the occupied level (labeled α). In the usual and simple cases for the bulk, the Kohn-Sham state $\psi_{\alpha}(k_{\text{VBM}})$ is composed only of the valence level p orbital of the ion. However, in the case of the defect, we can have a set of atoms contributing to this level, in which case we must remove a smaller fraction of electron from each of them, proportionally to their contribution. Hence, for each atomic orbital ϕ of each atom X , we subtract a fraction $\xi_{X,\phi}$ of an electron given by

$$\xi_{X\phi} = \text{char}_{X\phi} [\psi_{\alpha}(\Gamma)] \times \frac{1}{2}, \quad (4.1)$$

where $\text{char}_{X\phi}[\psi(k)]$ corresponds to the proportion of the atomic orbital ϕ of atom X to the orbital character of the Kohn-Sham state ψ at point k . Similarly, we must add the potential that corresponds to the addition of half-electron to the unoccupied level (labeled β). The fraction $\zeta_{X\phi}$ to be added to the orbital ϕ of atom X is given by:

$$\zeta_{X\phi} = \text{char}_{X\phi} [\psi_{\beta}(\Gamma)] \times \frac{1}{2}. \quad (4.2)$$

The projection on atomic orbitals is usually a standard output of DFT codes and is computed as the projection of the wave functions onto spherical harmonics within spheres of an atomic species-dependent radius around each ion. Considering the fact that some small contributions of atoms far from the defect are going to be neglected, it is important

to normalize the orbital characters of the considered atoms with respect to their sum, ensuring that

$$\sum_{X\phi} \xi_{X\phi} = \sum_{X\phi} \zeta_{X\phi} = \frac{1}{2}. \quad (4.3)$$

The self-energy potentials are considered spherically symmetric, so the dependence on r will be omitted on our notation. We compute the components $V_S^{X\phi}$ of the self-energy potential V_S as

$$V_{S,\alpha}^{X\phi} = V_X(f_0) - V_X(f_0 - \xi_{X\phi}) \quad (4.4)$$

$$V_{S,\beta}^{X\phi} = -[V_X(f_0) - V_X(f_0 - \zeta_{X\phi})], \quad (4.5)$$

where f_0 is the occupation of the orbital ϕ of atom X on the ground state, and $V_X(f)$ is the potential of atom X with occupation f . Adding the components, we find

$$V_S^{X\phi} = V_X(f_0 - \zeta_{X\phi}) - V_X(f_0 - \xi_{X\phi}). \quad (4.6)$$

Before adding the potentials to the Kohn-Sham potential, we must multiply them by a trimming function $\Theta_{X\phi}(r)$ to avoid the divergence that would arise from the sum of the $1/r$ coulombic tails of these potentials. (FERREIRA *et al.*, 2008; FERREIRA *et al.*, 2011) Θ is a smooth step-like function, defined as

$$\Theta(r) = \begin{cases} \left[1 - \left(\frac{r}{CUT}\right)^8\right]^3 & \text{if } r \leq CUT \\ 0 & \text{if } r > CUT \end{cases} \quad (4.7)$$

which depends on a parameter called CUT . This parameter have to be determined variationally, by extremizing the band gap. (FERREIRA *et al.*, 2008; FERREIRA *et al.*, 2011) Thus, the trimmed potential is

$$\widehat{V}_S^{X\phi} = \Theta_{X\phi} V_S^{X\phi}. \quad (4.8)$$

It is common to have situations in which the CUT depends only on the atom. In these cases, it is useful to define

$$\widehat{V}_S^X = \Theta_X \sum_{\phi} V_S^{X\phi}, \quad (4.9)$$

and then we would have a single correction to the potential per atomic species, with a single value of CUT to be determined variationally.

The most noticeable difference between the usual DFT-1/2 and the procedure here

introduced is that in the latter exactly half electron is transferred between the defect levels, being divided amongst the atoms which contribute to them. In solids, the total number of transferred electrons scales with the number of atoms in the cell, since the corrections are applied as if each atom contributed independently to the composition of the VBM and the CBM.

4.2 Benchmarking with the NV^- Center in Diamond

4.2.1 Computational details

The calculations have been performed within the DFT combined with the Generalized Gradient Approximation of Perdew-Burke-Ernzerhof (GGA-PBE) exchange-correlation potential (PERDEW *et al.*, 1996a) using the Viena Ab-initio Simulation Package (VASP). (KRESSE; FURTHMÜLLER, 1996a; KRESSE; FURTHMÜLLER, 1996b) The electronic wave functions have been expanded using the projected augmented wave (PAW) method. (BLÖCHL, 1994; KRESSE; JOUBERT, 1999)

In order to build a good approximation for the supercell structure, the structure of a single cubic unit cell has been relaxed. The next step is to replicate it side by side to build

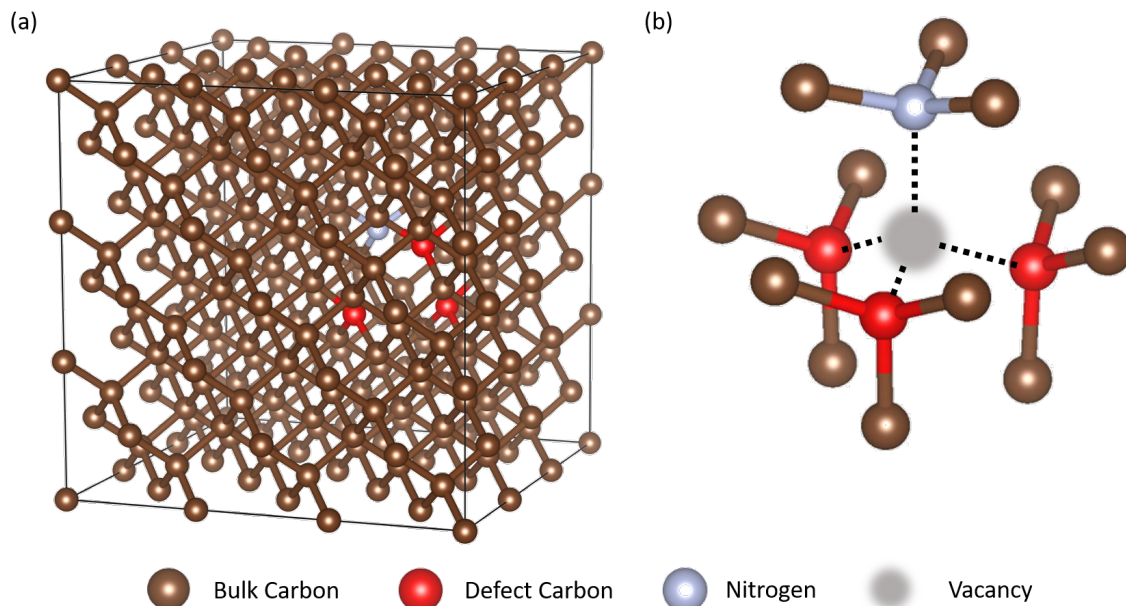


FIGURE 4.2 – (a) 215-atom supercell used to simulate the defect avoiding spurious interactions among images. (b) NV^- center and its surrounding atoms, representing the vacancy as a gray shadow. In both images, Brown, bluish-gray and red circles represent, respectively, the host carbon atoms, the nitrogen atom, and the three carbon atoms neighboring the vacancy. The images have been produced with help of the VESTA software. (MOMMA; IZUMI, 2011)

a 3x3x3 supercell, with a total of 216 atoms, and a new structural relaxation has been carried out. Then, the defect has been created by arbitrarily removing one of the atoms of the supercell and replacing one of the carbon atoms neighboring the resulting vacancy by a nitrogen atom (Fig. 4.2). The number of electrons has been increased by one since we are interested in the negatively charged NV center. As the last step before applying the DFT-1/2 corrections, a spin-polarized structural relaxation has been performed for both the electronic ground state and first excited state by setting the corresponding energy levels occupations, to obtain and store the respective resulting atomic positions. It is noteworthy that, according to Fig. 3.7(a), the first excited state corresponds to promote the highest occupied spin-down state ($2a_{1\downarrow}$) to the lowest unoccupied spin-down states ($e_{x\downarrow}$ and $e_{y\downarrow}$), with half electron in each one of the states, to symmetrize the occupation.

In the geometry optimization of the pure cells, *i.e.* cells that do not include the defect, the volume and the shape of the cell and all the atoms have been allowed to relax until the magnitude of all forces is smaller than 10^{-3} eV/Å. In order to save computational effort and relying on the fact that only the nearest atoms should be affected by the defect, the volume and the shape of the cell have been fixed for the relaxation of the supercells with the defect, and the same stopping criteria as before have been used.

Following the Monkhorst-Pack scheme, (MONKHORST; PACK, 1976) the Brillouin zone (BZ) has been sampled by a 19x19x19 grid of k-points for the single cubic cell and by only the gamma point for the supercells. The plane wave basis set has been considered within cutoff energy of 530 eV. The electronic convergence criterion has been that the total (free) energy and the band structure energy change between two steps are both smaller than 10^{-7} eV. In the simulation of the negatively charged defect, a positive uniform background charge has been added. The numeric errors of our calculations have been estimated to be smaller than 50 meV.

4.2.2 Procedure

The usual procedure to calculate the optical transition energies of defect levels is to take the difference in total energy between each electronic configuration. Since this concerns excitations, one needs to go beyond the Kohn-Sham scheme, by carrying out *e.g.* HSE calculations, to avoid the usual band gap problem.(RINKE *et al.*, 2009) Hence, one must go beyond standard DFT, as in HSE calculations, in order to obtain a more accurate result for these energies. The inconvenient is the increase in the computational cost. Therefore, it would be of interest to apply the less demanding DFT-1/2 formalism. However, as implemented, this method does not compute a physically meaningful total energy, but the optical transition energies can be accurately obtained as the difference between their corresponding Kohn-Sham eigenvalues, as demonstrated in Section 2.5.

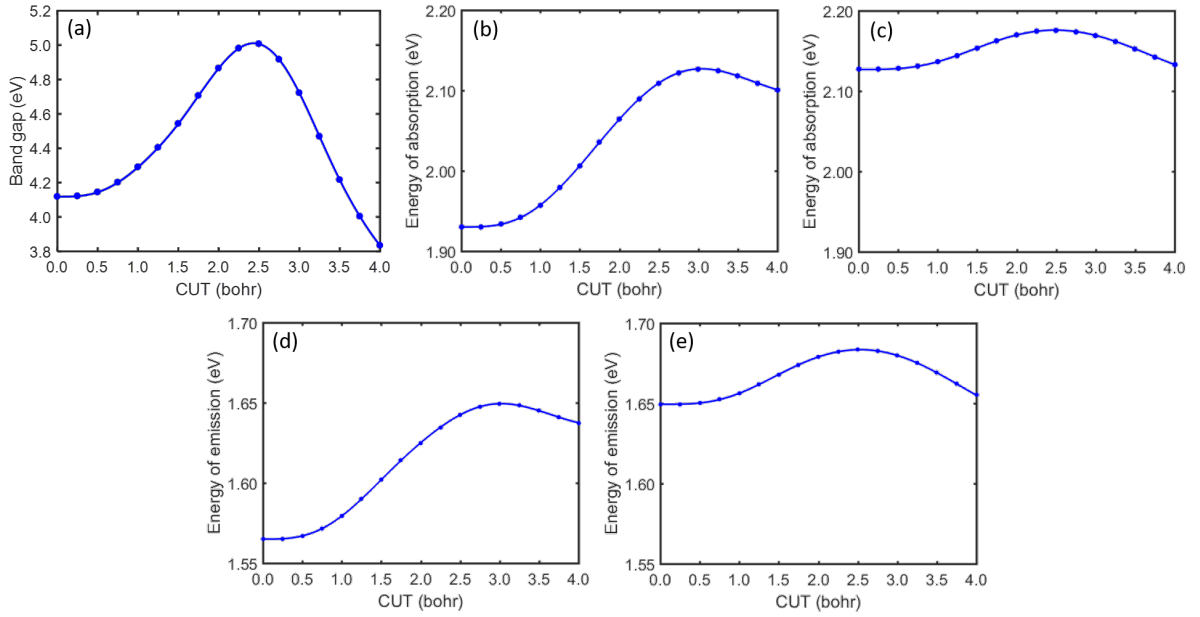


FIGURE 4.3 – CUT determination for the DFT-1/2 corrections. The corrections have been performed sequentially for each geometry, in the following order: C_{Bulk} , N, C_{Defect} . (a) Band gap of pure diamond as a function of the CUT for the 0.25 electron removal from the C_{Bulk} atoms' $2p$ orbital; (b) Transition energy on the ground state's geometry as a function of the CUT of the nitrogen atom, with C_{Bulk} corrected; (c) Transition energy on the ground state's geometry as a function of the CUT of the C_{Defect} atoms, with C_{Bulk} and N corrected; (d) Transition energy on the excited state's geometry as a function of the CUT of the nitrogen atom, with C_{Bulk} corrected; (e) Transition energy on the excited state's geometry as a function of the CUT of the C_{Defect} atoms, with C_{Bulk} and N corrected.

We must obtain the difference between the state $2a_{1\downarrow}$ and the double-degenerate state e_{\downarrow} in each geometry, according to Fig. 3.7(a). We may write

$$E_{Ab} = \varepsilon(e_{\downarrow}; q_{gnd}) - \varepsilon(2a_{1\downarrow}; q_{gnd}) \quad (4.10)$$

$$E_{Em} = \varepsilon(e_{\downarrow}; q_{exc}) - \varepsilon(2a_{1\downarrow}; q_{exc}), \quad (4.11)$$

where $\varepsilon(\psi; q)$ corresponds to the eigenvalue of the state ψ as a function of the configuration coordinate q , which in the current case correspond to the most stable geometries in each one of the two electronic configurations, as indicated in Fig. 3.7(b). Note that it is only possible to unambiguously define these functions because the position of the eigenvalues is considered independent of the occupation of these levels, as explained in Section 2.5. Otherwise, they would be functions of the occupation as well.

With the relaxed geometries for both the ground and excited states, we first separate the atoms in three types: the carbon atoms of the bulk (C_{Bulk}), which are responsible for the valence and conduction bands, the nitrogen atom, and the carbon atoms which are the carbon vacancy next-neighbors (C_{Defect}), whose dangling bonds contribute to the

TABLE 4.1 – Orbital character of the defect levels and fractions of an electron to be removed from and added to each potential (denoted by ξ and ζ , respectively).

$X\phi$	Ground State				Excited State			
	$2a_{1\downarrow}$	$\xi_{X\phi}$	$e_{x\downarrow}+e_{y\downarrow}$	$\zeta_{X\phi}$	$2a_{1\downarrow}$	$\xi_{X\phi}$	$e_{x\downarrow}+e_{y\downarrow}$	$\zeta_{X\phi}$
C_{2s}	0.6%	0.00	3.1%	0.02	0.6%	0.00	2.2%	0.01
C_{2p}	17.7%	0.09	30.2%	0.15	21.7%	0.11	31.1%	0.16
N_{2s}	4.6%	0.02	0.0%	0.00	4.9%	0.02	0.0%	0.00
N_{2p}	40.7%	0.20	0.3%	0.00	28.1%	0.14	0.3%	0.00

localized defect levels. Since these types contribute differently to the band structure, they must be analyzed separately.

For the C_{Bulk} atoms, the same corrected potential as the one used in the diamond unit cell is applied: due to the perfectly covalent bonds between the carbon atoms, the band gap of diamond is corrected by subtracting one quarter of electron from the $2p$ orbital of the C_{Bulk} atoms, as indicated in Ref. Ferreira *et al.* (2008). The CUT of 2.5 bohr is determined by maximizing the band gap, which gives a gap of 5.01 eV, as shown in Fig. 4.3(a).

To apply the local correction to the defect, the character of the levels involved in the first optical excitation, for both geometries, is determined by using the band character obtained by standard PBE calculation. Accordingly, the percentage of the character contribution is obtained by considering solely the nitrogen atom and the carbon atoms that are the vacancy next-neighbors (C_{Defect}). Table 4.1 presents the orbital character of the defect levels.

For each orbital, in each geometry, the potential of half electron, weighted by the character of the $2a_{1\downarrow}$ level, must be removed, while the potential of half electron, weighted by the character of the two states e_{\downarrow} , must be added. These results are also displayed in Table 4.1. The CUT parameters for these corrections are determined by maximizing the difference between the levels e_{\downarrow} and $2a_{1\downarrow}$, and we obtain the same values for the excited and ground states, which are CUT=2.50 bohr for C_{Defect} and CUT=3.00 bohr for N. The curves obtained in this optimization procedure are displayed in Figs. 4.3 (b, c, d, and e).

The maximum values obtained on Figs. 4.3 (c and e) correspond, respectively, to the corrected absorption and emission energies. The values are displayed in Table 4.2, together with other results and experimental data. With their respective corrected potentials, the electronic structure is calculated for each geometry, and the corrected band structures are displayed in Fig. 4.4. The energy differences between the defect levels correspond to the optical transition energies, as indicated by the curved arrows. The similarity of these results with the initial and simple picture of the position of the energy levels (Fig. 3.7(a))

TABLE 4.2 – Vertical absorption (E_{Ab}), vertical emission (E_{Em}), zero-phonon line (E_{ZPL}), Stokes shift (E_S) and anti-Stokes shift (E_{aS}) energies calculated by different methods, compared to the experimental data (all values in eV).

	Method	E_{Ab}	E_{Em}	E_{aS}	E_{ZPL}	E_S
GGA	total energy	1.90	1.55	0.16	1.71	0.19
GGA	eigenvalues	1.86	1.55	0.16*	1.72 [†]	0.15 [‡]
GGA-1/2	eigenvalues	2.18	1.68	0.16*	1.85[†]	0.33[‡]
HSE06 (GALI <i>et al.</i> , 2009)	total energy	2.21	1.74	0.22	1.96	0.26
Exp. (DAVIES; HAMER, 1976)	-/-	2.18	1.76	0.19	1.95	0.24

* Calculated using Eq. 4.12

† Calculated using Eq. 4.13

‡ Calculated using Eq. 4.14

is remarkable. A discussion about Table 4.2 and about the band structures shown in Fig. 4.4 is given in Section 4.2.3.

Besides the vertical transition energies, the ZPL energy is also of experimental interest. We cannot simply use the difference between the Kohn-Sham eigenvalues of two different geometries to calculate it since it would not take into account the energy difference due to the displacement of the ions. Nonetheless, we can indirectly calculate E_{ZPL} . This is possible because the values for the total energy of the two geometries in their electronic ground state are correctly calculated by the standard DFT. Hence, we can obtain the anti-Stokes shift as

$$E_{aS} = E(f_{gnd}, q_{exc}) - E(f_{gnd}, q_{gnd}), \quad (4.12)$$

where $E(f, q)$ is the energy as a function of the electronic configuration f and the geometry q , and use it together with the vertical transitions to determine the remaining desired energies as

$$E_{ZPL} = E_{Em} + E_{aS} \quad (4.13)$$

$$E_S = E_{Abs} - E_{ZPL}, \quad (4.14)$$

as one can readily see from Fig. 3.7(b).

Finally, the steps to be followed to apply the DFT-1/2 method for defect levels, introducing Local Corrections, can be summarized:

1. Perform the structural relaxation of the unit cell;
2. Determine the VBM and CBM orbital characters;
3. Build the supercell and perform a new structural relaxation;
4. Set and build the defect in the supercell, perform the structural relaxation with the electronic ground state occupancy and determine the orbital character of the

- selected defect levels;
5. Perform the structural relaxation with the electronic excited state occupancy and determine the orbital character of the selected defect levels;
 6. Calculate the system total energy in the electronic ground state in the excited state geometry, and determine the anti-Stokes shift (E_{aS}) using Eq. 4.12;
 7. Determine the CUT parameter for the bulk atoms by maximizing the band gap;
 8. Determine the CUT parameter for the defect atoms by maximizing the energy difference between the selected defect levels, and determine the energies of the vertical transitions (E_{Ab} and E_{Em}); and
 9. Determine the remaining energies (E_{ZPL} and E_S) using Eq. 4.13 and Eq. 4.14, respectively.
 10. Optional: Calculate the corrected band structures.

4.2.3 Results and Discussion

The diamond band gap value of 5.01 eV obtained with GGA-1/2 approach shows remarkable improvement over the value of 4.1 eV obtained with standard GGA when compared to the experimental value of 5.47 eV. (WORT; BALMER, 2008) Even though the result has a considerably better agreement with the experimental value, it is still slightly underestimated, not as good as the corrections to other materials. (FERREIRA *et al.*, 2011)

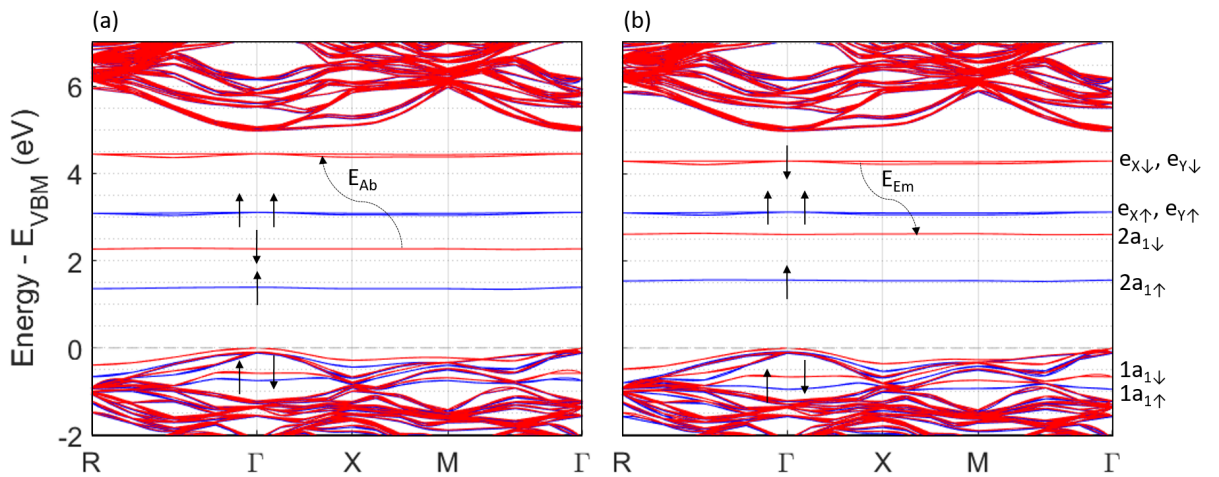


FIGURE 4.4 – Supercell band structures, around the gap region and along some special high symmetry directions in the cubic BZ, for the structural geometries of the NV- center in the (a) ground state and (b) excited state. The blue and red lines represent, respectively, the spin-up and spin-down energy levels. The occupied states related to the defect are indicated by \uparrow and \downarrow arrows. Both results have been obtained with bulk and local corrections. The direct band gap is a consequence of the supercell band folding.

This is due to the fact that the VBM and CBM of diamond's band structure have almost the same orbital character and the usual procedure (FERREIRA *et al.*, 2008; FERREIRA *et al.*, 2011) is not able to appropriately correct the conduction band.

The corrected band structures of Fig. 4.4 present all the expected general features for the NV^- center in diamond: the defect $1a_1$ energy levels are resonant inside the valence band; the relative positions of the spin up and spin down levels are correct; and the first possible valence band excitation is high energetic enough, avoiding an electron transition from the valence band to the defect $2a_{1\downarrow}$ energy levels when the pumping laser is shined.

Although the e_{\downarrow} energy levels appear to be closer to the conduction band than expected, due to the slightly underestimated band gap, the transition energies analysis is not impaired. On the other hand, since the gap underestimation is a diamond particular case, as explained above, the method is expected to display still better performance when applied to other semiconductors, like the III-V ones, in which the application of the DFT-1/2 method presents very accurate results. (FERREIRA *et al.*, 2011)

The usual procedure to obtain the optical transition energies via DFT is to take the difference between the total energy values of the excited and ground states. The correction method proposed here allows these quantities to be extracted directly from the Kohn-Sham eigenvalues. To verify this claim, Table 4.2 presents results obtained with the usual total energy approach and with the eigenvalues approach, without the quasi-particle corrections. Even though these values are not supposed to correspond to the quasi-particle band gap, they should agree with each other, and in fact, they do within a precision of 0.04 eV.

The results obtained when using the DFT-1/2 approximate quasi-particle corrections are in close agreement with the reported HSE results and experimental data. It is observed that, in the GGA-1/2 results, the relative error of the Stokes and anti-Stokes shifts are greater than that of the other energies, as expected, since both shifts values result from the difference between two values very close to each other.

In our development, it has been argued that the standard DFT approach may provide a good estimate of the anti-Stokes shift, and this is supported by the results from Ref. (GALI *et al.*, 2009) that reports both GGA-PBE and HSE calculations of the anti-Stokes shift for a larger supercell (4ax4ax4a) than the one used here, and they indeed shown that GGA slightly outperformed HSE.

4.3 Chromium-Vacancy in w-GaN

4.3.1 Characteristics of the Host

Gallium nitride is a binary III-IV semiconductor with well-established growth techniques. Its most stable phase has the wurtzite crystal structure, and a wide band gap of 3.4 eV, which affords its special properties for applications in Optoelectronics. For example, the first high-brightness blue LED, invented by Shuji Nakamura in 1989, was made of GaN. Producing a bright blue LED was first achieved by Akasaki and Amano (AMANO *et al.*, 1989). They developed a method to produce strongly p-type GaN by electron-beam irradiation of magnesium doped-GaN.

The advances of Nakamura’s work were to create a method to mass-produce the strongly p-type GaN, by doping it with Magnesium via a thermal annealing process, and to identify the passivation of acceptors caused by Hydrogen. The blue LED technology allowed for the production of white LEDs, by partially converting the light to yellow via a phosphor coating, and they went into production in 1993. Due to his contributions, he was rewarded with the 2014 Nobel Prize for Physics, “for the invention of efficient blue light-emitting diodes, which has enabled bright and energy-saving white light sources”, together with Isamu Akasaki and Hiroshi Amano.

Due to its technological relevance, several defects have been studied for GaN, both theoretically and experimentally. However, until recently, the interest was to find shallow donors and acceptors in GaN, and the plausibility of using deep defects as spin qubits was not considered. This scenario might have changed when GaN was identified as a potential host for spin qubits (GORDON *et al.*, 2013), together with several other semiconductors. Since then, there have been studies considering the properties of defects, such as the first-principles study of an Oxygen-Vacancy complex defect in cubic GaN (WANG *et al.*, 2012), and the spectroscopy of isolated defects in several GaN samples grown on sapphire and silicon carbide.

4.3.2 Computational details

As in Section 4.2.1, the calculations have been performed within the DFT combined with the Generalized Gradient Approximation of Perdew-Burke-Ernzerhof (GGA-PBE) exchange-correlation potential (PERDEW *et al.*, 1996a) using the Viena Ab-initio Simulation Package (VASP). (KRESSE; FURTHMÜLLER, 1996a; KRESSE; FURTHMÜLLER, 1996b) The electronic wave functions have been expanded using the projected augmented wave (PAW) method. (BLÖCHL, 1994; KRESSE; JOUBERT, 1999)

In the geometry optimization of the single cell, the volume and shape of the cell and

all the atoms have been allowed to relax until the magnitude of all forces is smaller than 10^{-5} eV/Å. In order to save computational effort and relying on the fact that only the nearest atoms should be affected by the defect, the volume and the shape of the cell have been fixed for the relaxation of the supercells with the defect, and the stopping criteria were changed to 10^{-4} eV/Å.

Following the Monkhorst-Pack scheme, (MONKHORST; PACK, 1976) the Brillouin zone (BZ) has been sampled by a 19x19x19 grid of k-points for the single orthogonal cell and by only the gamma point for the supercells. The plane wave basis set has been considered within cutoff energy of 530 eV. The electronic convergence criterion has been that the total (free) energy and the band structure energy change between two steps are both smaller than 10^{-7} eV. In the simulation of the positively charged defect, a negative uniform background charge has been added.

4.3.3 Simulating the Defect

There are several potential defects that could be studied in GaN. We have decided to study a complex defect composed by a substitutional Chromium atom at a Gallium site and an adjacent Vacancy, which then occupies a Nitrogen site. In this work, we are going to refer to this defect as the “Cr_{Ga}V_N” center.

In order to study defects in w-GaN, we chose to first perform the structural relaxation

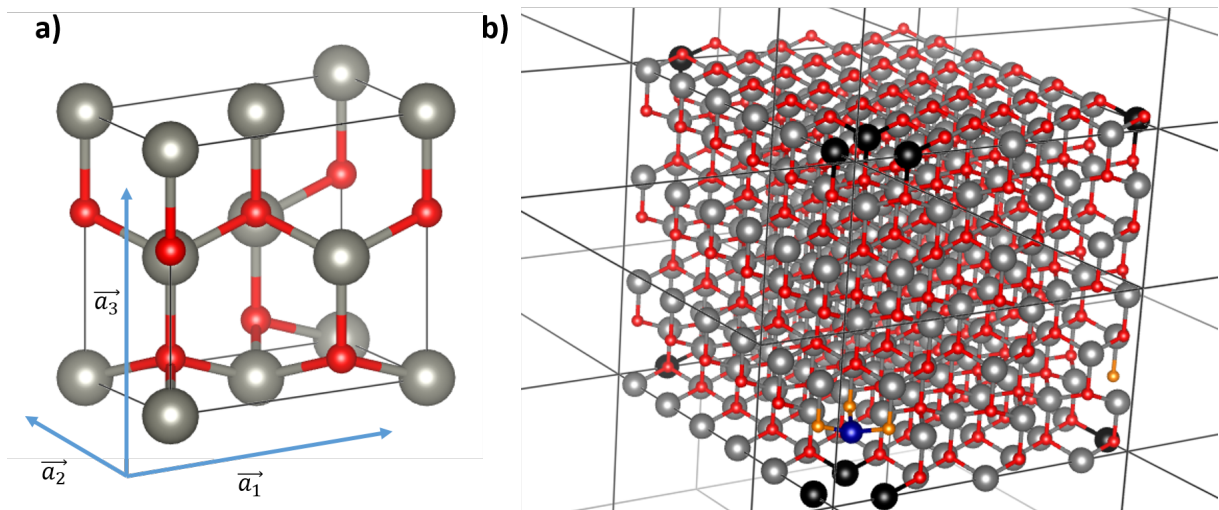


FIGURE 4.5 – (a) Orthogonal cell used to perform the structural relaxation of the w-GaN. (b) 432 atoms supercell used to simulate the defect, avoiding spurious interactions among images. In both images, gray and red spheres represent, respectively, the bulk Gallium and Nitrogen atoms, while the blue, black and orange spheres represent, respectively, the Chromium atom, the three Gallium atoms neighboring the vacancy and the three Nitrogen atoms neighboring the Chromium atom. The images have been produced with help of the VESTA software.(MOMMA; IZUMI, 2011)

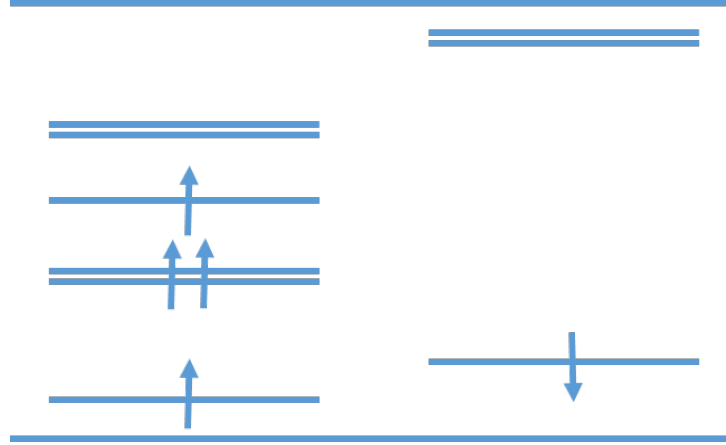


FIGURE 4.6 – Schematic band diagram for the $\text{Cr}_{\text{Ga}}\text{V}_{\text{N}}^+$ center, obtained via first-principles calculations after applying the correction to the bulk atoms.

of a small orthogonal cell, and then replicate it to form a large orthogonal supercell 4.5(a).

The validity of using only the gamma point in the sampling of the first Brillouin zone of the 432 atoms supercell was verified by comparing the calculated total energy with the one of a 4 atoms hexagonal cell fully converged. The ratio between these total energies was of 107.98, while the ratio between the number of atoms is 108. The agreement between these values indicates that a single k-point is enough to sample the supercell reciprocal space.

We then placed the defect of choice in the cell and identified its first neighbors 4.5(b), It is worth noting that in the case of the NV^- center, we only identified the neighbors of the vacancy. However, considering that GaN is a binary compound, it may be necessary to apply different corrections to the neighbors of the substitutional atom as well.

Point defects usually occur in several charge states. The strategy adopted in this work is to first determine charge states that have the desired electronic properties. Verifying whether this state is stable or not and in what conditions is left for a next step, to be done only in case the defect presents the desired properties.

TABLE 4.3 – Transition energy between the levels of interest for different corrections. The bulk corrected potentials were applied to different combinations of atoms, in order to study the effect of considering the neighbor atoms as part of the bulk or not.

Cr	Ga (defect)	N (defect)	Ga (bulk)	N (bulk)	Energy
-	-	-	-	-	0.744
-	-	-	-	X	0.821
-	-	-	X	X	0.819
-	-	X	X	X	0.499
-	X	-	X	X	0.815

Since the ground state of the neutral defect is neither a spin-triplet nor a spin-quadruplet, which have already been experimentally proven to be suitable for spin-qubit operations (WIDMANN *et al.*, 2014), we decided to study the positively charged $\text{Cr}_{\text{Ga}}\text{V}_{\text{N}}$, which will be denoted $\text{Cr}_{\text{Ga}}\text{V}_{\text{N}}^+$. Its level structure and occupation are schematically represented of Fig. 4.6. The highest occupied and lowest unoccupied spin-up levels are the levels of interest and hereafter are going to be referred to as the “lower” and “upper” levels, respectively. It is important to note that the upper level is two-fold degenerate.

We calculated the bulk correction by the standard procedure, using the single-cell to this purpose. After determining the corrected potentials for the bulk, we studied the influence of these corrections on the character and position of the defect levels of interest, by applying the corrected potentials to different combinations of bulk atoms and first-neighbors (Table 4.3).

The first point to note is that the application of the correction to the bulk atoms has a very small influence on the transition energy. This was expected, since we are correcting hundreds of atoms, and even negligible effects can add up to noticeable changes. The correction on the bulk Gallium atoms has a small effect on the band gap, and as shown, has also a small effect on the defect levels. Therefore, we can still neglect it, as usual. Surprisingly, applying the correction to the Nitrogen atoms that are neighbors to the Chromium atom resulted in a significant shift, and therefore they must be considered as different atoms. The Gallium atoms that are neighbors to the vacancy does not have a significant contribution, in contrast to what happens in the NV^- center in diamond.

If we examine the character of the levels of interest, we find a simple explanation for what was observed in Table 4.3. As shown in Table 4.4, the only atoms that significantly contributes to the levels of interest are the Chromium atom and its Nitrogen neighbors,

TABLE 4.4 – Orbital character of the defect levels and fractions of an electron to be removed from and added to each potential (denoted by ξ and ζ , respectively). Only the defect and its first neighbors were considered in this table.

$X\phi$	Ground State			
	Lower Level	$\xi_{X\phi}$	Upper Level	$\zeta_{X\phi}$
Cr_s	4.17%	0.021	0.00%	0.000
Cr_p	0.54%	0.003	11.01%	0.055
Cr_d	87.30%	0.436	79.75%	0.399
Ga_s	0.54%	0.003	0.21%	0.001
Ga_p	1.09%	0.005	0.30%	0.001
Ga_d	0.18%	0.001	0.04%	0.000
N_s	0.00%	0.000	0.12%	0.001
N_p	0.85%	0.004	2.40%	0.012
N_d	0.00%	0.000	0.00%	0.000

which are precisely the atoms that caused a major change in the transition energy. The contribution of the Nitrogen atoms occurs mostly on the upper level. It is important to remember that there are 3 of these atoms, and therefore they correspond to 7.20% of this level. Applying the bulk correction to these atoms is equivalent to a strong deviation from their contribution since in the first case it is subtracted half electron from each of them, instead of adding $0.001 + 0.012 - 0.004 = 0.009$ electron.

It is a known limitation of the DFT-1/2 as currently implemented that it does not distinguish the angular momentum projection in the corrections. This is due to the fact that the DFT code used only accept spherically symmetrical potentials as input. Therefore, since both the upper and lower levels have a strong Cr-d character, the corrections would cancel each other, even though they would not necessarily cancel if it was considered that the character of the lower level is Cr-d(z^2) and the character of the upper levels, which are degenerated, are Cr-d(x^2) and Cr-d(xy). Since this coincidence of both levels having almost the same character is only common in d-type orbitals, our methodology is more indicated for defects that do not contain transition metals. For this reason, the study of the $\text{Cr}_{\text{Ga}}\text{V}_{\text{N}}$ center was not continued, but it is still important as a beginning of the systematic calculations and for highlighting interesting aspects of the methodology.

5 Qubit Based on van der Waals Heterostructures

In this chapter we propose a novel qubit concept, based on van der Waals heterostructures of two-dimensional materials. A particular case is studied, namely the $\text{ZrSe}_2/\text{SnSe}_2$ heterostructure, and other possible systems are indicated by estimating the band alignments using Anderson's rule. Before the actual proposal of the qubit, in order to highlight important aspects of it, a toy model that presents analogous behavior is developed and analyzed.

5.1 Quantum superposition and two-dimensional systems

The quantum superposition (QS) plays a major role in the so-called second generation of quantum technologies, which includes quantum cryptography, quantum imaging, quantum computing, and quantum sensing (GEORGESCU; NORI, 2012). The preparation, manipulation, and measurement of the QS are central aspects in order to reach the operation of these advanced devices. Such a superposition of two quantum states characterizes the unit of quantum information, a qubit. The QS or a qubit can be prepared by a system of two quantum states. Examples are the polarization of light (O'BRIEN *et al.*, 2003), energy levels in a two level system (SCHNEIDER; SAENZ, 2012), electron spin orientations (LAUCHT *et al.*, 2016).

Very attractive are solid-state quantum bits such as spin qubits with electrically tunable spin-valley mixing in silicon (CRIPPA *et al.*, 2018; BOURDET; NIQUET, 2018), the qubit of the two charge states of a negatively charged nitrogen vacancy in diamond (LUCATTO *et al.*, 2017; CHOU *et al.*, 2018), and the charge-qubit operation of an isolated double quantum dot (GORMAN *et al.*, 2005). All these examples show that isolated atomic-like structures in or of solids may be of interest for novel qubits, which may be used as building blocks of future quantum computers or quantum information devices. Recently, together with

the strong development of two-dimensional (2D) materials technology, efforts have been made to find possible candidates for a qubit in monolayer (PAWLOWSKI *et al.*, 2018) and multilayer (KHORASANI; KOOTTANDAVIDA, 2016) structures.

One interesting property of 2D materials is the possibility of van der Waals (vdW) heterostructures formation, which consists of the stacking of 2D sheet crystals (NOVOSELOV *et al.*, 2016). Despite the weak interaction of the two atomic layers in a 2D heterostructure, spatial QS can be formed between the wavefunctions localized in different layers but forming the conduction or valence bands of the heterostructure, if the band structures of the isolated layers are nearly aligned on an absolute energy scale (KODA *et al.*, 2018). For the orbitals localized in one subsystem pointing toward the other subsystem, their bonding and antibonding combinations build the basis functions of the joint conduction or valence band (KODA *et al.*, 2017). The resulting energy splittings and the mixing coefficients of the wavefunctions depend on the vdW layers distance and the natural band discontinuities. The mixing coefficients characterize the quantum-mechanical probabilities to find a certain carrier, electron or hole, in one 2D material of the heterostructure.

5.2 A Toy Model for the Dihydrogen Cation Under an Axial Electric Field

The dihydrogen cation H_2^+ , consisting of a single electron in the Coulomb field of two protons, is the simplest molecular system possible and, for that reason, is studied in many introductory Quantum Mechanics books, such as (HAGELSTEIN *et al.*, 2004; GRIFFITHS, 2004). For that simplicity, we will choose this molecule to study the behavior of an electron in a double-well potential system under the influence of an electric field. This will give insights and aid in the understanding of the phenomena explored in the van der Waals qubit, which is the object of study of this chapter. Moreover, this simple system has even more similarities and possible analogies with another important qubit concept, the double quantum dot qubit (GORMAN *et al.*, 2005). The system will be solved under the Linear Combination of Atomic Orbitals (LCAO) approximation, due to the simplicity of this approach. It is important to mention that the system does admit an exact solution in terms of special functions, but it happens to be overly complicated, what ultimately defeats the purpose.

5.2.1 Formulation

In this section, we present the definitions of the relevant quantities and the results for the proposed toy model. The complete formulation is given in Appendix A, to avoid

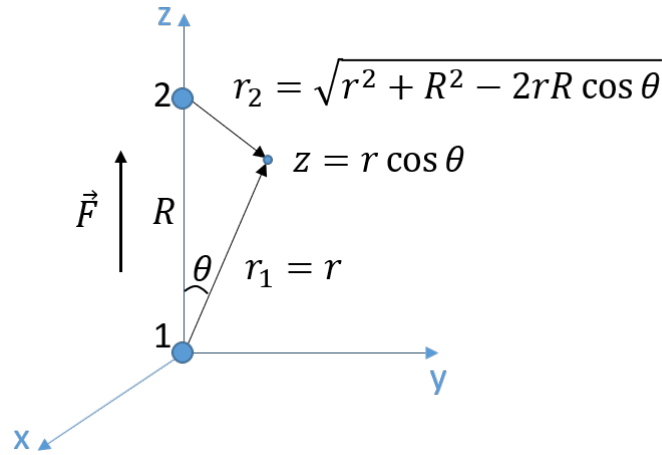


FIGURE 5.1 – Coordinates for the mathematical formulation of the dihydrogen cation system.

harnessing the reading with mathematical development.

Under the Born-Oppenheimer approximation, assuming that the atomic nuclei are fixed in position, with a specified distance R apart, the Hamiltonian for the electron is

$$H = -\frac{\hbar^2}{2m}\nabla^2 - \frac{e^2}{4\pi\epsilon_0}\left(\frac{1}{r_1} + \frac{1}{r_2}\right) + eFz = -\frac{\hbar^2}{2m}\nabla^2 + 2a_0E_0\left(\frac{1}{r_1} + \frac{1}{r_2}\right) + eFz \quad (5.1)$$

assuming S.I. units and where a_0 is the Bohr radius, E_0 is the ground state energy of the hydrogen atom, and $r_1 = |\mathbf{r}_1|$ and $r_2 = |\mathbf{r}_2|$ are the distances to the electron from the respective protons.

Using the simplest LCAO approximation, we will consider the electron's wavefunction to be a linear combination between the wavefunction of the ground state of the electron in a hydrogen atom, $\psi_0(r)$, centered in each nucleus. The ground state wavefunction of a hydrogen atom is (GRIFFITHS, 2004)

$$\psi_0(r) = \frac{e^{-r/a_0}}{\sqrt{\pi a_0^3}}. \quad (5.2)$$

Thus, our wavefunction can be written as

$$\psi(r) = \alpha\psi_0(r_1) + \beta\psi_0(r_2) = A[\psi_0(r_1) + \lambda\psi_0(r_2)], \quad (5.3)$$

where α and β are the mixing coefficients, A is the normalization constant, which we can choose to be a real number due to the non-observability of a global phase of the state, and λ is a complex number. In order to calculate the normalization constant, and considering that the displaced wavefunctions are not orthogonal, we define the overlap integral as

$I = \langle \psi_0(r_1) | \psi_0(r_2) \rangle$. Evaluating this integral, we obtain

$$I = e^{-R/a_0} \left[1 + \left(\frac{R}{a_0} \right) + \frac{1}{3} \left(\frac{R}{a_0} \right)^2 \right], \quad (5.4)$$

and the normalization constant can be written as

Calculating the expectation value of the Hamiltonian, it is useful to define the direct integral, $D = a_0 \langle \psi_0(r_2) | 1/r_2 | \psi_0(r_2) \rangle = a_0 \langle \psi_0(r_1) | 1/r_1 | \psi_0(r_1) \rangle$, and the exchange integral, $X = a_0 \langle \psi_0(r_1) | 1/r_2 | \psi_0(r_1) \rangle = a_0 \langle \psi_0(r_2) | 1/r_1 | \psi_0(r_2) \rangle$. Evaluating these integrals, we obtain

$$D = \frac{a_0}{R} - \left(1 + \frac{a_0}{R} \right) e^{-2R/a_0}, \quad (5.5)$$

and

$$X = \left(1 + \frac{R}{a_0} \right) e^{-R/a_0}. \quad (5.6)$$

Assuming that the nuclei are fixed in space, as is the case of quantum dots or the vdW heterostructure on a substrate, we find the values of λ that maximize and minimize the expectation value of the energy as a function of the field strength F .

$$\begin{aligned} \lambda_{max} &= \frac{-eFR - \sqrt{(eFR)^2(1 - I^2) + (4(DI - X)E_0)^2}}{eFIR + 4(DI - X)E_0} \\ \lambda_{min} &= \frac{-eFR + \sqrt{(eFR)^2(1 - I^2) + (4(DI - X)E_0)^2}}{eFIR + 4(DI - X)E_0}, \end{aligned} \quad (5.7)$$

which are always real numbers.

Including the energies due to the nucleus-nucleus repulsion and due to the nuclei in the electric field, we compute the total energy of the system, which is as a function of only the electric field, considering that R is fixed.

$$E_{tot} = \left(1 - 2\frac{a_0}{R} \right) E_0 + \frac{(D + 2X\lambda_{min} + D\lambda_{min}^2)2E_0 - (I\lambda_{min} + 1)eFR}{1 + \lambda_{min}^2 + 2I\lambda_{min}}. \quad (5.8)$$

The probabilities of finding the electron in atom 1 or in atom 2 are given, respectively, by

$$\begin{aligned} p_1 &= |\langle 1 | \psi \rangle|^2 = |\alpha + \beta I|^2 = \frac{(1 + I\lambda_{min})^2}{1 + \lambda_{min}^2 + 2I\lambda_{min}} \\ p_2 &= |\langle 2 | \psi \rangle|^2 = |\alpha I + \beta|^2 = \frac{(I + \lambda_{min})^2}{1 + \lambda_{min}^2 + 2I\lambda_{min}} \end{aligned} \quad (5.9)$$

5.2.2 Results and Discussion

The dihydrogen cation H_2^+ studied in (GRIFFITHS, 2004) is a particular case of the system studied here, when the field is null and $\lambda = 1$. Minimizing the energy in these particular conditions, we find $R_{min}=1.3\text{\AA}$, in agreement with (GRIFFITHS, 2004).

In order to increase the similarity between this model and the double quantum dot or the vdW heterostructure on a substrate, we keep the distance between the nuclei fixed, and thus we must choose one to work with. In this sense, $R = R_{min}$ is a natural choice and, therefore, we adopt it.

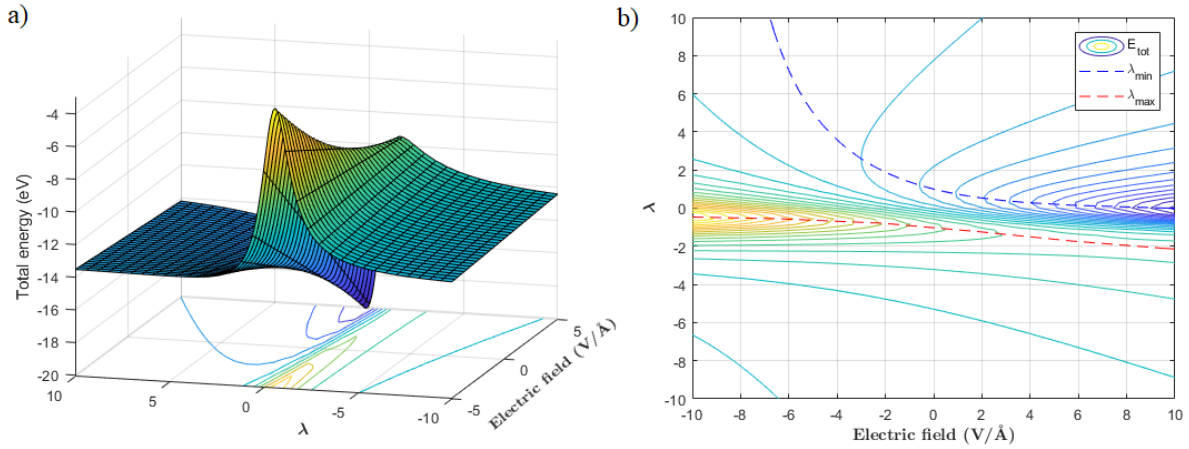


FIGURE 5.2 – (a) Total energy as a function of the electric field and the λ coefficient, for a fixed value of $R = R_{min}$. The values of λ which maximize and minimize the total energy for each field strength F are given by the red and blue dashed lines in the contour plot (b).

Figure 5.2(a) presents the total energy of the system as a function of the electric field and the λ coefficient, $E_{tot}|_{R_{min}}(F, \lambda)$. The λ values that are extrema of $\langle H \rangle$ are also extrema of E_{tot} , since the difference between these two functions is not a function of λ , not even implicitly since we are keeping R fixed. In Fig. 5.2(b), we superpose the contour plot of the total energy with the values of λ that extremize it for each value of the field F , given by Eqs. 5.2 with the substitution $R = R_{min}$. We note that the lines representing the extrema cross the contours whenever they are parallel to one of the axes, what is expected.

Since we have λ_{min} for all field strengths, we can compute the wavefunction given in Eq. 5.3 as a function of the electric field, and plot its values along the z axis. The result is presented in Fig. 5.3. It is possible to observe the symmetry of the solution with respect to the signal of the field strength F . When F is positive, the electron tends to be more localized around the nucleus at $z = 0$, and the opposite is true when F is negative.

Finally, we compute the probabilities of finding the electron around each nucleus, given by Eqs. 5.9. The results are presented in Fig. 5.4(a), and one can readily note that due

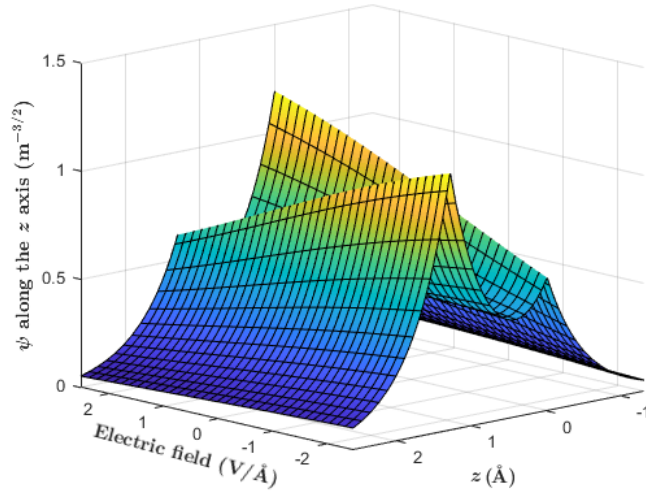


FIGURE 5.3 – The surface plot represents the values that the wavefunction along the z axis for a range of values of the electric field. One of the hydrogen nucleus is at $z = 0$, while the other is at $z = R_{min} = 1.3\text{Å}$.

to the overlap I being different from zero, the sum of the probabilities is greater than one. We then perform DFT calculations of the system, and following the same procedure, we choose to keep the distance between the nuclei fixed in the position of minimum energy at the null field, which is $R_{min,DFT} = 1.13\text{Å}$, closer to the experimental value of 1.06Å (GRIFFITHS, 2004).

The projections on atomic orbitals provided on the output of VASP need to be normalized. This is not a problem when the overlap between the projective functions is negligible, however, in the present case, this introduces a great distortion of the results. In order to compare the results, we normalize the probabilities p_1 and p_2 by their sum, resulting in

$$\begin{aligned}\bar{p}_1 &= \frac{p_1}{p_1 + p_2} \\ \bar{p}_2 &= \frac{p_2}{p_1 + p_2}.\end{aligned}\tag{5.10}$$

Figure 5.4(b) shows a good agreement between our model and the DFT solution, despite the simplicity of the former.

The study of this model, therefore, highlighted several aspects regarding the non-orthogonality of the projective basis, some of which are yet to be worked on, especially in what concerns the normalization of the projection provided by VASP. Moreover, in this model we are able to manipulate the position of the electron between one nucleus and the other by means of an electric field, using it to change the superposition coefficients. This effect will be explored in the proposal of the vdW qubit.

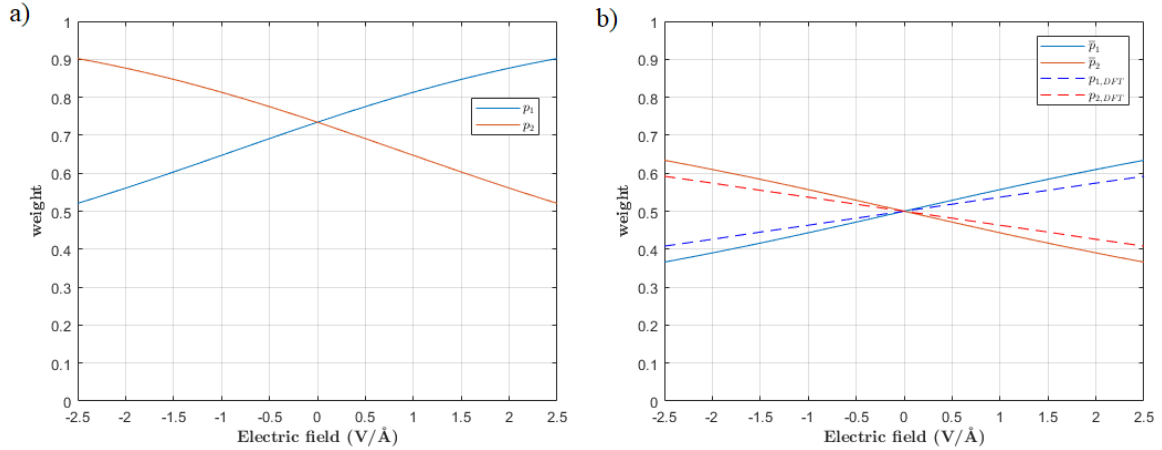


FIGURE 5.4 – (a) Probability of finding the electron around ions 1 (blue) and 2 (red) calculated using the LCAO model. (b) Comparison between the normalized probabilities calculated with the LCAO model (solid lines) and the DFT simulation (dashed lines)

5.3 The van der Waals Qubit

5.3.1 Computational details

The structural and electronic properties are calculated using the density functional theory (DFT) as implemented in the Vienna Ab-initio Simulation Package (VASP) (KRESSE; FURTHMÜLLER, 1996b). The wave functions and pseudopotentials are generated within the projector-augmented wave (PAW) method (KRESSE; JOUBERT, 1999). Exchange and correlation (XC) are described using the Perdew-Burke-Ernzerhof (PBE) functional within the generalized gradient approximation (GGA) (PERDEW *et al.*, 1996a). Van der Waals interaction is taken into account using the optB86b functional (KLIME *et al.*, 2011). The kinetic energy cutoff of the plane wave expansion is restricted to 500 eV. Integrations over the 2D Brillouin zone (BZ) are performed using an $11 \times 11 \times 1$ Γ -centered Monkhorst-Pack k-points mesh (MONKHORST; PACK, 1976) for 1×1 lateral unit cells. The repeated slab method is applied to simulate individual 2D crystals (BECHSTEDT, 2003). A vacuum thickness of 15 \AA is employed to avoid unphysical interaction in stacking direction. Since a charge transfer may occur in vdW heterostructures, dipole corrections are applied to satisfy the periodic boundary conditions for the supercells. Ionization energies I and electron affinities A of the isolated atomic layers are determined as differences of valence band maximum (VBM) and conduction band minimum (CBM) to the vacuum level defined by vanishing electrostatic potential (KODA *et al.*, 2017).

Minimum lateral unit cells employed are found using the coincidence lattice method (KODA *et al.*, 2016). Heterostructure investigations are performed after fixing the parameters of the most stable structural geometry for each monolayer and applying necessary strains to make the systems commensurate. We make sure that the resulting biaxial strain

in the 2D crystals is smaller than 2% and that there are no more than atoms inside the joint lateral cell. All structural parameters are calculated first finding the energy minimum with a stopping criterion of 10^{-5} eV for the energy convergence and then relaxing the atomic positions until the Hellmann-Feynman forces on atoms are smaller than $1 \text{ meV}/\text{\AA}$.

Electronic properties calculated using the DFT functional lead to 2D band structures which suffer from the typical underestimation of energy gaps and interband distances computed as differences of Kohn-Sham eigenvalues of the DFT (PAIER *et al.*, 2006). Therefore, they also lead to an incorrect description of hybridization and band offsets in vdW heterostructures (KODA *et al.*, 2017). To account for the excitation aspect we add approximate quasiparticle corrections to the Kohn-Sham bands by applying the XC hybrid functional HSE06 (PAIER *et al.*, 2006; HEYD *et al.*, 2003; HEYD *et al.*, 2006) to compute the electronic band structures and energy alignments.

5.3.2 Effect of vertical electric field on band structure

In order to illustrate the superposition of states for electrons and holes in biased 2D AB heterostructures, we start with an AB model system consisting of A=ZrSe₂ and B=SnSe₂ atomic triple layers. Because of the near lattice match, 1x1 cells with zero twist and small antisymmetric biaxial strain of ± 0.008 are chosen (KODA *et al.*, 2017). A vertical electric field \vec{F} simulates that the AB heterostructure is gated or vertically biased as displayed in the inset of Fig. 5.5(a). The band structures resulting for three field strengths are plotted in Fig. 5.5 along high-symmetry directions in the Brillouin zone (BZ) for a small energy interval around the fundamental gap. The indirect semiconductor character of the conduction band minimum (CBM) at M and the valence band maximum (VBM) at Γ is conserved for all field strengths. In Fig. 5.5, the color of each eigenvalue represents the relative contribution of each sheet crystal A or B to the wavefunction. It is obtained as the proportion of the projections of the Kohn-Sham orbitals onto the atomic orbitals (*i.e.*, the orbital character of these levels (LUCATTO *et al.*, 2017)), for all the atoms in the A or B material. Most interesting for the preparation of a qubit represented by a two-level system are the two lowest conduction bands at the M point in the BZ. The lower conduction band state at M may be denoted by $|0\rangle$, while the next higher conduction band state $|1\rangle$ is higher in energy by a value $\Delta \approx 0.3$ eV but at the same \vec{k} point. The most interesting hole state is the VBM at Γ . It is denoted by $|h\rangle$. All these band states are generally composed by wavefunctions, which are localized at one of the sheet crystals A or B. Figure 5.5 clearly shows that their contribution can be manipulated by external field \vec{F} .

In the unbiased case, Fig. 5.5(a), $|0\rangle$ and $|1\rangle$ have almost equal contributions of each layer of the junction as indicated by the green dots. This means that, in the absence

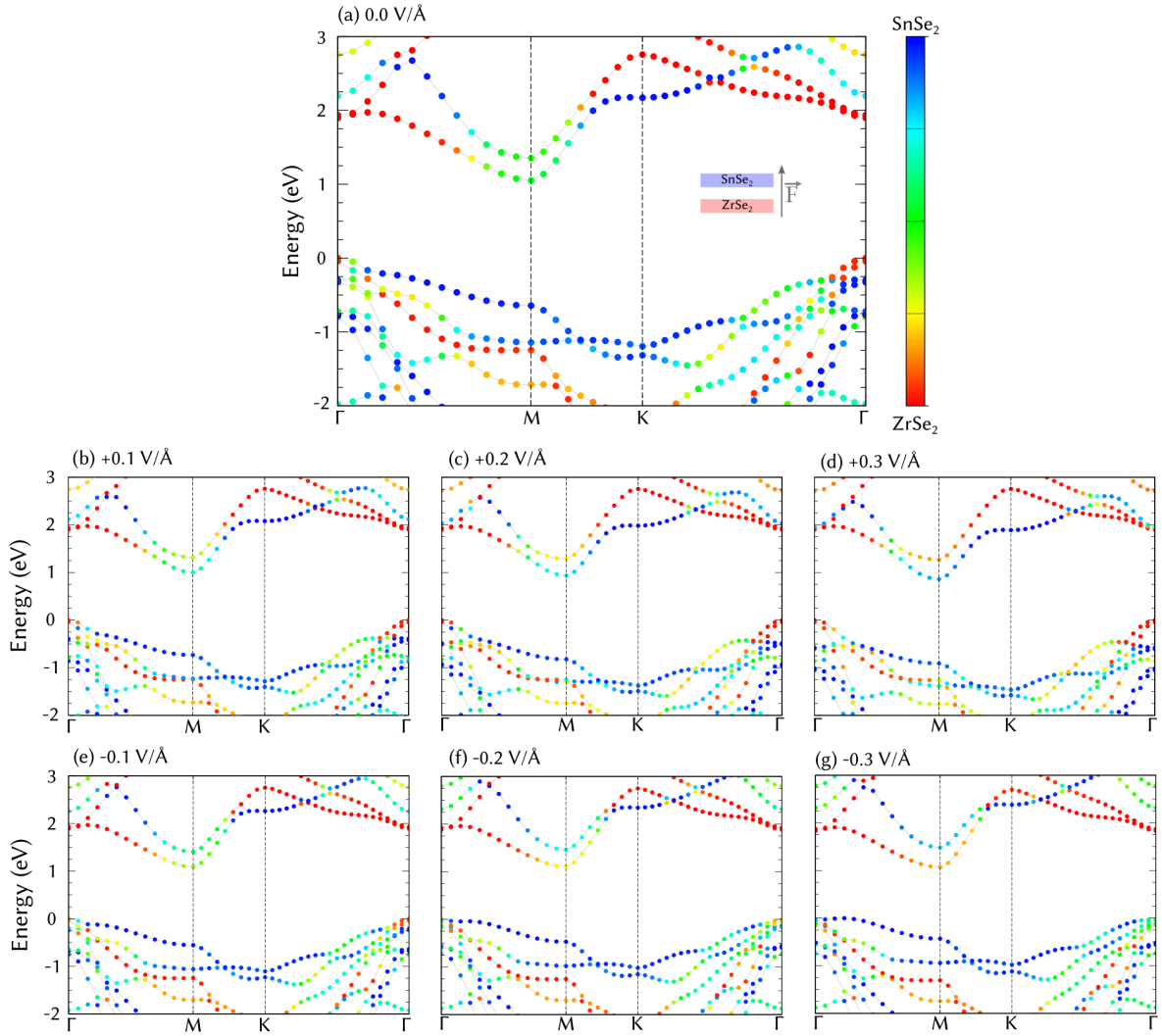


FIGURE 5.5 – Band structures of ZrSe₂/SnSe₂ heterostructure for different values of the vertical electric field. The inset in (a) shows the positive field orientation is considered from the ZrSe₂ layer to the SnSe₂ layer. The color of a dot in a Bloch band represents the relative contribution of each monolayer to the eigenvalue. The VBM is chosen as energy zero.

of the electrical field, an electron in one of these states tends to be in a superposed electronic state with equal probabilities to find the carrier due to material A and B. Instead, a superposition of the wavefunctions that belong to material A or to material B as illustrated in Fig. 5.6(b). This behavior is different from what happens in the top valence band state. $|h\rangle$ has a strong character of material A, as indicated by the red color of the VBM in Fig. 5.5(a). Therefore, a hole tends to be localized in sheet A. However, Fig. 5.5(a) also shows that slightly away from the Γ point the Bloch wave function may drastically change its localization in dependence on the direction of the wave vector.

A vertical external electric field, as indicated for the gated bilayer in the inset of Fig. 5.5(a), has a strong effect on the band states, shifting them relatively to each other in energy in Figs. 5.5(b to g). The change in energy also impacts the hybridization of the

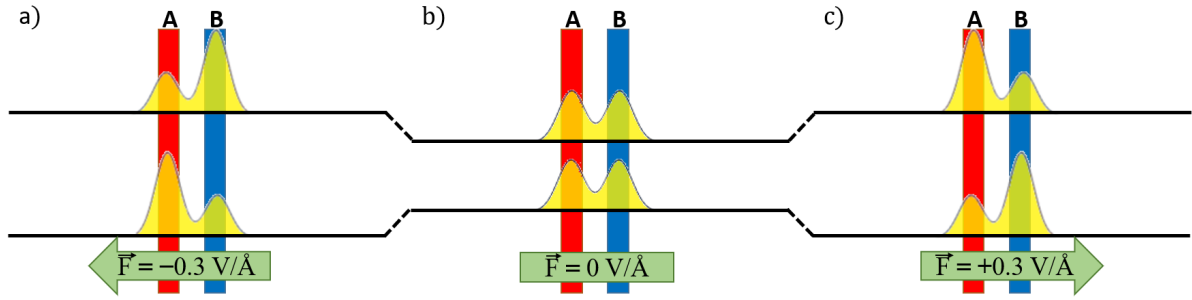


FIGURE 5.6 – Qualitative representation of the squared moduli of the wavefunctions for states $|0\rangle$ and $|1\rangle$ for positive (a), vanishing (b), and negative (c) electric fields.

orbitals, their overlap, and their relative contribution to the bilayer wave function. By applying an electric field in the A-B direction, electrons in the lowest CBM are lowered in energy. The electric field then “pulls down” the band structure of material B relatively to the band structure of material A, and consequently turns $|0\rangle$ in a state with a stronger character of material B, as indicated by the dot colors of the lower CBM in Figs. 5.5(b to d). As $|0\rangle$ becomes more localized in material B, $|1\rangle$ becomes more localized in state A. In the valence band, $|h\rangle$ becomes almost completely localized in sheet A. The consequences for the wave function localization are schematically depicted in Fig. 5.6c.

The opposite is true when applying an electric field in the reverse direction: the bands of material B are “shifted up”, conceiving to $|0\rangle$ a stronger localization in material A. As $|0\rangle$ becomes more localized in material A, $|1\rangle$ becomes more localized in state B, as indicated in Figs. 5.5(e to g), and schematically depicted in Fig. 5.6a. However, this is not the only effect observed in this case. Since the band structure of material B is shifted toward higher absolute energies, the VBM of material B starts to line up with the VBM of material A, and thus $|h\rangle$ exhibits a stronger hybridization and nearly equal contributions from both sheets A and B, as indicated by the colors of Fig. 5.5(g). Moreover, for this extreme value of the electric field, the VBM is shifted from Γ , which is not true for the intermediate values. See Section 5.3.4 for a more detailed discussion on the hole states.

There is a complementarity between $|0\rangle$ and $|1\rangle$ under the influence of the gate field, where one state becomes more localized in one sheet as the other becomes more localized in the other sheet. Therefore, an electron occupying any superposition of these two states configures a charge qubit in the AB heterostructure, where for strong positive electric fields the $|0\rangle$ and $|1\rangle$ states are localized in sheets B and A, respectively, and the opposite happens for strong negative electric fields. The corresponding energy configuration is illustrated schematically in Fig. 5.7 as a function of the electric field. Anticrossing energy $\Delta_{AC} = 0.30$ eV is determined by the difference between the eigenenergies of $|1\rangle$ and $|0\rangle$ for the wavefunction, in which the contribution of each layer is the same. This energy difference corresponds to oscillations of frequency $\omega \approx 450$ THz. In the studied

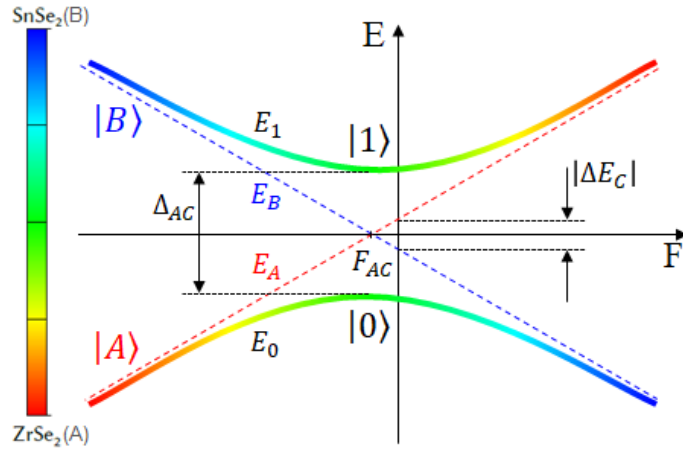


FIGURE 5.7 – Conduction-band energy level diagram versus gate-field strength F together with the localized electron states for an uncoupled system $|A\rangle$ and $|B\rangle$ (dashed lines) with eigenenergies E_A and E_B , respectively. The hybridization of the states for the coupled system results in new eigenstates $|0\rangle$ and $|1\rangle$, with eigenenergies E_0 and E_1 , respectively, and anticrossing energy Δ_{AC} (solid lines). For strong fields the qubit eigenstates are well approximated by $|A\rangle$ and $|B\rangle$, but for fields values around F_{AC} the eigenstates are strongly delocalized. For the null field, $E_B - E_A = \Delta E_C$, *i.e.*, the conduction band discontinuity.

system, this occurs at nearly vanishing field $F_{AC} \approx -15\text{mV}/\text{\AA}$. The conduction-level system, therefore, has similarities with the charge qubit suggested in a double quantum dot (GORMAN *et al.*, 2005). The difference in energy between these two states as a function of the vertical electric field F is plotted in Fig. 5.8. The actual field variation of $E_1 - E_0$ in Fig. 5.8 exhibits a nearly parabolic behavior, *i.e.*, it is almost independent of the field orientation.

The contribution of each layer A or B to the Bloch wave function of the states $|0\rangle$ and $|1\rangle$ in the AB heterostructure strongly depends on the electric field strength F . Therefore, any electron wave function $|\psi(F)\rangle$ of the AB heterostructure is mainly a combination of the corresponding wave functions $|A\rangle$ and $|B\rangle$ of the two individual atomic sheets with different weights. It can be written as a superposition for a given field strength F

$$|\psi(F)\rangle = \alpha_\psi(F) |A\rangle + \beta_\psi(F) |B\rangle \quad (5.11)$$

with complex but normalized coefficients, such that $|\alpha_\psi(F)|^2 + |\beta_\psi(F)|^2 = 1$. Because of the vdW gap between the two sheets the overlap of the functions $|A\rangle$ and $|B\rangle$ is neglected. Their squared moduli give the weights of each sheet to that wavefunction, as illustrated in Fig. 5.9, which presents similar qualitative behavior as the one obtained using the simple model, Fig. 5.4. The figure also provides evidence for the complementarity between $|0\rangle$ and $|1\rangle$, which further justifies the usage of the system as a charge qubit realized in the sheet arrangement. The representation of Eq. (5.11) can be also interpreted as a coherent

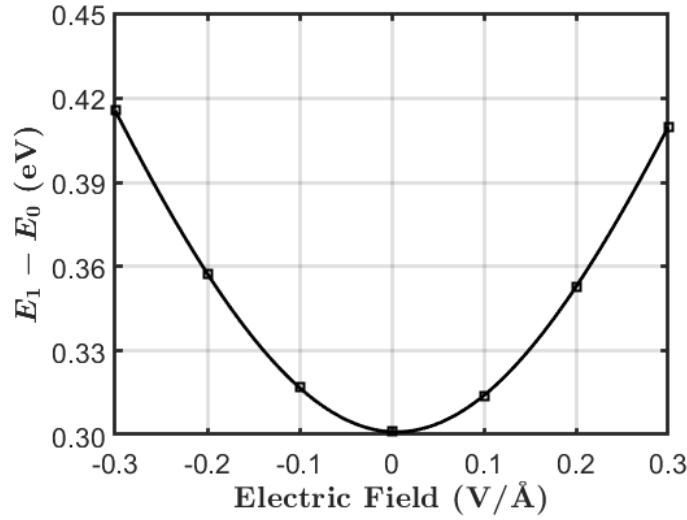


FIGURE 5.8 – Difference between the eigenenergies $E_1 - E_0$ as a function of the vertical electric field.

superposition of basic quantum states $|A\rangle$ and $|B\rangle$ at a given time or field strength, where the probability amplitudes α_ψ , β_ψ to find an electron characterize a linear combination as in a single qubit (SCHUMACHER, 1995). In a linear approximation around the state of maximum delocalization, considering it to be exactly at the unbiased case, one finds for the biased ZrSe₂/SnSe₂ heterostructure

$$\left\{ \begin{array}{l} |\alpha_0(F)|^2 \\ |\beta_0(F)|^2 \end{array} \right\} = \left\{ \begin{array}{l} |\beta_1(F)|^2 \\ |\alpha_1(F)|^2 \end{array} \right\} = \frac{1}{2} \left(1 \mp 2.9[\text{\AA}/\text{V}]F \right). \quad (5.12)$$

The states $|\psi(F)\rangle$ of Eq. 5.11 can be described as a Bloch vector in the standard Bloch sphere representation, where the mixing coefficients are described by spherical coordinates with angles θ and ϕ as

$$\begin{aligned} \alpha &= \cos(\theta/2) \\ \beta &= e^{i\phi} \sin(\theta/2) \end{aligned} \quad (5.13)$$

The polar angle θ can be calculated as

$$\theta = 2 \arccos(|\alpha|) = 2 \arcsin(|\beta|). \quad (5.14)$$

For the considered values of the electric field, the Bloch vector lies in the shaded area depicted in the inset of Fig. 5.9, which corresponds to the interval between $\theta \approx 45^\circ$ and $\theta \approx 135^\circ$. Considering $|F| < 0.1 \text{V}/\text{\AA}$, where the linear approximation introduces just a small error, the vector lies in the dark gray area in the inset of Fig. 5.9.

5.3.3 Usage as qubit:

A general state $|\psi\rangle$ on this two-level system for a given field F can be expanded in the energy eigenvector basis as $|\psi\rangle = \xi|0\rangle + \eta|1\rangle$. Considering that $|0\rangle = \alpha_0|A\rangle + \beta_0|B\rangle$ and $|1\rangle = \alpha_1|A\rangle + \beta_1|B\rangle$, the expansion in the A/B basis will be given by $|\psi\rangle = \alpha_\psi|A\rangle + \beta_\psi|B\rangle$, where

$$\begin{aligned}\alpha_\psi &= \xi\alpha_0 + \eta\alpha_1 \\ \beta_\psi &= \xi\beta_0 + \eta\beta_1\end{aligned}\quad (5.15)$$

A possible application of this system as a quantum bit is to initialize the system in the desired state, by choosing a suitable vertical electrical field amplitude and allowing the system to relax to ensure the electron is in the CBM, *i.e.*, in the state $|0\rangle$. In order to apply single-qubit gate operations, the gate field would be set to another value, and thus changing the two-level system's Hamiltonian itself, since the Hamiltonian is a function of the field strength F . If this change is made in a slow manner, the coefficients on the eigenvectors basis ξ and η would stay the same, under the conditions of the adiabatic theorem. Therefore, the electron would stay in state $|0\rangle$, regardless of the wavefunction of $|0\rangle$ being different from the starting one, which implies that α_ψ and β_ψ changed. On the other hand, if the change of the electric field is fast enough, the electron wavefunction would stay approximately the same during the whole process, *i.e.*, α_ψ and β_ψ would stay

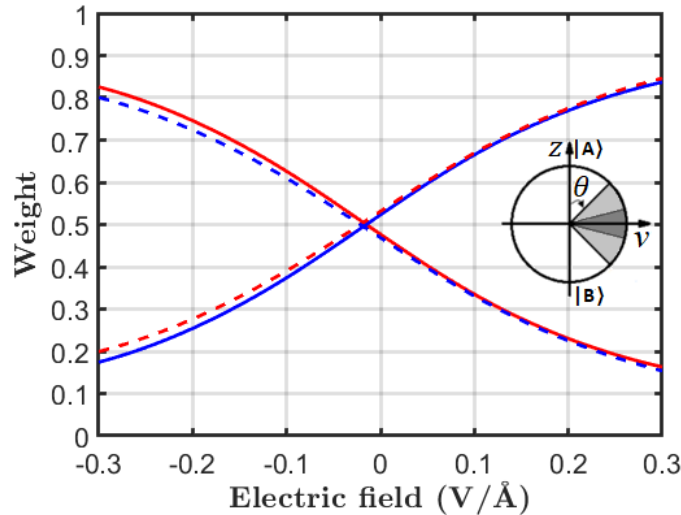


FIGURE 5.9 – Weights $|\alpha_\psi|^2$ (red) and $|\beta_\psi|^2$ (blue), for $|\psi\rangle$ equals $|0\rangle$ (solid lines) and $|1\rangle$ (dashed lines), as a function of the applied vertical electric field. The inset represents the area of the Bloch sphere in which $|0\rangle$ and $|1\rangle$ are comprised for the considered electric fields ($|F| < 0.3\text{V}/\text{\AA}$) (light gray), and for small fields ($|F| < 0.1\text{V}/\text{\AA}$) (dark gray) considering a generic azimuthal angle ϕ . The horizontal axis indicates the direction of the vector $\hat{v} = \cos \phi \hat{x} + \sin \phi \hat{y}$ in the xy -plane.

constant. Together with the fact that the coefficients of the energy eigenstates in the A/B basis change with the electric field, this implies that ξ and η would change. This opens the possibility of moving the electron to the excited state without recurring to optical excitations. In order to measure the resulting state, the carrier concentration in each sheet must be measured in a time window and compared.

An example of operation would be to prepare the initial state of the system with a strong negative field, *i.e.*, to start with $|0\rangle \approx |A\rangle$ and $|1\rangle \approx |B\rangle$, then suddenly change the electric field to a strongly positive one. Considering the field switch happens fast enough, the electron state remains the same, *i.e.*, $|A\rangle$ or $|B\rangle$, but now this state corresponds to the opposite eigenstate of the new Hamiltonian, *i.e.*, $|1\rangle$ or $|0\rangle$, respectively. Therefore, by doing so, a Pauli-X quantum gate was applied to the qubit. Applying an additional external bias in the horizontal direction in each sheet, a small carrier drift can be induced, and by measuring the resulting currents the carrier concentration in the layers can be compared.

Since the variation of the orbital character of a band is continuous with respect to the crystal momentum (see Fig. 5.5), even if more than one electron is excited, we can assume it will have approximately the same mixing coefficients as the first one. The Pauli exclusion principle is satisfied due to the difference in the crystal momentum quantum number. Therefore, it may be possible to perform the same operation with many electrons at the same time, if the decoherence time does not decrease too much due to carrier collisions. This would allow for a single measurement operation since the desired statistics of the result would be given by the relative amplitude between the currents flowing through each sheet. Experimental realization of the qubit should give a measure of how the (electro)chemical potential positioning affects the decoherence time. Besides, since $\Delta \gg k_B T$, where k_B is the Boltzmann constant and T is the room temperature, we expect the system to operate at high temperatures.

5.3.4 Conduction by holes

In order to work as a qubit as proposed, the ZrSe₂/SnSe₂ vdW heterostructure must have electrons in its conduction band. One easy way to produce them is to excite electrons from the valence band via optical radiation, creating an electron-hole pair. Therefore, for such a method, the analysis of the charge on the sheets must include the effects of the hole wavefunction in the device operation. The following analysis does not take into account excitonic and spin-orbit coupling effects, and thus are only general trends that might have small deviations from the actual behavior of the system.

As indicated in Fig. 5.5, in this heterostructure, an electron in the lower CBM and a hole at the VBM move in the opposite direction, thereby, forming a vertical dipole. This

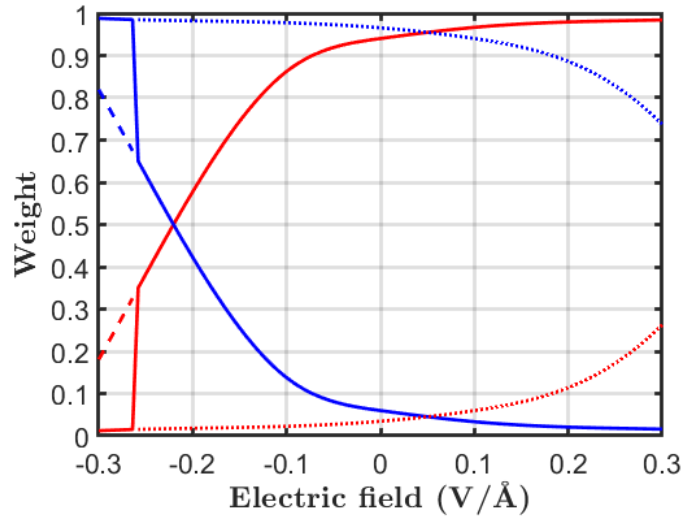


FIGURE 5.10 – Weights $|\alpha_h|^2$ (red, solid line) and $|\beta_h|^2$ (blue, solid line), as a function of the applied vertical electric field. The dashed lines indicate the weights for the maximum valence band state at Γ and the dotted lines indicate the weights for the maximum valence band state at the reciprocal space position of the VBM for $F = -0.3\text{V}/\text{\AA}$.

will not happen for an electron in the upper conduction state $|1\rangle$.

As the field becomes more negative, the bands of material B are shifted up. At $F \approx -0.26\text{V}/\text{\AA}$, a bump in its valence band is raised above the energy level of the maximum valence band state at Γ , resulting in the VBM of the heterostructure being shifted from Γ to a point between Γ and M, as indicated in Fig. 5.5(g). This causes a step change in the weights α_h and β_h , since the characters of these states are substantially different for this value of F , as indicated in Fig. 5.10.

The fact that the holes change their localization from one sheet to the other depending on the electric field value makes the comparison between the electrical current of electrons not straight forward, so engineering the (electro)chemical potential position by n-type doping would be preferable than producing free carriers by optical absorption transitions.

5.3.5 Similar systems

The weights $|\alpha_\psi(F)|^2$ and $|\beta_\psi(F)|^2$ are strongly related to the “natural” band discontinuities ΔE_C and ΔE_V of the band structures of the two sheet materials A and B forming the AB heterostructure, at least for vanishing gate field $F \rightarrow 0$ (KODA *et al.*, 2018). This has been demonstrated in Fig.4 of the main text. The Anderson rule (ANDERSON, 1962) is a first approximation to predict the alignment of the band structures of the individual sheets in the heterostructure. Thus, they should allow predicting also other possible A and B heterosystems for charge vdW qubits.

TABLE 5.1 – Difference in energy between the conduction and valence bands of several pairs of materials, *i.e.*, the band discontinuities ΔE_C and ΔE_V (in eV). In green are the systems that present a misalignment lower than 0.3 eV, in yellow the ones that are between 0.3 eV and 0.6 eV and in red the ones that are greater than 0.6 eV. All the values are given in eV.

A \ B	hBN		HfS ₂		ZrS ₂		ZrSe ₂		MoS ₂		MoSe ₂		WS ₂		WSe ₂		SnS ₂		SnSe ₂	
	ΔE_C	ΔE_V	ΔE_C	ΔE_V	ΔE_C	ΔE_V	ΔE_C	ΔE_V	ΔE_C	ΔE_V	ΔE_C	ΔE_V	ΔE_C	ΔE_V	ΔE_C	ΔE_V	ΔE_C	ΔE_V	ΔE_C	ΔE_V
hBN	0.00	0.00	-3.98	0.22	-4.20	0.25	-4.06	-0.65	-3.09	-0.47	-2.79	-1.06	-2.84	-0.67	-2.39	-1.31	-4.02	0.58	-4.17	-0.25
HfS ₂	3.98	-0.22	0.00	0.00	-0.22	0.03	-0.08	-0.87	0.89	-0.69	1.19	-1.28	1.14	-0.89	1.59	-1.53	-0.04	0.36	-0.19	-0.47
ZrS ₂	4.20	-0.25	0.22	-0.03	0.00	0.00	0.14	-0.90	1.11	-0.72	1.41	-1.31	1.36	-0.92	1.81	-1.56	0.18	0.33	0.03	-0.50
ZrSe ₂	4.06	0.65	0.08	0.87	-0.14	0.90	0.00	0.00	0.97	0.18	1.27	-0.41	1.22	-0.02	1.67	-0.66	0.04	1.23	-0.11	0.40
MoS ₂	3.09	0.47	-0.89	0.69	-1.11	0.72	-0.97	-0.18	0.00	0.00	0.30	-0.59	0.25	-0.20	0.70	-0.84	-0.93	1.05	-1.08	0.22
MoSe ₂	2.79	1.06	-1.19	1.28	-1.41	1.31	-1.27	0.41	-0.30	0.59	0.00	0.00	-0.05	0.39	0.40	-0.25	-1.23	1.64	-1.38	0.81
WS ₂	2.84	0.67	-1.14	0.89	-1.36	0.92	-1.22	0.02	-0.25	0.20	0.05	-0.39	0.00	0.00	0.45	-0.64	-1.18	1.25	-1.33	0.42
WSe ₂	2.39	1.31	-1.59	1.53	-1.81	1.56	-1.67	0.66	-0.70	0.84	-0.40	0.25	-0.45	0.64	0.00	0.00	-1.63	1.89	-1.78	1.06
SnS ₂	4.02	-0.58	0.04	-0.36	-0.18	-0.33	-0.04	-1.23	0.93	-1.05	1.23	-1.64	1.18	-1.25	1.63	-1.89	0.00	0.00	-0.15	-0.83
SnSe ₂	4.17	0.25	0.19	0.47	-0.03	0.50	0.11	-0.40	1.08	-0.22	1.38	-0.81	1.33	-0.42	1.78	-1.06	0.15	0.83	0.00	0.00

The general result is that electron and hole distributions over the atomic sheets in a heterocombination can be only significantly modified by an external vertical electric field F for small band discontinuities ΔE_C and ΔE_V . Considering field strengths of the order of $F = 0.1\text{V}/\text{\AA}$ and vdW gaps between the sheets of about $d = 3\text{\AA}$, field-induced modification of the band structure of energies $eFd = 0.3\text{ eV}$ appear as observed from Fig. 5.5. Consequently, hetero-combinations with maximum band discontinuities of about $|\Delta E_C|$ or $|\Delta E_V| \approx 0.3\text{ eV}$ may be switched with the gate voltage.

Besides the trivial match when the materials are the same, we observe that out of the 45 possible combinations, there are 13 with matching conduction bands and 9 with matching valence bands, as shown in Table 5.1. Moreover, between these combinations there are only two, HfS₂/ZrS₂ and MoS₂/WS₂, with a simultaneous match between both the valence and conduction bands. The explicit values are $\Delta E_C = -0.22$ (0.25) eV and $\Delta E_V = 0.03$ (-0.20) eV for HfSe₂/ZrS₂ (MoS₂/WS₂), indicating that both heterostructures are of type II as also the model system ZrSe₂/SnSe₂.

Other extreme band alignments occur in the types II and III heterostructure cases, the staggered-gap and broken-gap systems, respectively, where the valence band of one material is aligned with the conduction band of the other material. Among the 45 hetero-combinations studied only the systems ZrSe₂/WSe₂ and SnSe₂/WSe₂ approach this situation, all of them being of type II. The CBM of ZrS₂ (SnSe₂) is only 0.29 (0.32) eV above the VBM of WSe₂, as shown in Table 5.2. Consequently, there should be a wave function overlap of the conduction-band functions of the A sheet and the valence-band functions of the B sheet. Tunneling of electrons from the B=WSe₂ side into the A=ZrS₂ or SnSe₂ sheet should be possible.

Under the action of a negative gate field, oriented from A to B, this tendency will be enforced until strong tunneling of electrons from the valence band of one sheet into the conduction band of the other happens. In the opposite field direction, the band alignment tends toward a pronounced type II heterostructure character. Experimental studies of vdW heterostructure devices based on the WSe₂/SnSe₂ combination (ROY *et al.*, 2016) seem to imply that efficient carrier tunneling can be obtained by applying moderate gate voltages. This is in line with the above theoretical predictions.

TABLE 5.2 – Difference in energy between the conduction band minimum of the materials in the columns with the valence band maximum of the materials in the rows. In green are the systems that present a misalignment lower than 0.3 eV, in yellow the ones that are between 0.3 eV and 0.6 eV and in red the ones that are greater than 0.6 eV. All the values are given in eV.

		Conduction									
		hBN	HfS ₂	ZrS ₂	ZrSe ₂	MoS ₂	MoSe ₂	WS ₂	WSe ₂	SnS ₂	SnSe ₂
Valence	hBN	5.80	1.82	1.60	1.74	2.71	3.01	2.96	3.41	1.78	1.63
	HfS ₂	6.02	2.04	1.82	1.96	2.93	3.23	3.18	3.63	2.00	1.85
	ZrS ₂	6.05	2.07	1.85	1.99	2.96	3.26	3.21	3.66	2.03	1.88
	ZrSe ₂	5.15	1.17	0.95	1.09	2.06	2.36	2.31	2.76	1.13	0.98
	MoS ₂	5.33	1.35	1.13	1.27	2.24	2.54	2.49	2.94	1.31	1.16
	MoSe ₂	4.74	0.76	0.54	0.68	1.65	1.95	1.90	2.35	0.72	0.57
	WS ₂	5.13	1.15	0.93	1.07	2.04	2.34	2.29	2.74	1.11	0.96
	WSe ₂	4.49	0.51	0.29	0.43	1.40	1.70	1.65	2.10	0.47	0.32
	SnS ₂	6.38	2.40	2.18	2.32	3.29	3.59	3.54	3.99	2.36	2.21
	SnSe ₂	5.55	1.57	1.35	1.49	2.46	2.76	2.71	3.16	1.53	1.38

6 Conclusion

In summary, we studied solid state systems focusing on their application as qubits. We first present an experiment on a real quantum processor, through the IBM Quantum Experience, which is an online platform that gives users in the general public access to a set of IBM's prototype quantum processors via the Cloud, being an example of cloud-based quantum computing. In the experiment, we both demonstrate how quantum information can be processed and give an example that highlights how quantum algorithms are not just probabilistic computation. We then present a review on the use of NV^- centers in diamond as qubits, and develop a toy model for its operation that reduces the complexity of the quantum interactions to the simplicity of a Markov chain, by assuming the validity of rate equations, enlightened by the ideas of Einstein in its famous study of the quantum theory of radiation. The model helps understanding how the spin configuration determines the intensity of the irradiated light.

Understanding that the NV^- center in diamond has some drawbacks due to the fact that diamond as a host does not allow it to be integrated with other microelectronics devices with current technology, and that it is, therefore, greatly desirable to find an analogous system in a host material more technologically mature than diamond, we develop a method to approximate quasiparticle corrections in the study of complex defects in semiconductors, based on a methodology to correct band gaps called LDA-1/2. Since computing time is one of the most limiting aspects of the techniques that go beyond DFT to adequately predict properties regarding excited states, including the transition energies, the method developed in this work greatly contributes to this field of research, allowing the calculation of various different combinations of host materials and complex defects, and helping in the characterization of these defects through spectroscopy. We also presented results for the application of the proposed method to a complex-defect in gallium nitride, which permitted us to further understand some characteristics of these corrections. Gallium nitride was chosen as a possible host due to its large band gap and its extensive use on the microelectronic industry. The study of defects in GaN introduced some additional complexity, especially because it is a binary compound and because of its wurtzite structure, which has a lower symmetry than the diamond structure.

Similarly to a classical bit where the state of a transistor in a processor, the magneti-

zation of a surface in a hard disk and the presence of current in a cable can all be used to represent bits in the same computer, an eventual quantum computer is likely to use various combinations of qubits in its design. We aimed to contribute to this matter by proposing a new concept of a qubit, based on a spatial quantum superposition state in the conduction bands of van der Waals heterostructures with small natural band discontinuities, which we show that can be manipulated by a gate field perpendicular to the 2D crystals. In order to better understand the physical concepts explored in vdW qubit proposal, we first develop a toy model based on the dihydrogen cation H_2^+ under the effects of an axial electric field, which highlights important aspects regarding the manipulation of the position of an electron in a double-well structure by means of an electric field and the use of the projections on each side of the double-well as a measuring basis. Finally, we performed rigorous *ab initio* calculations for the model vdW heterostructure consisting of atomic sheets of $ZrSe_2$ and $SnSe_2$ for several values of the perpendicular electric field. We obtained quantitative conduction band structures which clearly showed the feasibility of controlling the probability of the electron being on a specific side of the heterostructure by the external field. We proposed to use the system as a charge qubit, by proposing possible methodologies to initialize, manipulate and measure its state. The qubit is based in a robust electronic state, possibly does not require optical apparatus nor cryogenic operating temperatures, and is compatible with the technology of 2D electronic devices.

Therefore, the fast and accurate method to simulate complex defects in semiconductors and the novel concept of qubit based on gated vdW heterostructures may pave the way for developing new physical implementations of qubits. Together with the instructive and concise toy models here developed, this work contributed to the scientific community of physics and engineering in the area of quantum information devices.

Bibliography

ADAMO, C.; BARONE, V. Toward reliable density functional methods without adjustable parameters: The PBE0 model. **Journal of Chemical Physics**, vol. 110, no. 13, p. 6158–6170, 1999. ISSN 00219606.

ALLEN, L.; EBERLY, J. H. **Optical resonance and two-level atoms**. [S.l.]: Courier Corporation, 2012.

AMANO, H.; KITO, M.; HIRAMATSU, K.; AKASAKI, I. n P-Type Conduction in Mg-Doped GaN Treated with Low-Energy Electron Beam Irradiation (LEEBI). **Japanese Journal of Applied Physics**, vol. 28, no. Part 2, No. 12, p. L2112–L2114, 1989. ISSN 0021-4922.

ANDERSEN, O. K. Linear methods in band theory. **Physical Review B**, vol. 12, no. 8, p. 3060–3083, oct 1975. ISSN 0556-2805.

ANDERSON, R. L. Experiments on Ge-GaAs Heterojunctions. **IRE Transactions on Electron Devices**, vol. 9, no. 6, p. 509, 1962. ISSN 00962430.

ATAIDE, C. A.; PELÁ, R. R.; MARQUES, M.; TELES, L. K.; FURTHMÜLLER, J.; BECHSTEDT, F. Fast and accurate approximate quasiparticle band structure calculations of ZnO, CdO, and MgO polymorphs. **Physical Review B**, vol. 95, no. 4, p. 045126, jan 2017. ISSN 2469-9950.

BARRETT, S. D.; KOK, P. Efficient high-fidelity quantum computation using matter qubits and linear optics. **arXiv.org**, quant-ph, p. 2–5, 2004. ISSN 1050-2947.

BECHSTEDT, F. **Principles of Surface Physics**. Berlin, Heidelberg: Springer Berlin Heidelberg, 2003. (Advanced Texts in Physics). ISBN 978-3-642-62458-2.

BECKE, A. D. A new mixing of Hartree-Fock and local density-functional theories. **The Journal of Chemical Physics**, vol. 98, no. 2, p. 1372–1377, 1993. ISSN 00219606.

BLOCH, F. Über die Quantenmechanik der Elektronen in Kristallgittern. **Zeitschrift für Physik**, vol. 52, no. 7-8, p. 555–600, 1929. ISSN 14346001.

BLOCH, F. Nuclear induction. **Physical Review**, vol. 70, no. 7-8, p. 460–474, 1946. ISSN 0031899X.

BLOCHL, P. E. Projector augmented-wave method. **Physical Review B**, vol. 50, no. 24, p. 17953–17979, 1994. ISSN 01631829.

BORN, M. The statistical interpretation of quantum mechanics. **Nobel Lecture**, vol. 11, p. 1942–1962, 1954. ISSN 0036-8075.

BOURDET, L.; NIQUET, Y. M. All-electrical manipulation of silicon spin qubits with tunable spin-valley mixing. **Physical Review B**, American Physical Society, vol. 97, no. 15, p. 1–9, 2018. ISSN 24699969.

CAPELLE, K. A bird's-eye view of density-functional theory. **Brazilian Journal of Physics**, vol. 36, no. 4a, p. 1318–1343, dec 2006. ISSN 0103-9733.

CASPERSON, L. W. Rate-equation approximations in high-gain lasers. **Physical Review A**, vol. 55, no. 4, p. 3073–3085, 1997. ISSN 1050-2947.

CHOI, S.; JAIN, M.; LOUIE, S. G. Mechanism for optical initialization of spin in NV - center in diamond. **Physical Review B - Condensed Matter and Materials Physics**, vol. 86, no. 4, p. 1–5, 2012. ISSN 10980121.

CHOU, J.-P.; BODROG, Z.; GALI, A. First-Principles Study of Charge Diffusion between Proximate Solid-State Qubits and Its Implications on Sensor Applications. 2018.

COULSON, C. A.; KEARSLEY, M. J. Colour Centres in Irradiated Diamonds. I. **Proceedings of the Royal Society A: Mathematical, Physical and Engineering Sciences**, vol. 241, no. 1227, p. 433–454, sep 1957. ISSN 1364-5021.

CRIPPA, A.; MAURAND, R.; BOURDET, L.; KOTEKAR-PATIL, D.; AMISSE, A.; JEHL, X.; SANQUER, M.; LAVIÉVILLE, R.; BOHUSLAVSKYI, H.; HUTIN, L.; BARRAUD, S.; VINET, M.; NIQUET, Y. M.; De Franceschi, S. Electrical Spin Driving by g -Matrix Modulation in Spin-Orbit Qubits. **Physical Review Letters**, vol. 120, no. 13, p. 1–5, 2018. ISSN 10797114.

DAVIES, G.; HAMER, M. F. Optical Studies of the 1.945 eV Vibronic Band in Diamond. **Proc. Roy. Soc. Lond. A**, vol. 348, no. 1653, p. 285–298, 1976. ISSN 1364-5021, 1471-2946.

DEUTSCH, D. Quantum Theory, the Church-Turing Principle and the Universal Quantum Computer. **Proceedings of the Royal Society A: Mathematical, Physical and Engineering Sciences**, vol. 400, no. 1818, p. 97–117, jul 1985. ISSN 1364-5021.

DION, M.; RYDBERG, H.; SCHRÖDER, E.; LANGRETH, D. C.; LUNDQVIST, B. I. Van der Waals density functional for general geometries. **Physical Review Letters**, vol. 92, no. 24, p. 22–25, 2004. ISSN 00319007.

DOHERTY, M. W.; MANSON, N. B.; DELANEY, P.; HOLLENBERG, L. C. L. The negatively charged nitrogen-vacancy centre in diamond: The electronic solution. **New Journal of Physics**, vol. 13, 2011. ISSN 13672630.

DOHERTY, M. W.; MANSON, N. B.; DELANEY, P.; JELEZKO, F.; WRACHTRUP, J.; HOLLENBERG, L. C. L. The nitrogen-vacancy colour centre in diamond. **Physics Reports**, vol. 528, no. 1, p. 1–45, 2013. ISSN 03701573.

EINSTEIN, A. Zur quantentheorie der strahlung. **Phys. Z.**, vol. 18, p. 121–128, 1917.

ENGEL, E.; DREIZLER, R. M. **Density Functional Theory**. Berlin, Heidelberg: Springer Berlin Heidelberg, 2011. (Theoretical and Mathematical Physics). ISBN 978-3-642-14089-1.

FERREIRA, L. G.; MARQUES, M.; TELES, L. K. Approximation to density functional theory for the calculation of band gaps of semiconductors. **Physical Review B**, vol. 78, no. 12, p. 125116, 2008. ISSN 1098-0121.

FERREIRA, L. G.; MARQUES, M.; TELES, L. K. Slater half-occupation technique revisited: The LDA-1/2 and GGA-1/2 approaches for atomic ionization energies and band gaps in semiconductors. **AIP Advances**, vol. 1, no. 3, p. 0–11, 2011. ISSN 21583226.

FEYNMAN, R. P. Simulating physics with computers. **International Journal of Theoretical Physics**, vol. 21, no. 6-7, p. 467–488, jun 1982. ISSN 0020-7748.

FOCK, V.; LENINGRAD, V. V. F. Näherungsmethode zur Lösung des quantenmechanischen Mehrkörperproblems. **Zeitschrift für Physik**, vol. 61, no. 1-2, p. 126–148, 1930. ISSN 1434-6001.

FREITAS, F. L.; FURTHMÜLLER, J.; BECHSTEDT, F.; MARQUES, M.; TELES, L. K. Influence of the composition fluctuations and decomposition on the tunable direct gap and oscillator strength of Ge $1-x$ Sn x alloys. **Applied Physics Letters**, vol. 108, no. 9, p. 092101, feb 2016. ISSN 0003-6951.

FREITAS, F. L.; MARQUES, M.; TELES, L. K. First-principles determination of band-to-band electronic transition energies in cubic and hexagonal AlGaInN alloys. **AIP Advances**, vol. 6, no. 8, p. 085308, 2016. ISSN 2158-3226.

GALI, A.; FYTA, M.; KAXIRAS, E. Ab initio supercell calculations on nitrogen-vacancy center in diamond: Electronic structure and hyperfine tensors. **Physical Review B - Condensed Matter and Materials Physics**, vol. 77, no. 15, p. 1–12, 2008. ISSN 10980121.

GALI, A.; JANZÉN, E.; DEÁK, P.; KRESSE, G.; KAXIRAS, E. Theory of Spin-Conserving Excitation of the NV- Center in Diamond. **Physical Review Letters**, vol. 103, no. 18, p. 186404, 2009. ISSN 0031-9007.

GEORGESCU, I.; NORI, F. Quantum technologies: An old new story. **Physics World**, vol. 25, no. 5, p. 16–17, 2012. ISSN 09538585.

GÖRANSSON, C.; OLOVSSON, W.; ABRIKOSOV, I. A. Numerical investigation of the validity of the Slater-Janak transition-state model in metallic systems. **Physical Review B - Condensed Matter and Materials Physics**, vol. 72, no. 13, p. 1–7, 2005. ISSN 10980121.

GORDON, L.; WEBER, J. R.; VARLEY, J. B.; JANOTTI, A.; AWSCHALOM, D. D.; Van de Walle, C. G. Quantum computing with defects. **MRS Bulletin**, vol. 38, no. 10, p. 802–807, oct 2013. ISSN 0883-7694.

GORMAN, J.; HASKO, D. G.; WILLIAMS, D. A. Charge-qubit operation of an isolated double quantum dot. **Physical Review Letters**, vol. 95, no. 9, p. 1–4, 2005. ISSN 00319007.

- GRIFFITHS, D. J. **Introduction to Quantum Mechanics (2nd Edition)**. 2nd. ed. [S.l.]: Pearson Prentice Hall, 2004. ISBN 0131118927.
- HAGELSTEIN, P. L.; SENTURIA, S. D.; ORLANDO, T. P. **Introductory applied quantum and statistical mechanics**. [S.l.]: John Wiley & Sons, 2004.
- HAMDI, S. M.; ZUHORI, S. T.; MAHMUD, F.; PAL, B. A Compare between Shor's quantum factoring algorithm and General Number Field Sieve. In **1st International Conference on Electrical Engineering and Information and Communication Technology, ICEEICT 2014**. [S.l.: s.n.], 2014. p. 1–6. ISBN 9781479948192.
- HARTREE, D. R. The Wave Mechanics of an Atom with a Non-Coulomb Central Field Part I Theory and Methods. **Mathematical Proceedings of the Cambridge Philosophical Society**, vol. 24, no. 1, p. 89–110, 1928. ISSN 14698064.
- HELLMANN, H. A New Approximation Method in the Problem of Many Electrons. **The Journal of Chemical Physics**, vol. 3, no. 1, p. 61–61, 1935. ISSN 00219606. Available from Internet: <<http://aip.scitation.org/doi/10.1063/1.1749559>>.
- HEYD, J.; SCUSERIA, G. E.; ERNZERHOF, M. Hybrid functionals based on a screened Coulomb potential. **Journal of Chemical Physics**, vol. 118, no. 18, p. 8207–8215, 2003. ISSN 00219606.
- HEYD, J.; SCUSERIA, G. E.; ERNZERHOF, M. Erratum: “Hybrid functionals based on a screened Coulomb potential” [J. Chem. Phys. 118, 8207 (2003)]. **The Journal of Chemical Physics**, vol. 124, no. 21, p. 219906, jun 2006. ISSN 0021-9606.
- HIROSE, M.; CAPPELLARO, P. Coherent feedback control of a single qubit in diamond. **Nature**, Nature Publishing Group, vol. 532, no. 7597, p. 77–80, 2016. ISSN 14764687.
- HOHENBERG, P.; KOHN, W. Inhomogeneous Electron Gas. **Physical Review**, vol. 136, no. 3B, p. B864–B871, nov 1964. ISSN 0031-899X.
- HYBERTSEN, M. S.; LOUIE, S. G. First-principles theory of quasiparticles: Calculation of band gaps in semiconductors and insulators. **Physical Review Letters**, vol. 55, no. 13, p. 1418–1421, 1985. ISSN 00319007.
- JANAK, J. Proof that $dE/dn_i = e_i$ in density-functional theory. **Physical Review B**, vol. 18, no. 2, p. 7165–7168, 1978. ISSN 0163-1829.
- KHORASANI, S.; KOOTTANDAVIDA, A. Nonlinear Graphene Quantum Capacitors for Electro-optics. **npj 2D Materials and Applications**, Springer US, no. November 2016, p. 1–6, 2016. ISSN 2397-7132.
- KLIME, J.; BOWLER, D. R.; MICHAELIDES, A. Van der Waals density functionals applied to solids. **Physical Review B - Condensed Matter and Materials Physics**, vol. 83, no. 19, p. 1–13, 2011. ISSN 10980121.
- KODA, D. S.; BECHSTEDT, F.; MARQUES, M.; TELES, L. K. Coincidence Lattices of 2D Crystals: Heterostructure Predictions and Applications. **The Journal of Physical Chemistry C**, vol. 120, no. 20, p. 10895–10908, may 2016. ISSN 1932-7447.

KODA, D. S.; BECHSTEDT, F.; MARQUES, M.; TELES, L. K. Tuning Electronic Properties and Band Alignments of Phosphorene Combined with MoSe₂ and WSe₂. **Journal of Physical Chemistry C**, vol. 121, no. 7, p. 3862–3869, 2017. ISSN 19327455.

KODA, D. S.; BECHSTEDT, F.; MARQUES, M.; TELES, L. K. Trends on band alignments: Validity of Anderson's rule in SnS₂ - and SnSe₂-based van der Waals heterostructures. **Physical Review B**, American Physical Society, vol. 97, no. 16, p. 165402, apr 2018. ISSN 2469-9950.

KOEHL, W. F.; SEO, H.; GALLI, G.; AWSCHALOM, D. D. Designing defect spins for wafer-scale quantum technologies. **MRS Bulletin**, vol. 40, no. 12, p. 1146–1153, 2015. ISSN 0883-7694.

KOHN, W.; SHAM, L. J. Self-Consistent Equations Including Exchange and Correlation Effects. **Physical Review**, vol. 140, no. 4A, p. A1133–A1138, nov 1965. ISSN 0031-899X.

KRESSE, G.; FURTHMÜLLER, J. Efficiency of ab-initio total energy calculations for metals and semiconductors using a plane-wave basis set. **Computational Materials Science**, vol. 6, no. 1, p. 15–50, 1996. ISSN 09270256.

KRESSE, G.; FURTHMÜLLER, J. Efficient iterative schemes for ab initio total-energy calculations using a plane-wave basis set. **Physical Review B**, vol. 54, no. 16, p. 11169–11186, 1996. ISSN 0163-1829.

KRESSE, G.; JOUBERT, D. From ultrasoft pseudopotentials to the projector augmented-wave method. **Physical Review B**, vol. 59, no. 3, p. 1758–1775, jan 1999. ISSN 0163-1829.

KRUPIN, O. **Dichroism and Rashba effect at magnetic crystal surfaces of rare-earth metals**. 79–84 p. Tese (Doctoral dissertation) — Freie Universität Berlin, 2004.

LAMB, W. E. Theory of an Optical Maser. **Physical Review**, vol. 134, no. 6A, p. A1429–A1450, jun 1964. ISSN 0031-899X.

LAUCHT, A.; KALRA, R.; SIMMONS, S.; DEHOLLAIN, J. P.; MUHONEN, J. T.; MOHIYADDIN, F. A.; FREER, S.; HUDSON, F. E.; ITOH, K. M.; JAMIESON, D. N.; MCCALLUM, J. C.; DZURAK, A. S.; MORELLO, A. A dressed spin qubit in silicon. **Nature Nanotechnology**, Nature Publishing Group, vol. 12, no. 1, p. 61–66, oct 2016. ISSN 1748-3387.

LEITE, J. R.; FERREIRA, L. G. Effects of the Coulomb correlation on the calculated results for atoms with and without spin polarization. **Physical Review A**, vol. 3, no. 4, p. 1224–1230, 1971. ISSN 10502947.

LENEF, A.; RAND, S. C. Electronic structure of the N-V center in diamond: Theory. **Physical Review B**, vol. 53, no. 20, p. 13441–13455, 1996. ISSN 0163-1829.

LUCATTO, B.; ASSALI, L. V. C.; PELA, R. R.; MARQUES, M.; TELES, L. K. General procedure for the calculation of accurate defect excitation energies from

- DFT-1/2 band structures: The case of the NV- center in diamond. **Physical Review B**, vol. 96, no. 7, p. 075145, aug 2017. ISSN 2469-9950.
- MANSON, N. B.; HARRISON, J. P.; SELLARS, M. J. Nitrogen-vacancy center in diamond: Model of the electronic structure and associated dynamics. **Physical Review B - Condensed Matter and Materials Physics**, vol. 74, no. 10, p. 1–11, 2006. ISSN 10980121.
- MATUSALEM, F.; PELÁ, R. R.; MARQUES, M.; TELES, L. K. Charge transition levels of Mn-doped Si calculated with the GGA-1/2 method. **Physical Review B**, vol. 90, no. 22, p. 224102, dec 2014. ISSN 1098-0121.
- MATUSALEM, F.; Ribeiro, Jr., M.; MARQUES, M.; PELÁ, R. R.; FERREIRA, L. G.; TELES, L. K. Combined LDA and LDA-1/2 method to obtain defect formation energies in large silicon supercells. **Physical Review B**, vol. 88, no. 22, p. 224102, dec 2013. ISSN 1098-0121.
- MOMMA, K.; IZUMI, F. VESTA 3 for three-dimensional visualization of crystal, volumetric and morphology data. **Journal of Applied Crystallography**, International Union of Crystallography, vol. 44, no. 6, p. 1272–1276, 2011. ISSN 00218898.
- MONKHORST, H. J.; PACK, J. D. Special points for Brillouin-zone integrations. **Physical Review B**, vol. 13, no. 12, p. 5188–5192, jun 1976. ISSN 0556-2805.
- NOVOSELOV, K. S.; MISHCHENKO, A.; CARVALHO, A.; Castro Neto, A. H. 2D materials and van der Waals heterostructures. **Science**, vol. 353, no. 6298, 2016. ISSN 10959203.
- O'BRIEN, J. L.; PRYDE, G. J.; WHITE, A. G.; RALPH, T. C.; BRANNING, D. Demonstration of an all-optical quantum controlled-NOT gate. **Nature**, vol. 426, no. 6964, p. 264–267, 2003. ISSN 0028-0836.
- PAIER, J.; MARSMAN, M.; HUMMER, K.; KRESSE, G.; GERBER, I. C.; ANGYÁN, J. G. Screened hybrid density functionals applied to solids. **Journal of Chemical Physics**, vol. 124, no. 15, 2006. ISSN 00219606.
- PAWŁOWSKI, J.; ZEBROWSKI, D.; BEDNAREK, S. Valley qubit in a gated MoS₂monolayer quantum dot. **Physical Review B**, vol. 97, no. 15, p. 1–12, 2018. ISSN 24699969.
- PELA, R. R.; MARQUES, M.; TELES, L. K. Comparing LDA-1/2, HSE03, HSE06 and G 0 W 0 approaches for band gap calculations of alloys. **Journal of Physics: Condensed Matter**, IOP Publishing, vol. 27, no. 50, p. 505502, dec 2015. ISSN 0953-8984.
- PERDEW, J. P.; BURKE, K.; ERNZERHOF, M. Generalized Gradient Approximation Made Simple. **Physical Review Letters**, vol. 77, no. 18, p. 3865–3868, 1996. ISSN 0031-9007.
- PERDEW, J. P.; ERNZERHOF, M.; BURKE, K. Rationale for mixing exact exchange with density functional approximations. **Journal of Chemical Physics**, vol. 105, no. 22, p. 9982–9985, 1996. ISSN 00219606.

- PERDEW, J. P.; LEVY, M. Physical content of the exact kohn-sham orbital energies: Band gaps and derivative discontinuities. **Physical Review Letters**, vol. 51, no. 20, p. 1884–1887, 1983. ISSN 00319007.
- PERDEW, J. P.; YANG, W.; BURKE, K.; YANG, Z.; GROSS, E. K. U.; SCHEFFLER, M.; SCUSERIA, G. E.; HENDERSON, T. M.; ZHANG, I. Y.; RUZSINSZKY, A.; PENG, H.; SUN, J.; TRUSHIN, E.; GÖRLING, A. Understanding band gaps of solids in generalized Kohn–Sham theory. **Proceedings of the National Academy of Sciences**, vol. 114, no. 11, p. 2801–2806, 2017. ISSN 0027-8424.
- PSEUDOPOTENTIALS. 2014. Available from Internet: <<http://bohr.inesc-mn.pt/~jlm/pseudo.html>>. Cited November 2017.
- RINKE, P.; JANOTTI, A.; SCHEFFLER, M.; Van De Walle, C. G. Defect formation energies without the band-gap problem: Combining density-functional theory and the GW approach for the silicon self-interstitial. **Physical Review Letters**, vol. 102, no. 2, p. 1–4, 2009. ISSN 00319007.
- ROBLEDO, L.; BERNIEN, H.; SAR, T. V. D.; HANSON, R. Spin dynamics in the optical cycle of single nitrogen-vacancy centres in diamond. **New Journal of Physics**, vol. 13, 2011. ISSN 13672630.
- ROY, T.; TOSUN, M.; HETTICK, M.; AHN, G. H.; HU, C.; JAVEY, A. 2D-2D tunneling field-effect transistors using WSe₂/SnSe₂ heterostructures. **Applied Physics Letters**, vol. 108, no. 8, p. 083111, 2016. ISSN 0003-6951.
- SCHNEIDER, P. I.; SAENZ, A. Quantum computation with ultracold atoms in a driven optical lattice. **Physical Review A - Atomic, Molecular, and Optical Physics**, vol. 85, no. 5, p. 1–5, 2012. ISSN 10502947.
- SCHUMACHER, B. Quantum coding. **Physical Review A**, vol. 51, no. 4, p. 2738–2747, 1995. ISSN 10502947.
- SHAM, L. J.; SCHLÜTER, M. Density-functional theory of the band gap. **Physical Review B**, vol. 32, no. 6, p. 3883–3889, sep 1985. ISSN 0163-1829.
- SHOR, P. W. Polynomial-Time Algorithms for Prime Factorization and Discrete Logarithms on a Quantum Computer *. **SIAM Journal on Computing**, vol. 26, no. 5, p. 1484–1509, 1997. ISSN 0097-5397.
- SLATER, J. C.; JOHNSON, K. H. Self-consistent-field Xa cluster method for polyatomic molecules and solids. **Physical Review B**, vol. 5, no. 3, p. 844–853, 1972. ISSN 01631829.
- STRUCK, P. R.; BURKARD, G. Spin Quantum Computing. In **Handbook of Spintronics**. [S.l.: s.n.], 2016. p. 71–103.
- TU, Y.; TANG, Z.; ZHAO, X. G.; CHEN, Y.; ZHU, Z. Q.; CHU, J. H.; FANG, J. C. A paramagnetic neutral VAION center in wurtzite AlN for spin qubit application. **Applied Physics Letters**, vol. 103, no. 7, 2013. ISSN 00036951.

VANDERBILT, D. Soft self-consistent pseudopotentials in a generalized eigenvalue formalism. **Physical Review B**, vol. 41, no. 11, p. 7892–7895, apr 1990. ISSN 0163-1829.

WANG, L. J.; ZOU, K. H.; SUN, W.; MAO, Y.; ZHU, Y. X.; YIN, H. L.; CHEN, Q.; ZHAO, Y.; ZHANG, F.; CHEN, T. Y.; PAN, J. W. Long-distance copropagation of quantum key distribution and terabit classical optical data channels. **Physical Review A - Atomic, Molecular, and Optical Physics**, vol. 95, no. 1, p. 1–8, 2017. ISSN 10941622.

WANG, X.; ZHAO, M.; WANG, Z.; HE, X.; XI, Y.; YAN, S. Spin-polarization of V GaO N center in GaN and its application in spin qubit. **Applied Physics Letters**, vol. 100, no. 19, p. 1–5, 2012. ISSN 00036951.

WANG, Y.; DOLDE, F.; BIAMONTE, J.; BABBUSH, R.; BERGHOLM, V.; YANG, S.; JAKOBI, I.; NEUMANN, P.; ASPURU-GUZI, A.; WHITFIELD, J. D.; WRACHTRUP, J. Quantum Simulation of Helium Hydride in a Solid-State Spin Register. no. 8, p. 7769–7774, 2014. ISSN 1936-0851.

WEBER, J. R.; KOEHL, W. F.; VARLEY, J. B.; JANOTTI, A.; BUCKLEY, B. B.; Van de Walle, C. G.; AWSCHALOM, D. D. Quantum computing with defects. **Proceedings of the National Academy of Sciences of the United States of America**, vol. 107, no. 19, p. 8513–8, 2010. ISSN 1091-6490.

WIDMANN, M.; LEE, S.-Y.; RENDLER, T.; SON, N. T.; FEDDER, H.; PAIK, S.; YANG, L.-P.; ZHAO, N.; YANG, S.; BOOKER, I.; DENISENKO, A.; JAMALI, M.; MOMENZADEH, S. A.; GERHARDT, I.; OHSHIMA, T.; GALI, A.; JANZÉN, E.; WRACHTRUP, J. Coherent control of single spins in silicon carbide at room temperature. **Nature Materials**, vol. 14, no. 2, p. 164–168, 2014. ISSN 1476-1122. Available from Internet: <<http://www.nature.com/doi/10.1038/nmat4145>>.

WORT, C. J. H.; BALMER, R. S. Diamond as an electronic material. **Materials Today**, Elsevier Ltd, vol. 11, no. 1-2, p. 22–28, 2008. ISSN 13697021.

Appendix A - Formulation of the dihydrogen cation toy model

Under the Born-Oppenheimer approximation, assuming that the atomic nuclei are fixed in position, with a specified distance R apart, the Hamiltonian for the electron is

$$H = -\frac{\hbar^2}{2m}\nabla^2 - \frac{e^2}{4\pi\epsilon_0}\left(\frac{1}{r_1} + \frac{1}{r_2}\right) + eFz = -\frac{\hbar^2}{2m}\nabla^2 + 2a_0E_0\left(\frac{1}{r_1} + \frac{1}{r_2}\right) + eFz \quad (\text{A.1})$$

assuming S.I. units and where a_0 is the Bohr radius, E_0 is the ground state energy of the hydrogen atom, and $r_1 = |\mathbf{r}_1|$ and $r_2 = |\mathbf{r}_2|$ are the distances to the electron from the respective protons.

Using the simplest LCAO approximation, we will consider the electron's wavefunction to be a linear combination between the wavefunction of the ground state of the electron in a hydrogen atom, $\psi_0(r)$, centered in each nucleus. The ground state wavefunction of a

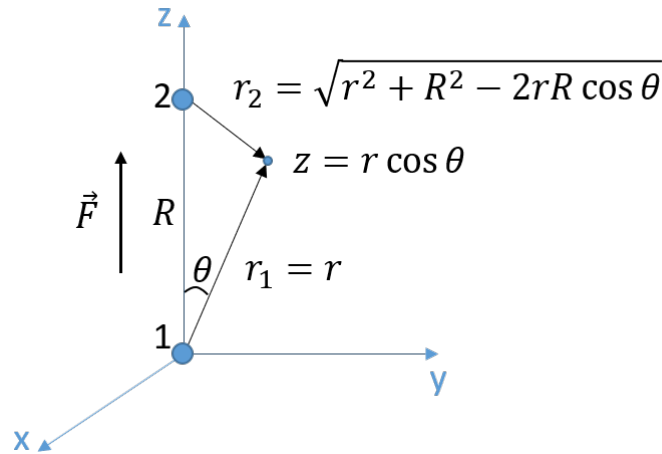


FIGURE A.1 – Coordinates for the mathematical formulation of the dihydrogen cation system.

hydrogen atom is (GRIFFITHS, 2004)

$$\psi_0(r) = \frac{e^{-r/a_0}}{\sqrt{\pi a_0^3}}. \quad (\text{A.2})$$

Thus, our wavefunction can be written as

$$\psi(r) = \alpha\psi_0(r_1) + \beta\psi_0(r_2) = A[\psi_0(r_1) + \lambda\psi_0(r_2)], \quad (\text{A.3})$$

where α and β are the mixing coefficients, A is the normalization constant, which we can choose to be a real number due to the non-observability of a global phase of the state, and λ is a complex number.

In order to normalize the wavefunction, we calculate

$$1 = A^2 \left[\int d^3r |\psi_0(r_1)|^2 + |\lambda|^2 \int d^3r |\psi_0(r_2)|^2 + 2\text{Re}(\lambda) \int d^3r \psi_0(r_1)\psi_0(r_2) \right], \quad (\text{A.4})$$

where $\text{Re}(\lambda)$ stands for the real part of λ . The first two integrals are 1, since ψ_0 itself is normalized. The third is known as the overlap integral, and results in (GRIFFITHS, 2004)

$$I = \langle 1|2 \rangle = e^{-R/a_0} \left[1 + \left(\frac{R}{a_0} \right) + \frac{1}{3} \left(\frac{R}{a_0} \right)^2 \right], \quad (\text{A.5})$$

where we adopted $|1\rangle = |\psi_0(r_1)\rangle$ and $|2\rangle = |\psi_0(r_2)\rangle$, for shortness. Therefore, in terms of I , the square of the normalization factor A is

$$A^2 = \frac{1}{1 + |\lambda|^2 + 2\text{Re}(\lambda)I}. \quad (\text{A.6})$$

The expectation value of the energy $\langle H \rangle$ is given by

$$\begin{aligned} \langle H \rangle &= [A(\langle 1| + \lambda^* \langle 2|)] H [A(|1\rangle + \lambda|2\rangle)] \\ &= A^2(\langle 1|H|1\rangle + |\lambda|^2 \langle 2|H|2\rangle + 2\text{Re}(\lambda) \langle 0|H|1\rangle). \end{aligned} \quad (\text{A.7})$$

Writing $H = T + U_1 + U_2 + eFz$, where $T = -(\hbar^2/2m)\nabla^2$ is the kinetic energy operator, $U_1 = (2a_0E_0)(1/r_1)$ is the coulombic potential of nucleus 1, and $U_2 = (2a_0E_0)(1/r_2)$ is the coulombic potential of nucleus 2, we can simplify the terms in Eq. A.7.

- The first term is given by

$$\langle 1|H|1\rangle = \langle 1|T + U_1|1\rangle + \langle 1|U_2|1\rangle + eF \langle 1|z|1\rangle = E_0 + 2a_0E_0 \left\langle 1 \left| \frac{1}{r_1} \right| 1 \right\rangle,$$

where we used the fact that the expectation value of z in the wavefunction 1 is zero.

Defining $D = a_0 \langle 1 | 1/r_1 | 1 \rangle$ (the so-called direct integral), we write

$$\langle 1 | H | 1 \rangle = E_0 + 2E_0 D, \quad (\text{A.8})$$

•The second term is given by

$$\langle 2 | H | 2 \rangle = \langle 2 | T + U_2 | 2 \rangle + \langle 2 | U_1 | 2 \rangle + eF \langle 2 | z | 2 \rangle = E_0 + 2a_0 E_0 \left\langle 2 \left| \frac{1}{r_2} \right| 2 \right\rangle + eFR,$$

where we used the fact that the expectation value of z in the wavefunction 2 is R . Since $a_0 \langle 2 | 1/r_2 | 2 \rangle = a_0 \langle 1 | 1/r_1 | 1 \rangle = D$, we write

$$\langle 2 | H | 2 \rangle = E_0 + 2E_0 D + eFR, \quad (\text{A.9})$$

•The third and last term is given by

$$\begin{aligned} \langle 1 | H | 2 \rangle &= \langle 1 | T + U_2 | 2 \rangle + \langle 1 | U_1 | 2 \rangle + eF \langle 1 | z | 2 \rangle \\ &= E_0 \langle 1 | 2 \rangle + 2a_0 E_0 \left\langle 1 \left| \frac{1}{r_1} \right| 2 \right\rangle + eF \langle 1 | z | 2 \rangle, \end{aligned}$$

Defining $Z_X = \langle 1 | z | 2 \rangle$, $X = a_0 \langle 1 | 1/r_1 | 1 \rangle$ (the so-called exchange integral), and recalling that $\langle 1 | 2 \rangle = I$, we write

$$\langle 1 | H | 2 \rangle = E_0 I + 2E_0 X + Z_X. \quad (\text{A.10})$$

The results for the direct and exchange integrals are the same as in the case of no electric field, which are (GRIFFITHS, 2004)

$$D = \frac{a_0}{R} - \left(1 + \frac{a_0}{R}\right) e^{-2R/a_0}, \quad (\text{A.11})$$

and

$$X = \left(1 + \frac{R}{a_0}\right) e^{-R/a_0}. \quad (\text{A.12})$$

Finally, we must calculate Z_X .

$$\begin{aligned} Z_X &= \int d^3 r \psi_0(r_1) z \psi_0(r_2) = \frac{1}{\pi a_0^3} \int d^3 r e^{-r_1/a_0} e^{-r_2/a_0} r_1 \cos \theta \\ &= \frac{1}{\pi a_0^3} \int \int \int e^{-r/a_0} e^{-(\sqrt{r^2+R^2-2rR\cos\theta})/a_0} r^3 \cos \theta \sin \theta dr d\theta d\phi \\ &= \frac{2}{a_0^3} \int \int e^{-r/a_0} e^{-(\sqrt{r^2+R^2-2rR\cos\theta})/a_0} r^3 \cos \theta \sin \theta dr d\theta \end{aligned} \quad (\text{A.13})$$

Let $y = \sqrt{r^2 + R^2 - 2rR \cos \theta}$, so that $d(y^2) = 2y dy = 2rR \sin \theta d\theta$. Using also that

$\cos \theta = (r^2 + R^2 - y^2)/(2rR)$, we have

$$\begin{aligned} Z_X &= \frac{1}{R^2 a_0^3} \int_0^\infty r e^{-r/a_0} \left[\int_{|r-R|}^{r+R} e^{-y/a_0} y (R^2 + r^2 - y^2) dy \right] dr \\ &= \frac{1}{R^2 a_0^3} \int_0^\infty r e^{-r/a_0} \left[(R^2 + r^2) \int_{|r-R|}^{r+R} y e^{-y/a_0} dy - \int_{|r-R|}^{r+R} y^3 e^{-y/a_0} dy \right] dr \end{aligned} \quad (\text{A.14})$$

Evaluating this integral, we obtain

$$Z_X = \frac{R}{2} e^{-R/a_0} \left[1 + \left(\frac{R}{a_0} \right) + \frac{1}{3} \left(\frac{R}{a_0} \right)^2 \right] = \frac{R}{2} I. \quad (\text{A.15})$$

Putting all this together, Eq. A.7 becomes

$$\langle H \rangle = E_0 + \frac{(D + 2X \operatorname{Re}(\lambda) + D|\lambda|^2) 2E_0 + (\operatorname{Re}(\lambda)I + |\lambda|^2) eFR}{1 + |\lambda|^2 + 2\operatorname{Re}(\lambda)I} \quad (\text{A.16})$$

Assuming that the nuclei are fixed in space, as is the case of quantum dots or the vdW heterostructure on a substrate, we take the partial derivative of the expectation value of the Hamiltonian with respect to λ^* , the complex conjugate of λ , to find the maximum and minimum points as functions of the electric field. This yields

$$\begin{aligned} \lambda_{max} &= \frac{-eFR - \sqrt{(eFR)^2(1 - I^2) + (4(DI - X)E_0)^2}}{eFIR + 4(DI - X)E_0} \\ \lambda_{min} &= \frac{-eFR + \sqrt{(eFR)^2(1 - I^2) + (4(DI - X)E_0)^2}}{eFIR + 4(DI - X)E_0}, \end{aligned} \quad (\text{A.17})$$

which are always real. Therefore, we may write the total energy of the system as a function of the electric field by adding the energy of the nucleus-nucleus repulsion and the energy of the nuclei in the electric field to $\langle H \rangle|_{\lambda_{min}}$, which gives

$$\begin{aligned} E_{tot} &= \langle H \rangle - \frac{2a_0 E_0}{R} - eFR \\ E_{tot} &= \left(1 - 2\frac{a_0}{R} \right) E_0 + \frac{(D + 2X\lambda_{min} + D\lambda_{min}^2) 2E_0 - (I\lambda_{min} + 1) eFR}{1 + \lambda_{min}^2 + 2I\lambda_{min}}. \end{aligned} \quad (\text{A.18})$$

The probabilities of finding the electron in atom 1 or in atom 2 are given, respectively, by

$$\begin{aligned} p_1 &= |\langle 1|\psi \rangle|^2 = |\alpha + \beta I|^2 = \frac{(1 + I\lambda_{min})^2}{1 + \lambda_{min}^2 + 2I\lambda_{min}} \\ p_2 &= |\langle 2|\psi \rangle|^2 = |\alpha I + \beta|^2 = \frac{(I + \lambda_{min})^2}{1 + \lambda_{min}^2 + 2I\lambda_{min}} \end{aligned} \quad (\text{A.19})$$

Appendix B - Publications in periodicals

Until the present moment, we have one paper (directly related to this work) published in an international periodical. It is:

LUCATTO, B.; ASSALI, L. V. C.; PELA, R. R.; MARQUES, M.; TELES, L. K. General procedure for the calculation of accurate defect excitation energies from DFT-1/2 band structures: The case of the NV^- center in diamond. **Physical Review B**, vol. 96, no. 7, p. 75145, aug. 2017. ISSN 2469-9950.

Appendix C - Presentations at conferences

Several results of this work have already been presented at national conferences. We list them (the presenter's name is underlined).

1. LUCATTO, B.; ASSALI, L. V. C.; PELA, R. R.; MARQUES, M.; TELES, L. K. Obtaining accurate defect excitation energies from DFT-1/2 band structures. XL Encontro Nacional de Física da Matéria Condensada, Aug. 27-31, 2017 (XL ENFMC)- Búzios, RJ, Brazil. Oral presentation.
2. LUCATTO, B.; ASSALI, L. V. C.; PELA, R. R.; MARQUES, M.; TELES, L. K. Accurate deep centers' optical transition energies from DFT-1/2 band structures. 18th Brazilian Workshop on Semiconductor Physics (BWSP-2017), Aug. 14-18, 2017 - Mareias, São Paulo, Brazil. Panel presentation.

Annex A - Published papers

Accurate defect excitation energies from DFT-1/2 band structures: the NV⁻ center in diamond

Bruno Lucatto,^{1,*} Lucy V. C. Assali,² Ronaldo Rodrigues Pela,¹ Marcelo Marques,¹ and Lara K. Teles¹

¹*Grupo de Materiais Semicondutores e Nanotecnologia (GMSN),*

Technological Institute of Aeronautics (ITA), 12228-900 São José dos Campos, SP, Brazil

²*Institute of Physics, University de São Paulo (USP), 05315-970 São Paulo, SP, Brazil*

(Dated: May 29, 2017)

A major challenge in creating a quantum computer is to find a quantum system that can be used to implement the qubits. For this purpose, deep centers are prominent candidates, and *ab initio* calculations are one of the most important tools to theoretically study their properties. However, these calculations are highly involved, due to the large supercell needed, and the computational cost can be even larger when one goes beyond the Kohn-Sham scheme to correct the band gap problem and achieve good accuracy. In this work, we present a method that overcomes these problems and provides the optical transition energies as a difference of Kohn-Sham eigenvalues; and even more, provides a complete and accurate band structure of the defect in the semiconductor. The method is an extension of the low-cost and parameter-free DFT-1/2 approximate quasi-particle correction, and allows it to be applied in the study of complex defects. As a benchmark, we apply the method to the NV⁻ center in diamond. The agreement with experiments is remarkable, with an accuracy of 0.1 eV. The band structure agrees with the expected qualitative features of this system, and thus provides a good intuitive physical picture by itself.

I. INTRODUCTION

One of the most exciting engineering problems of current days is to develop a quantum computer. A quantum computer is a computation system that makes direct use of quantum phenomena, such as entanglement and superposition, to perform operations on data. Their fundamental building blocks are called qubits, in analogy to the bits present in digital computers. Quantum computers could enable us to solve complex and time-demanding problems in a much faster way. This performance difference is not due to an eventual faster clock speed, but due to the different kind of operations that quantum computers will be able to perform with the data stored in qubits.¹

A major challenge in creating a quantum computer is to find a quantum system that could be used to implement the qubits. Most systems interact strongly with their surroundings, causing decoherence and consequently loss of information. In this scenario, deep centers are prominent.² They are point defects in a semiconductor or insulating crystal that bind electrons to a localized region. Consequently, most characteristics of their electronic states resembles the ones of single atoms or molecules. Additionally, deep centers are fixed in space by the surrounding crystal, in contrast to some other proposals that require additional systems, like the magneto-optical traps for ultracold atoms.

A deep center in diamond, known as negatively charged nitrogen-vacancy center (NV⁻ center),³ has been strongly considered for such applications, since it has many desirable characteristics: its spin can be optically polarized, manipulated with microwaves, optically measured in an on-demand fashion at the single defect level, and also have a huge coherence time, achieving the order

of milliseconds.⁴

Although NV⁻ centers in diamond have all the desirable characteristics for a qubit, diamond as a host is not ideal, since it makes device construction and design with current technology really challenging due to its high mechanical resistance and small chemical reactivity.⁴ Therefore, it is desirable to find deep centers with NV-like properties in semiconductor hosts that are more technologically mature, and a systematic search has been initiated.⁵

To predict theoretically whether a system is suitable to implement a qubit, first principles calculations based on density functional theory (DFT) are often used. However, in order to achieve enough accuracy, the calculations are usually highly involved because one needs to use a large supercell and one must go beyond the Kohn-Sham scheme to better describe it, due to the underestimation of the quasi-particle band gap in standard DFT calculations. Hence, it is desirable to develop a fast method that can be employed on this systematic search for NV⁻ like systems. A good choice is the LDA-1/2 (*LDA minus half*), developed by Ferreira, Marques and Teles,^{6,7} which introduces approximate quasi-particle corrections and has accurate predictions, while keeping the same computational cost of the standard LDA approach. The method also works with the more modern GGA functionals, in which case it is called GGA-1/2. Hence, to avoid unnecessary particularization, we call it DFT-1/2.

In this paper, we extend the DFT-1/2 method to calculate the optical transition energies between the defect levels. We demonstrate that it is possible to determine the optical transition energies directly from the Kohn-Sham band structure, against the usual procedure of taking the difference between two total-energy calculations. Our proposal is benchmarked by applying it to the NV⁻ center in diamond, whose transition energies have already

been experimentally determined. The method allows for a systematic search for deep centers, since it has as a final result a complete band structure which we can use to accurately analyze the system both qualitatively and quantitatively. Moreover, despite the specific nature of its initial motivation, this method is a general procedure, and can be used to study any system with optical transition energies between levels within the band gap.

II. RETROSPECT FOR THE NV⁻ CENTER IN DIAMOND

Point defects are usually stable in different charge configurations, depending on the Fermi level position. The NV center has two different charge configurations, NV⁰ and NV⁻, and only the latter has the desired properties to be used as a qubit.³ Fortunately, nitrogen doping places the Fermi level inside the range where the negatively charged defect is stable.⁸

The NV center consists in a substitutional nitrogen atom adjacent to a carbon vacancy, presenting a C_{3v} point symmetry. An instructive and useful model is to consider the defect as an effective molecule.^{9,10} This approach, known as “molecular model for defects” consists in making symmetry adapted linear combinations of the dangling bonds around the vacancy to construct molecular orbitals. It has the implicit assumption that the electrons bound to the defect are localized around it and are not “spilling over” from the vacancy into the entire crystal.^{9,11} The states are labeled using the Mulliken symbols. Lower case letters indicate the single-particle states, while capital letters label the many-body states.

Since each dangling bond from the three carbon atoms surrounding the vacancy contributes with one electron,

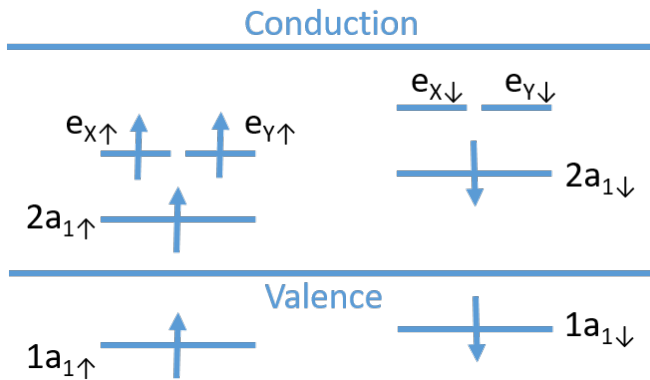


FIG. 1. (color online) Schematic representation of the defect states and their occupation on the ground state of the NV⁻ center in diamond. Spin up levels are on the left of the figure, while spin down levels are on the right. There are two distinct levels with a_1 geometry, which are labeled in crescent order of energy with a number on the left. The double-degenerate level e is indicated with a broken line.

and the overlapping nitrogen lone pair has other two electrons, we conclude that the neutral NV center would have five electrons and, consequently, the NV⁻ would have six, which would be accommodated in the defect energy levels.

We note that the defect has states within the band gap that are spin dependent, a consequence of the fact that this defect breaks the spatial inversion symmetry of the crystal. The electronic occupation for the ground state of the NV⁻ center is shown in Fig. 1. It can be obtained by filling the lowest energy states with the corresponding spin state (spin up on the left side, spin down on the right side). This leaves us with four spin-up and two spin-down electrons, hence the spins in the ground state do not cancel out and we have a total effective spin $S = 1$, *i.e.* the ground state is a triplet. This fact is of central importance in the application of the NV⁻ center as a qubit, since it is the spin that is used to store the quantum information.

When electromagnetic radiation of 2.18 eV (569 nm, green light) is applied,¹² as depicted in Fig 2, there is a resonant excitation to the first excited state. This can be understood in light of Fig. 1 as promoting the spin down electron in the state $2a_{1\downarrow}$ to one of the excited states $e_{x\downarrow}$ or $e_{y\downarrow}$. Note that this is the first possible optical excitation of the system, since changes in spin are forbidden at the first order. Another important fact concerning this transition is that it is possible to excite the system without exciting electrons neither from the valence band to the defect nor from the defect to the conduction band, because the defect levels are far apart from the Valence Band Maximum (VBM) and the Conduction Band Minimum (CBM). If the levels were shallower, it would be possible to excite electrons into or outside the defect levels, what would compromise its operation as a qubit.

Considering the multi-electronic system, both the ground state and the excited state are triplets. However, the excited state transforms as the E symmetry representation, in contrast with the ground state, which transforms as A₂. This difference in symmetry of the wave function impacts the geometry of the defect. After a transition, the structure relaxes to the new equilibrium geometry, and since the movement of the ions is orders of magnitude slower than the electronic excitation, it is a good approximation to consider that the absorption and emission corresponds to vertical transitions (Fig 2). The photon emission then occurs in the geometry of the excited state, and the difference in energy between the excited state and the ground state in this configuration is 1.76 eV (704 nm, red light).¹² The difference in energy between the excited and ground states in their respective relaxed geometries is called the Zero Phonon Line (ZPL), and is also indicated in Fig 2. This considerable difference in the wavelength enables to easily separate the photons of the pumping laser from the photons emitted by the center by using a dichroic mirror (which reflects one wavelength and transmits the other), as in confocal microscopy.

It is important to mention that the DFT approach and the defect molecular model are complementary to each other. These two theoretical methods have their complementary strengths and weaknesses, and only their combined application can give us a good picture of the observed phenomena.³

III. THE DFT-1/2 LOCAL CORRECTION TO DEFECT LEVELS

The most important tools to support the search for suitable deep centers for quantum computing applications are the *ab initio* computational techniques based on DFT, since they allow us to determine macroscopic properties based only on the system's atomic composition and approximate geometry. Many attempts have been made to find such defects to find such kind of defects in several semiconductors, as in some silicon-

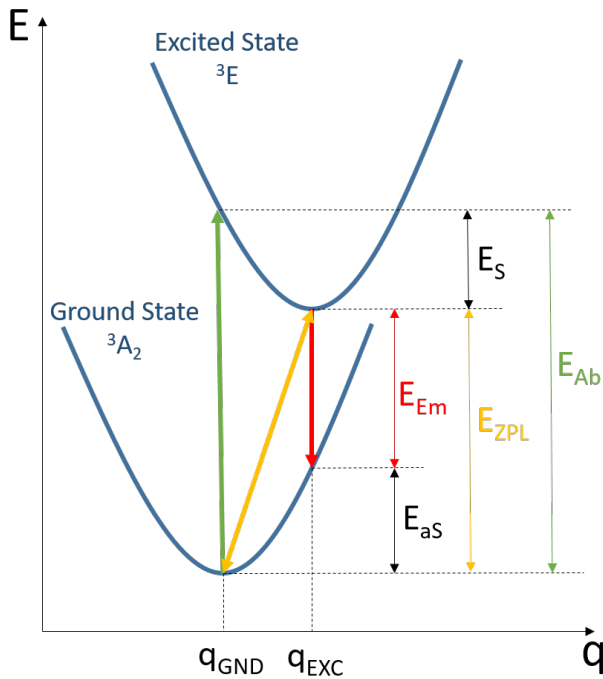


FIG. 2. (color online) Schematic configuration coordinate diagram for the NV⁻ center. The curves represent the energy of the defect as a function of the displacement of the atoms, measured by a generalized coordinate q , for both its many-body electronic ground and excited states. The minima of these curves correspond to the relaxed geometry of each case. The vertical transitions (green and red arrows) correspond to the peaks in the optical absorption and emission curves, respectively. The transition between the minima is called the zero-phonon line (ZPL), and is the same for both the emission and absorption. The Stokes (E_S) and anti-Stokes (E_{aS}) shift energies are also indicated.³

carbide polytypes,^{4,8} wurtzite aluminum nitride¹³ and zinc-blende gallium nitride.¹⁴

Two major concerns can make first-principle calculations of defects a difficult task. First, the usually employed periodic boundary conditions to study solids require a large supercell to minimize the interaction between the defect and its images. Second, the Kohn-Sham band gap is underestimated when compared to experiments,^{15,16} which also impairs reliable calculations of defect levels above the valence band.¹⁷ The method which correct Kohn-Sham eigenvalues, such as hybrid functionals^{18,19} and the *GW* approach,²⁰ usually raise the computational cost.²¹ The DFT-1/2 method is a good alternative due to its nice accuracy and low computational cost.

LDA-1/2 and GGA-1/2 have already been successfully used to study point defects^{22,23} by applying a formalism developed by Rinke *et al.*¹⁷ In these cases, the interest was to study the defect formation and transition energies, both quantities related to the electronic ground state in several charge states, such that what was changing was the number of electrons binded to the defect as a function of the Fermi level position. In the present case, the charge of the defect is always the same and our interest is to study the energies associated to the optical excitation of an electron between intra-defect energy levels.

The DFT-1/2 method generalizes the Slater's transition state technique for solids, introducing approximate quasi-particle corrections which lead to accurate band gap calculations. The details of the method are given in Refs. 6,7. In this work, we present an overview to contextualize the reader who is not familiar with the method. The approach relies on the Janak's theorem²⁴ and on the approximately linear dependence of the Kohn-Sham eigenvalues with its own occupation. It is possible to use these two facts to show that, in the case of atoms and molecules, the value of the highest occupied eigenvalue with half-ionization is the system ionization energy with a remarkable agreement with experimental data.²⁵

In semiconductors and insulators, the quasi-particle band gap is defined as the energy difference between the ionization energy and the electronic affinity. Thus, this scheme allows us to compute the band gap as the difference between the Kohn-Sham eigenvalues, by introducing a half-hole on the VBM and a half-electron on the CBM.

Since Bloch states are delocalized, they do not accurately describe neither the hole on the valence band nor the electron on the conduction band.⁷ Therefore, instead of changing the occupations of the levels, this contribution in energy is added to the potential of the atoms itself. It is assumed that this potential has the same format of the atomic self-energy potential V_S , which can be simply computed as the difference between the neutral atomic potential and the half-ionized atomic potential.⁶ Considering that the localized hole state will be close to the VBM and the localized electron state will be close to the CBM, we must find which atomic orbitals contribute to each of these levels and in what proportion (the or-

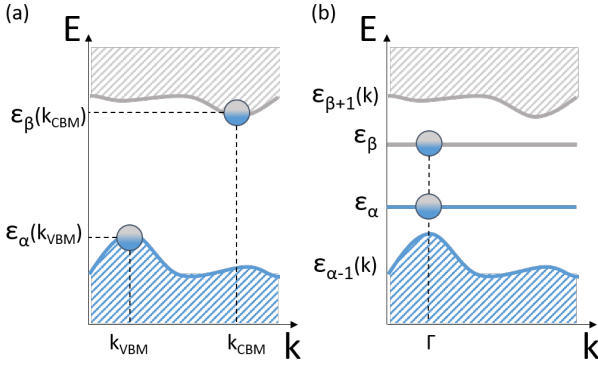


FIG. 3. (color online) (a) Schematic representation of a Kohn-Sham band structure with the Valence Band Maximum and Conduction Band Minimum with half-occupation, as considered on the DFT-1/2 method; and (b) Extension of the DFT-1/2 scheme for defect levels within the band gap.

bital *character* of the levels). This is quantified by the projection of these Kohn-Sham orbitals onto the atomic orbitals. A schematic representation of this scenario is given on Fig. 3(a).

In what follows, we describe an extension of the method for defect levels, which resembles in many aspects the scheme for the bulk (Fig. 3(b)). Due to the increased complexity of the orbital character of the levels, a more precise notation is necessary. Indeed, this is also a formalization of some ideas that already have been introduced in recent publications.^{26–28}

We must add the potential that corresponds to the removal of half-electron from the occupied level (labeled α). In the usual and simple cases for the bulk, the Kohn-Sham state $\psi_{\alpha}(k_{\text{VBM}})$ is composed only of the valence level p orbital of the ion. However, in the case of the defect, we can have a set of atoms contributing to this level, in which case we must remove a smaller fraction of electron from each of them, proportionally to their contribution. Hence, for each atomic orbital ϕ of each atom X , we subtract a fraction $\xi_{X,\phi}$ of an electron given by

$$\xi_{X\phi} = \text{char}_{X\phi}[\psi_{\alpha}(\Gamma)] \times \frac{1}{2}, \quad (1)$$

where $\text{char}_{X\phi}[\psi(k)]$ corresponds to the proportion of the atomic orbital ϕ of atom X to the orbital character of the Kohn-Sham state ψ at point k . Similarly, we must add the potential that corresponds to the addition of half-electron to the unoccupied level (labeled β). The fraction $\zeta_{X\phi}$ to be added to the orbital ϕ of atom X is given by:

$$\zeta_{X\phi} = \text{char}_{X\phi}[\psi_{\beta}(\Gamma)] \times \frac{1}{2}. \quad (2)$$

The projection on atomic orbitals is usually a standard output of DFT codes, and is computed as the projection of the wave functions onto spherical harmonics within

spheres of an atomic species-dependent radius around each ion. Considering the fact that some small contributions of atoms far from the defect are going to be neglected, it is important to normalize the orbital characters of the considered atoms with respect to their sum, ensuring that

$$\sum_{X\phi} \xi_{X\phi} = \sum_{X\phi} \zeta_{X\phi} = \frac{1}{2}. \quad (3)$$

The self-energy potentials are considered spherically symmetric, so the dependence on r will be omitted on our notation. We compute the components $V_S^{X\phi}$ of the self-energy potential V_S as

$$V_{S,\alpha}^{X\phi} = V_X(f_0) - V_X(f_0 - \xi_{X\phi}) \quad (4)$$

$$V_{S,\beta}^{X\phi} = -[V_X(f_0) - V_X(f_0 - \zeta_{X\phi})], \quad (5)$$

where f_0 is the occupation of the orbital ϕ of atom X on the ground state, and $V_X(f)$ is the potential of atom X with occupation f . Adding the components, we find

$$V_S^{X\phi} = V_X(f_0 - \zeta_{X\phi}) - V_X(f_0 - \xi_{X\phi}). \quad (6)$$

Before adding the potentials to the Kohn-Sham potential, we must multiply them by a trimming function $\Theta_{X\phi}(r)$ to avoid the divergence that would arise from the sum of the $1/r$ coulombic tails of these potentials.^{6,7} Θ is a smooth step-like function, defined as

$$\Theta(r) = \begin{cases} \left[1 - \left(\frac{r}{CUT}\right)^8\right]^3 & \text{if } r \leq CUT \\ 0 & \text{if } r > CUT \end{cases} \quad (7)$$

which depends on a parameter called CUT . This parameter have to be determined variationally, by extremizing the band gap.^{6,7} Thus, the trimmed potential is

$$\widehat{V}_S^{X\phi} = \Theta_{X\phi} V_S^{X\phi}. \quad (8)$$

It is common to have situations in which the CUT depends only on the atom. In these cases, it is useful to define

$$\widehat{V}_S^X = \Theta_X \sum_{\phi} V_S^{X\phi}, \quad (9)$$

and then we would have a single correction to the potential per atomic specie, with a single value of CUT to be determined variationally.

The most noticeable difference between the usual DFT-1/2 and the procedure here introduced is that in the latter exactly half electron is transferred between the defect levels, being divided amongst the atoms which contribute to them. In solids, the total number of transferred electrons scales with the number of atoms in the cell, since the corrections are applied as if each atom contributed independently to the composition of the VBM and the CBM.

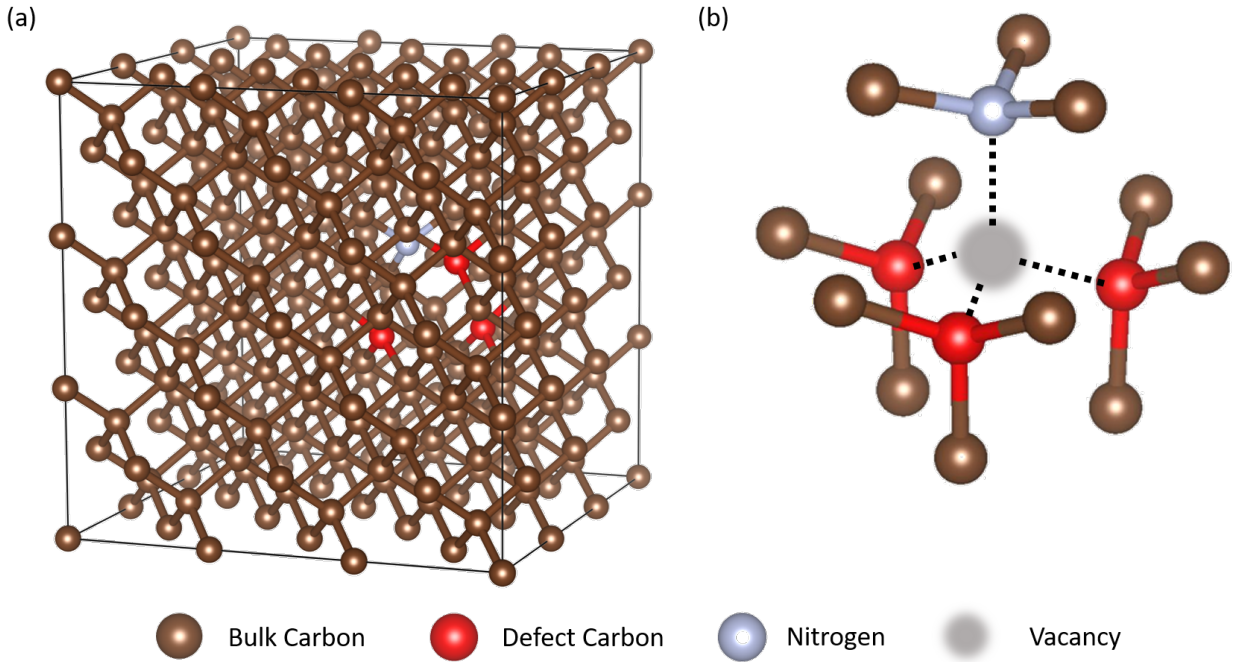


FIG. 4. (color online) (a) 215-atom supercell used to simulate the defect avoiding spurious interactions among images. (b) NV⁻ center and its surrounding atoms, representing the vacancy as a gray shadow. In both images, Brown, bluish-gray and red circles represent, respectively, the host carbon atoms, the nitrogen atom, and the three carbon atoms neighboring the vacancy. The images have been produced with help of the VESTA software.²⁹

IV. COMPUTATIONAL DETAILS

The calculations have been performed within the DFT combined with the Generalized Gradient Approximation of Perdew-Burke-Ernzerhof (GGA-PBE) exchange-correlation potential³⁰ using the Vienna Ab-initio Simulation Package (VASP).^{31,32} The electronic wave functions have been expanded using the projected augmented wave (PAW) method.^{33,34}

In order to build a good approximation for the supercell structure, first the structure of a single cubic unit cell has been relaxed. The next step is to replicate it side by side to build a 3x3x3 supercell, with a total of 216 atoms, and a new structural relaxation has been carried out. Then, the defect has been created by arbitrarily removing one of the atoms of the supercell and replacing one of the carbon atoms neighboring the resulting vacancy by a nitrogen (Fig. 4). The number of electrons has been increased by one, since we are interested in the negatively charged NV center. As the last step before applying the DFT-1/2 corrections, a spin-polarized structural relaxation has been performed for both the electronic ground state and first excited state by setting the corresponding energy levels occupations, to obtain and store the respective resulting atomic positions. It is noteworthy that, according to Fig. 1, the first excited state corresponds to promote the highest occupied spin-down state ($2a_{1\downarrow}$) to the lowest unoccupied spin-down

states ($e_{x\downarrow}$ and $e_{y\downarrow}$), with half electron in each one of the states, to symmetrize the occupation.

In the geometry optimization of the pure cells, *i.e.* cells that do not include the defect, the volume and shape of the cell and all the atoms have been allowed to relax until the magnitude of all forces is smaller than 10^{-3} eV/Å. In order to save computational effort and relying on the fact that only the nearest atoms should be affected by the defect, the volume and shape of the cell have been fixed for the relaxation of the supercells with the defect, and the same stopping criteria as before has been used.

Following the Monkhorst-Pack scheme,³⁵ the Brillouin zone (BZ) has been sampled by a 19x19x19 grid of k-points for the single cubic cell and by only the gamma point for the supercells. The plane wave basis set has been considered within a cutoff energy of 530 eV. The electronic convergence criterion has been that the total (free) energy and the band structure energy change between two steps are both smaller than 10^{-7} eV. In the simulation of the negatively charged defect, a positive uniform background charge has been added. The numeric errors of our calculations have been estimated to be smaller than 50 meV.

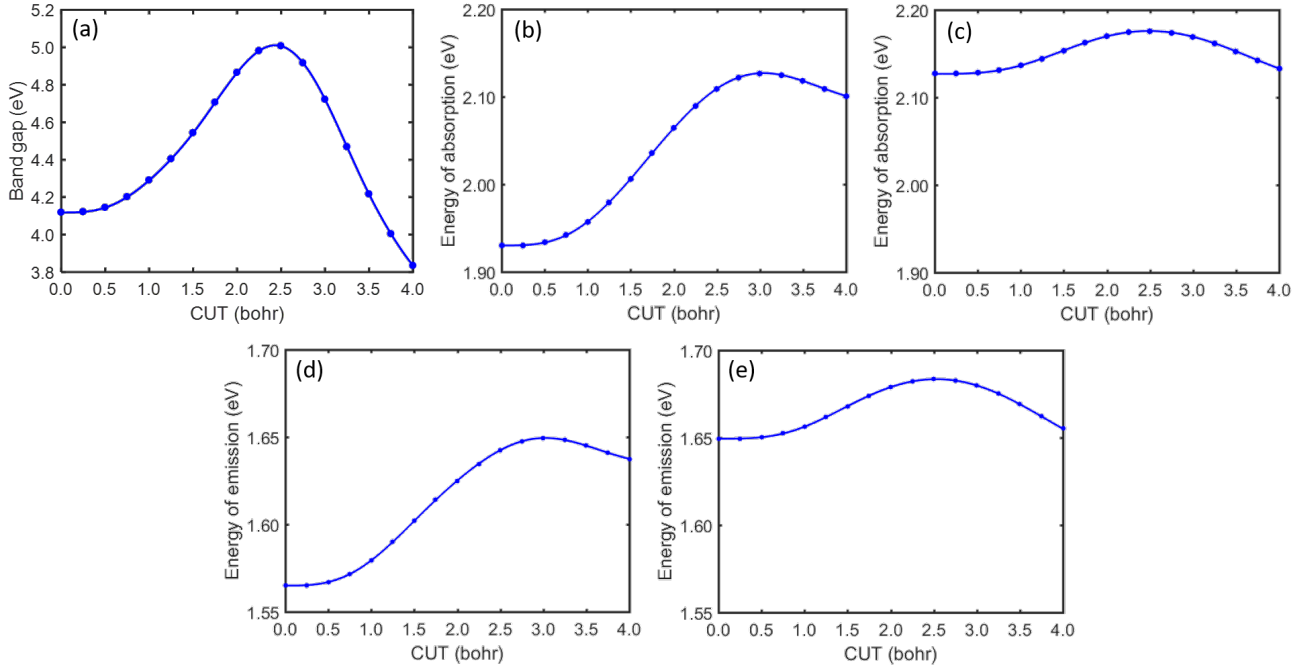


FIG. 5. (color online) CUT determination for the DFT-1/2 corrections. The corrections have been performed sequentially for each geometry, in the following order: C_{Bulk} , N, C_{Defect} . (a) Band gap of pure diamond as a function of the CUT for the 0.25 electron removal from the C_{Bulk} atoms' $2p$ orbital; (b) Transition energy on the ground state's geometry as a function of the CUT of the nitrogen atom, with C_{Bulk} corrected; (c) Transition energy on the ground state's geometry as a function of the CUT of the C_{Defect} atoms, with C_{Bulk} and N corrected; (d) Transition energy on the excited state's geometry as a function of the CUT of the nitrogen atom, with C_{Bulk} corrected; (e) Transition energy on the excited state's geometry as a function of the CUT of the C_{Defect} atoms, with C_{Bulk} and N corrected.

V. APPLYING THE LOCAL CORRECTION TO THE NV⁻ CENTER IN DIAMOND

The usual procedure to calculate the optical transition energies of defect levels is to take the difference in total energy between each electronic configuration. Because this concerns excitations, one needs to go beyond the Kohn-Sham scheme, by carrying out *e.g.* HSE calculations, to avoid the usual band gap problem.¹⁷ Hence, one must go beyond standard DFT, as in HSE calculations, in order to obtain a more accurate result for these energies. The inconvenient is the increase in the computational cost. Therefore, it would be of interest to apply the less demanding DFT-1/2 formalism. However, as implemented, this method does not compute a physically meaningful total energy, but the optical transition energies can be accurately obtained as the difference between their corresponding Kohn-Sham eigenvalues, as demonstrated in appendix A.

We must obtain the difference between the state $2a_{1\downarrow}$ and the double-degenerated state e_{\downarrow} in each geometry, according to Fig. 1. We may write

$$E_{Ab} = \varepsilon(e_{\downarrow}; q_{gnd}) - \varepsilon(2a_{1\downarrow}; q_{gnd}) \quad (10)$$

$$E_{Em} = \varepsilon(e_{\downarrow}; q_{exc}) - \varepsilon(2a_{1\downarrow}; q_{exc}), \quad (11)$$

where $\varepsilon(\psi; q)$ corresponds to the eigenvalue of the state

TABLE I. Orbital character of the defect levels and fractions of electron to be removed from and added to each potential (denoted by ξ and ζ , respectively).

$X\phi$	Ground State				Excited State			
	$2a_{1\downarrow}$	$\xi_{X\phi}$	$e_{x\downarrow}+e_{y\downarrow}$	$\zeta_{X\phi}$	$2a_{1\downarrow}$	$\xi_{X\phi}$	$e_{x\downarrow}+e_{y\downarrow}$	$\zeta_{X\phi}$
C_{2s}	0.6%	0.00	3.1%	0.02	0.6%	0.00	2.2%	0.01
C_{2p}	17.7%	0.09	30.2%	0.15	21.7%	0.11	31.1%	0.16
N_{2s}	4.6%	0.02	0.0%	0.00	4.9%	0.02	0.0%	0.00
N_{2p}	40.7%	0.20	0.3%	0.00	28.1%	0.14	0.3%	0.00

ψ as a function of the configuration coordinate q , which in the current case correspond to the most stable geometries in each one of the two electronic configurations, as indicated in Fig. 2. Note that it is only possible to unambiguously define these functions because the position of the eigenvalues are considered independent of the occupation of these levels, as explained in the appendix A. Otherwise, they would be functions of the occupation as well.

With the relaxed geometries for both the ground and excited states, we first separate the atoms in three types: the carbon atoms of the bulk (C_{Bulk}), which are responsible for the valence and conduction bands, the nitrogen atom, and the carbon atoms which are the carbon va-

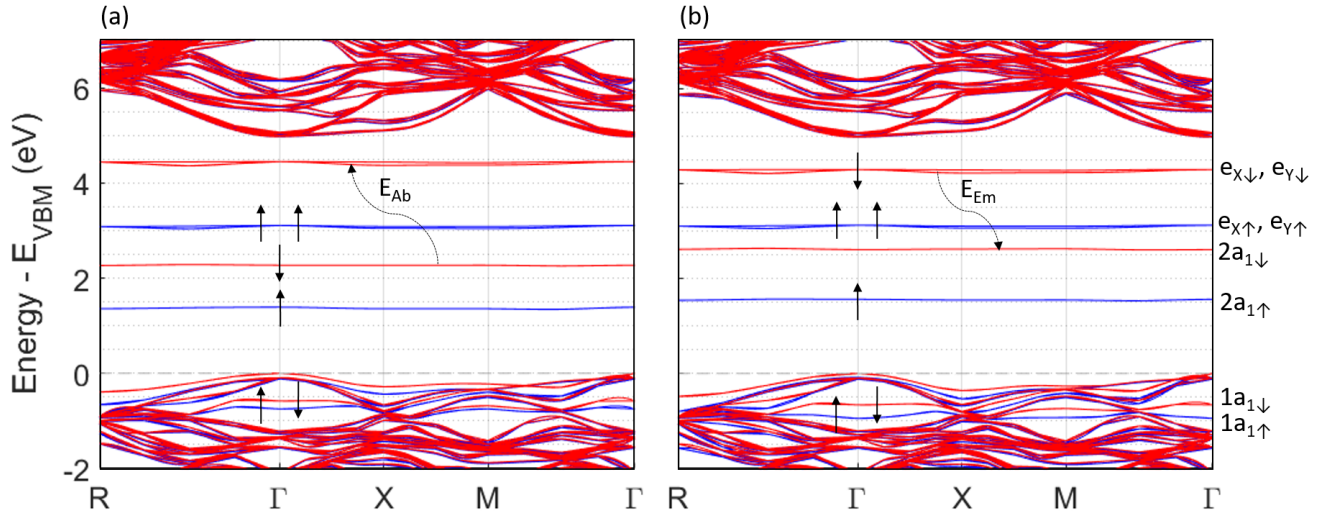


FIG. 6. (color online) Supercell band structures, around the gap region and along some special high symmetry directions in the cubic BZ, for the structural geometries of the NV⁻ center in the (a) ground state and (b) excited state. The blue and red lines represent, respectively, the spin-up and spin-down energy levels. The occupied states related to the defect are indicated by \uparrow and \downarrow arrows. Both results have been obtained with bulk and local corrections. The direct band gap is a consequence of the supercell band folding.

cancy next-neighbors (C_{Defect}), whose dangling bonds contribute to the localized defect levels. Since these types contribute differently to the band structure, they must be analyzed separately.

For the C_{Bulk} atoms, the same corrected potential as the one used in the diamond unit cell is applied: due to the perfectly covalent bonds between the carbon atoms, the band gap of diamond is corrected by subtracting one quarter of electron from the $2p$ orbital of the C_{Bulk} atoms, as indicated in Ref. 6. The CUT of 2.5 bohr is determined by maximizing the band gap, which gives a gap of 5.01 eV, as shown in Fig. 5(a).

To apply the local correction to the defect, the character of the levels involved in the first optical excitation, for both geometries, is determined by using the band character obtained by standard PBE calculation. Accordingly, the percentage of the character contribution is obtained by considering solely the nitrogen atom and the carbon atoms that are the vacancy next-neighbors (C_{Defect}). Table I presents the orbital character of the defect levels.

For each orbital, in each geometry, the potential of half electron, weighted by the character of the $2a_{1\downarrow}$ level, must be removed, while the potential of half electron, weighted by the character of the two states e_{\downarrow} , must be added. These results are also displayed in Table I. The CUT parameters for these corrections are determined by maximizing the difference between the levels e_{\downarrow} and $2a_{1\downarrow}$, and we obtain the same values for the excited and ground states, which are CUT=2.50 bohr for C_{Defect} and CUT=3.00 bohr for N. The curves obtained in this optimization procedure are displayed in Figs. 5 (b, c, d and

e).

The maximum values obtained on Figs. 5 (c and e) correspond, respectively, to the corrected absorption and emission energies. The values are displayed in Table II, together with other results and experimental data. With their respective corrected potentials, the electronic structure is calculated for each geometry, and the corrected band structures are displayed in Fig. 6. The energy differences between the defect levels correspond to the optical transition energies, as indicated by the curved arrows. The similarity of these results with the initial and simple picture of the position of the energy levels (Fig. 1) is remarkable. A discussion about Table II and about the band structures shown in Fig. 6 is given in Section VI.

Besides the vertical transition energies, the ZPL energy is also of experimental interest. We cannot simply use the difference between the Kohn-Sham eigenvalues of two different geometries to calculate it, since it would not take into account the energy difference due to the displacement of the ions. Nonetheless, we can indirectly calculate E_{ZPL} . This is possible because the values for the total energy of the two geometries in their electronic ground state are correctly calculated by the standard DFT. Hence, we can obtain the anti-Stokes shift as

$$E_{aS} = E(f_{gnd}, q_{exc}) - E(f_{gnd}, q_{gnd}), \quad (12)$$

where $E(f, q)$ is the energy as a function of the electronic configuration f and the geometry q , and use it together with the vertical transitions to determine the remaining desired energies as

$$E_{ZPL} = E_{Em} + E_{aS} \quad (13)$$

$$E_S = E_{Abs} - E_{ZPL}, \quad (14)$$

as one can readily see from Fig. 2.

Finally, the steps to be followed to apply the DFT-1/2 method for defect levels, introducing Local Corrections, can be summarized:

1. Perform the structural relaxation of the unit cell;
2. Determine the VBM and CBM orbital characters;
3. Build the supercell and perform a new structural relaxation;
4. Set and build the defect in the supercell, perform the structural relaxation with the electronic ground state occupancy and determine the orbital character of the selected defect levels;
5. Perform the structural relaxation with the electronic excited state occupancy and determine the orbital character of the selected defect levels;
6. Calculate the system total energy in the electronic ground state in the excited state geometry, and determine the anti-Stokes shift (E_{aS}) using Eq. 12;
7. Determine the CUT parameter for the bulk atoms by maximizing the band gap;
8. Determine the CUT parameter for the defect atoms by maximizing the energy difference between the selected defect levels, and determine the energies of the vertical transitions (E_{Ab} and E_{Em}); and
9. Determine the remaining energies (E_{ZPL} and E_S) using Eq. 13 and Eq. 14, respectively.
10. Optional: Calculate the corrected band structures.

VI. RESULTS AND DISCUSSION

The diamond band gap value of 5.01 eV obtained with GGA-1/2 approach shows a remarkable improvement over the value of 4.1 eV obtained with standard GGA, when compared to the experimental value of 5.47 eV.³⁶ Even though the result has a considerably better agreement with the experimental value, it is still slightly underestimated, not as good as the corrections to other materials.⁷ This is due to the fact that the VBM and CBM of diamond's band structure have almost the same orbital character and the usual procedure^{6,7} is not able to appropriately correct the conduction band.

The corrected band structures of Fig. 6 present all the expected general features for the NV⁻ center in diamond: the defect $1a_1$ energy levels are resonant inside the valence band; the relative positions of the spin up and spin down levels are correct; and the first possible valence band excitation is high energetic enough, avoiding an electron transition from the valence band to the defect $2a_{1\downarrow}$ energy levels when the pumping laser is shined.

Although the e_{\downarrow} energy levels appear to be closer to the conduction band than expected, due to the slightly underestimated band gap, the transition energies analysis is not impaired. On the other hand, since the gap underestimation is a diamond particular case, as explained

TABLE II. Vertical absorption (E_{Ab}), vertical emission (E_{Em}), zero-phonon line (E_{ZPL}), Stokes shift (E_S) and anti-Stokes shift (E_{aS}) energies calculated by different methods, compared to the experimental data¹² (all values in eV).

	E_{Ab}	E_{Em}	E_{aS}	E_{ZPL}	E_S
GGA (total energy)	1.90	1.55	0.16	1.71	0.19
GGA (eigenvalues)	1.86	1.55	0.16*	1.72 [†]	0.15 [‡]
GGA-1/2 (eigenvalues)	2.18	1.68	0.16*	1.85[†]	0.33[‡]
HSE06 ³⁷ (total energy)	2.21	1.74	0.22	1.96	0.26
Exp. ¹²	2.18	1.76	0.19	1.95	0.24

* Calculated using Eq. 12

[†] Calculated using Eq. 13

[‡] Calculated using Eq. 14

above, the method is expected to display still better performance when applied to other semiconductors, like the III-V ones, in which the application of the DFT-1/2 method presents very accurate results.⁷

The usual procedure to obtain the optical transition energies via DFT is to take the difference between the total energy values of the excited and ground states. The correction method proposed here allows these quantities to be extracted directly from the Kohn-Sham eigenvalues. To verify this claim, Table II presents results obtained with the usual total energy approach and with the eigenvalues approach, without the quasi-particle corrections. Even though these values are not supposed to correspond to the quasi-particle band gap, they should agree with each other, and in fact, they do within a precision of 0.04 eV.

The results obtained when using the DFT-1/2 approximate quasi-particle corrections are in close agreement with the reported HSE results and experimental data. It is observed that, in the GGA-1/2 results, the relative error of the Stokes and anti-Stokes shifts are greater than that of the other energies, as expected, since both shifts values result from the difference between two values very close to each other.

In our development, it has been argued that standard DFT approach may provide a good estimate of the anti-Stokes shift, and this is supported by the results from Ref. 37 that reports both GGA-PBE and HSE calculations of the anti-Stokes shift for a larger supercell (4ax4ax4a) than the one used here, and they indeed shown that GGA slightly outperformed HSE.

VII. CONCLUSION

The Kohn-Sham eigenvalues, with quasi-particle corrections, have been related to the experimental transition energies by introducing a new procedure, that allows

the application of the low computational effort method DFT-1/2 to correct the relative position of the deep defect energy levels. Since this method sharply reduces the computational cost when compared with other methods, it allows a systematic search for new defects in semiconductor hosts for several applications, including the search for new solid state qubits. In particular, the NV⁻ center in diamond has been considered as a benchmark of the method, and also as an example of its application. In this test case, an accuracy of 0.1 eV have been reached in comparison with experimental data.

ACKNOWLEDGMENTS

We thank the brazilian funding agencies FAPESP (grant n. 2012/50738-3), CAPES (PVE - grant n. 88887.116535/2016-00), and CNPq (grants n. 305405/2014-4, 308742/2016-8, and 154636/2016-9) for the financial support. We acknowledge the National Laboratory for Scientific Computing (LNCC/MCTI, Brazil) for providing HPC resources of the SDumont supercomputer. LVCA acknowledge partial support from CNPq (grant n. 312337/2013-2)

BL thanks professor Tomás Palacios for the introduction to the search for solid state qubits.

Appendix A: Obtaining differences in total energy through eigenvalues

Consider a situation in which we want to obtain the energy of an electronic transition between the localized

states ψ_α and ψ_β through the use of a supercell DFT calculation. Defining the total energy E in terms of partial occupations

$$E = T + U[n] + E_{xc}[n], \quad (\text{A1})$$

$$n(\vec{r}) = \sum_i f_i |\psi_i(\vec{r})|^2, \quad (\text{A2})$$

where n is the electron number density, ψ_i is the i -th Kohn-Sham orbital and f_i its occupancy, T is the kinetic energy, U is the classical Coulomb energy, and E_{xc} is the exchange-correlation functional.

Considering all but ψ_α and ψ_β levels' occupations are fixed, we have $E = E(f_\alpha, f_\beta)$. The Janak's theorem states that

$$\frac{\partial E}{\partial f_i} = \varepsilon_i, \quad (\text{A3})$$

where ε_i is the i -th Kohn-Sham eigenvalue. In a large supercell, the excitation of a localized electron is a small perturbation on the Kohn-Sham operators. Thus, the position of the eigenvalues remain unchanged and we can immediately integrate to obtain

$$E(1, f_\beta) - E(0, f_\beta) = \varepsilon_\alpha, \forall f_\beta \quad (\text{A4})$$

and

$$E(f_\alpha, 1) - E(f_\alpha, 0) = \varepsilon_\beta, \forall f_\alpha. \quad (\text{A5})$$

We can express the transition energy of interest as

$$\Delta E_{trans} = E(0, 1) - E(1, 0) = \varepsilon_\beta - \varepsilon_\alpha, \quad (\text{A6})$$

i.e. the transition energy can be computed as the difference between the Kohn-Sham eigenvalues.

* brunolucatto@gmail.com; gmsn@ita.br

¹ P. R. Struck and G. Burkard, in *Handbook of Spintronics* (2016) pp. 71–103.

² J. J. Morton and B. W. Lovett, *Annual Review of Condensed Matter Physics* **2**, 189 (2011), arXiv:1103.0418.

³ M. W. Doherty, N. B. Manson, P. Delaney, F. Jelezko, J. Wrachtrup, and L. C. L. Hollenberg, *Physics Reports* **528**, 1 (2013), arXiv:1302.3288.

⁴ W. F. Koehl, H. Seo, G. Galli, and D. D. Awschalom, *MRS Bulletin* **40**, 1146 (2015).

⁵ L. Gordon, J. R. Weber, J. B. Varley, A. Janotti, D. D. Awschalom, and C. G. Van de Walle, *MRS Bulletin* **38**, 802 (2013).

⁶ L. G. Ferreira, M. Marques, and L. K. Teles, *Physical Review B* **78**, 125116 (2008), arXiv:0808.0729.

⁷ L. G. Ferreira, M. Marques, and L. K. Teles, *AIP Advances* **1**, 0 (2011).

⁸ J. R. Weber, W. F. Koehl, J. B. Varley, A. Janotti, B. B. Buckley, C. G. Van de Walle, and D. D. Awschalom, *Proceedings of the National Academy of Sciences of the United States of America* **107**, 8513 (2010), arXiv:1003.1754.

⁹ A. Lenef and S. C. Rand, *Physical Review B* **53**, 13441 (1996).

¹⁰ V. Gomes, L. Assali, J. Leite, A. Fazzio, and M. Caldas, *Solid State Communications* **53**, 841 (1985).

¹¹ C. A. Coulson and M. J. Kearsley, *Proceedings of the Royal Society A: Mathematical, Physical and Engineering Sciences* **241**, 433 (1957).

¹² G. Davies and M. F. Hamer, *Proc. Roy. Soc. Lond. A* **348**, 285 (1976), arXiv:arXiv:1011.1669v3.

¹³ Y. Tu, Z. Tang, X. G. Zhao, Y. Chen, Z. Q. Zhu, J. H. Chu, and J. C. Fang, *Applied Physics Letters* **103** (2013), 10.1063/1.4818659.

¹⁴ X. Wang, M. Zhao, Z. Wang, X. He, Y. Xi, and S. Yan, *Applied Physics Letters* **100**, 1 (2012).

¹⁵ L. Sham and M. Schlüter, *Physical Review B* **32**, 3883 (1985).

¹⁶ J. P. Perdew and M. Levy, *Physical Review Letters* **51**, 1884 (1983).

¹⁷ P. Rinke, A. Janotti, M. Scheffler, and C. G. Van De Walle, *Physical Review Letters* **102**, 1 (2009), arXiv:0812.2492.

¹⁸ J. Heyd, G. E. Scuseria, and M. Ernzerhof, *Journal of*

- Chemical Physics **118**, 8207 (2003).
- ¹⁹ J. Heyd, G. E. Scuseria, and M. Ernzerhof, *The Journal of Chemical Physics* **124**, 219906 (2006).
- ²⁰ M. S. Hybertsen and S. G. Louie, *Physical Review Letters* **55**, 1418 (1985).
- ²¹ R. R. Pela, M. Marques, and L. K. Teles, *Journal of Physics: Condensed Matter* **27**, 505502 (2015).
- ²² F. Matusalem, M. Ribeiro, M. Marques, R. R. Pela, L. G. Ferreira, and L. K. Teles, *Physical Review B - Condensed Matter and Materials Physics* **88**, 1 (2013).
- ²³ F. Matusalem, R. R. Pela, M. Marques, and L. K. Teles, *Physical Review B - Condensed Matter and Materials Physics* **90**, 1 (2014).
- ²⁴ J. Janak, *Physical Review B* **18**, 7165 (1978).
- ²⁵ J. C. Slater and K. H. Johnson, *Physical Review B* **5**, 844 (1972).
- ²⁶ F. L. Freitas, M. Marques, and L. K. Teles, *AIP Advances* **6**, 085308 (2016).
- ²⁷ F. L. Freitas, J. Furthmüller, F. Bechstedt, M. Marques, and L. K. Teles, *Applied Physics Letters* **108** (2016), 10.1063/1.4942971.
- ²⁸ C. A. Ataide, R. R. Pela, M. Marques, L. K. Teles, J. Furthmüller, and F. Bechstedt, *Physical Review B - Condensed Matter and Materials Physics* **95**, 30 (2017).
- ²⁹ K. Momma and F. Izumi, *Journal of Applied Crystallography* **44**, 1272 (2011).
- ³⁰ J. P. Perdew, K. Burke, and M. Ernzerhof, *Physical Review Letters* **77**, 3865 (1996), arXiv:0927-0256(96)00008 [10.1016].
- ³¹ G. Kresse and J. Furthmüller, *Computational Materials Science* **6**, 15 (1996), arXiv:0927-0256(96)00008 [10.1016].
- ³² G. Kresse and J. Furthmüller, *Physical Review B* **54**, 11169 (1996), arXiv:0927-0256(96)00008 [10.1016].
- ³³ P. E. Blöchl, *Physical Review B* **50**, 17953 (1994), arXiv:arXiv:1408.4701v2.
- ³⁴ G. Kresse, *Physical Review B* **59**, 1758 (1999).
- ³⁵ H. J. Monkhorst and J. D. Pack, *Physical Review B* **13**, 5188 (1976), arXiv:arXiv:1011.1669v3.
- ³⁶ C. J. H. Wort and R. S. Balmer, *Materials Today* **11**, 22 (2008).
- ³⁷ A. Gali, E. Janzén, P. Deák, G. Kresse, and E. Kaxiras, *Physical Review Letters* **103**, 186404 (2009), arXiv:0903.4078.

FOLHA DE REGISTRO DO DOCUMENTO

1. CLASSIFICAÇÃO/TIPO DM	2. DATA 29 de janeiro de 2019	3. DOCUMENTO Nº DCTA/ITA/DM-135/2018	4. Nº DE PÁGINAS 111
5. TÍTULO E SUBTÍTULO: Ab initio study of 2D heterostructures and defects in 3D semiconductors for physical implementation of qubits			
6. AUTOR(ES): Bruno Lucatto			
7. INSTITUIÇÃO(ÕES)/ÓRGÃO(S) INTERNO(S)/DIVISÃO(ÕES): Instituto Tecnológico de Aeronáutica – ITA			
8. PALAVRAS-CHAVE SUGERIDAS PELO AUTOR: Solid state qubit; Deep center; van der Waals qubit.			
9. PALAVRAS-CHAVE RESULTANTES DE INDEXAÇÃO: Heteroestruturas de van der Waals; Estruturas bidimensionais; Semicondutores; Cálculos ab initio; Física.			
10. APRESENTAÇÃO: <input checked="" type="checkbox"/> Nacional <input type="checkbox"/> Internacional ITA, São José dos Campos, Curso de Mestrado. Programa de Pós-Graduação em Física. Área de Física Atômica e Molecular. Orientador: Prof. Dr. Marcelo Marques. Defesa em 10/12/2018. Publicado em 2018.			
11. RESUMO: <p>A major challenge in creating a quantum computer is to find a quantum system that could be used to implement the qubits. In this scenario, solid state systems, such as deep center defects in semiconductors or quantum dots, are prominent qubit candidates, and <i>ab initio</i> calculations are one of the most important tools to theoretically study their properties. However, these calculations are usually highly involved, due to the large supercells needed, and the computational cost can be even larger when one goes beyond the Kohn-Sham scheme to correct the band gap problem and achieve good accuracy in the prediction of excited state phenomena.</p> <p>In this work, we use first principle calculations in the search of materials and systems that would be suitable for the physical implementation of quantum bits and other quantum information devices. This is addressed on two fronts: First, we develop a method that sharply reduces the computational cost of simulating deep center defects with DFT including quasiparticle corrections, and then we benchmark it with the largely used quantum register based on the negatively-charged NV center in diamond, obtaining a great agreement with experimental data. Second, we demonstrate the possibility of using a gated van der Waals heterostructure to implement spatial quantum superpositions of electron states and, moreover, to implement a qubit. We study the case of the ZrSe₂/SnSe₂ heterostructure, simulating it under the influence of the gate field, providing theoretical quantitative results of its operation as a qubit, and proposing a possible methodology to manipulate and to measure the information in this qubit.</p>			
12. GRAU DE SIGILO: <div style="display: flex; justify-content: space-around; align-items: center;"> <input checked="" type="checkbox"/> OSTENSIVO <input type="checkbox"/> RESERVADO <input type="checkbox"/> SECRETO </div>			